Electronic and phononic states of quantum structures

vorgelegt von

M. Sc.

Steffen Westerkamp

von der Fakultät II - Mathematik und Naturwissenschaften

der Technischen Universität Berlin

zur Erlangung des akademischen Grades

Doktor der Naturwissenschaften

- Dr. rer. nat. -

genehmigte Dissertation

Promotionsausschuss:

Vorsitzender: Prof. Dr. Michael Lehmann
Gutachter: Prof. Dr. A. Hoffmann
Gutachter: Dr. Matthias auf der Maur

Tag der wissenschaftlichen Aussprache: 23. Mai 2019

Berlin 2019

Abstract

Colloidal core-shell semiconductor quantum dots present a fascinating field in both semiconductor research and applications, because they share many properties with more conventional quantum dots embedded in bulk semiconductor materials, such as quantum dots produced via a Stranski-Krastanov process. Yet they are are both much simpler to produce, being the product of chemical synthesis methods, and, for this reason, their production is also much simpler to scale, making them very promising as a low-cost industrial substitute to quantum dots produced using high tech MOCVD machinery.
This advantage brings with it some challenges with regards to the control of the chemical synthesis process, but at this time, it is possible to mass produce colloidal quantum dots with very precise sizes and material compositions.
There have been theoretical studies of the electronic structure of colloidal core-shell quantum dots, but some aspects that have been thoroughly studied in Stranski-Krastanov quantum dots have so far not been the focus of the theoretical description of colloidal quantum dots.
These are the influences the internal electric potentials, which arise in semiconductor heterostructures, can have on the electronic structure of the quantum dots.
In this work, we compute both the piezoelectric potentials, which arise due to the strain imposed on the lattice structure due to the lattice constant mismatch between core and shell material, as well as the pyroelectric potentials, which are present only in semiconductor heterostructures with wurtzite lattice structure.
These potentials are then employed in our calculations of the electronic structure of colloidal quantum dots, performed for quantum dots with zincblende and wurtzite lattice structure using 8-band $\mathbf{k}\cdot\mathbf{p}$ theory. We present results both for the single-particle picture and the multi-particle picture, derived using an iterative Hartree-Fock approach.
Our calculations show that the influence of the internal potentials differs strongly between the two considered lattice structures: while for zincblende the changes in electronic structure induced by the internal potentials are negligible, for quantum dots with wurtzite lattice structure we observe profound changes when internal potentials are incorporated: electron- and hole-wavefunctions are spatially separated, and their energy difference is strongly redshifted, an effect also observed for polar semiconductor heterostructures in bulk materials and usually named the quantum confined Stark effect.
Additionally, we present calculations performed for non-spherical quantum dots, modeled by us as ellipsoids. We find that deviations from sphericity lift degeneracies in the energy structure, and also shift the effective bandgap of the quantum dots.
Insight into the excitonic properties is shown via the multiparticle calculations, here we observe, for wurtzite quantum dots, that the excitonic ground state is not entirely spin-polarized, leading to a non-zero matrix-element, and therefore luminescence from the ground state. This is in contrast to previous work, which characterised this ground state as a dark state.
Our analysis of the vibrational properties of the quantum dots lead to the following insights: The vibrational eigenmodes, or phonons, of the system can be classified into distict groups, differentiated by their energies. The phonons in a group all show similar distribu-

tions of their atomic dynamics; while some groups closely resemble bulk phonons, others show a very localised dynamics that more resembles molecular vibrations.
When we determine the coupling of the phonons to different transitions in the excitonic system, we find that only a small percentage of phonons show significant coupling, and those who do are constrained to small parts of the energy scale, leading to the formation of peaks in the coupling spectra. Furthermore, most phonons that exhibit significant coupling are found to display a bulk-phonon-like dynamics distribution.

Zusammenfassung

Kolloidale core-shell Quantenpunkte sind ein faszinierendes Feld in der Halbleiter-Forschung und in ihrer Anwendung, da sie viele Eigenschaften von etablierteren Quantenpunkten teilen, etwa Quantenpunkten, welche im Stranski-Krastanov Wachstumsmodus hergestellt wurden.
Zugleich sind kolloidale Quantenpunkte jedoch mit sehr viel einfacheren Verfahren zu produzieren, da sie das Produkt chemischer Syntheseverfahren sind, welche auch deutlich leichter im Produktionsvolumen zu skalieren sind als die sehr aufwändige und teure Herstellung mit z.B. MOCVD-Verfahren.
Dieser Vorteil bringt auch Herausforderungen mit sich, da chemische Herstellungsprozesse nicht notwendigerweise dieselbe Präzision wie MOCVD-Verfahren aufweisen, es ist jedoch mittlerweile möglich, sehr präzise kolloidale Quantenpunkte, in Bezug auf ihre Größe und chemische Komposition in Masse zu produzieren.
Die bisherige theoretische Behandlung der elektronischen Eigenschaften dieser Quantenpunkte hat einige Aspekte, welche bei selbstorganisierten Quantenpunkten bereits seit langem im Detail untersucht wurden, nicht in vollem Umfang mit einbezogen. Dies sind insbesondere die internen elektrischen Potentiale, welche in Halbleiter-Heterostrukturen jeder Art auftreten, und die Auswirkungen dieser Potentiale auf die elektronische Struktur.
In dieser Arbeit präsentieren wir Berechnungen der elektronischen Struktur für kolloidale core-shell Quantenpunkte für zwei verschiedene Gitterstrukturen: Zinkblende und Wurtzit. Wir berechnen sowohl piezoelektrische Potentiale, welche durch die Verzerrung der Gitterstruktur innerhalb der Quantenpunkte entstehen, welche durch die unterschiedlichen Gitterkonstanten der zwei Materialien ausgelöst wird, als auch die pyroelektrischen Potentiale, welche für Wurtzit-Heterostrukturen auftreten.
Diese Potentiale werden dann in die Berechnung der elektronischen Struktur, welche mithilfe von 8 Band $\mathbf{k}\cdot\mathbf{p}$ Theorie durchgeführt wird, einbezogen. Wir präsentieren Ergebnisse sowohl im Einteilchen-Bild als auch für Exzitonen im Mehrteilchenbild. Die exzitonischen Zustände werden durch in iteratives Hartree-Fock Verfahren berechnet.
Unsere Ergebnisse zeigen, dass der Einfluss der internen Potentiale für die beiden betrachteten Gitterstrukturen sehr unterschiedlich ausfällt: während die Änderungen der elektronischen Struktur durch die Potentiale für Zinkblende-Quantenpunkte vernachlässigbar sind, gibt es einen starken Einfluss für Wurtzit-Quantenpunkte: hier beobachten wir zum einen eine räumliche Trennung von Elektronen- und Loch-Wellenfunktionen, als auch eine starke Rotverschiebung ihrer Energiedifferenz. Dieses Phänomen wird im Forschungsfeld selbstorganisierter Quantenpunkte und Quantenwells als quantum confined Stark effect bezeichnet.
Zusätzlich präsentieren wir Ergebnisse für nicht-sphärische Quantenpunkte, welche von uns als Ellipsoide modelliert werden: hier finden wir, dass Abweichungen von der Kugelform sowohl Entartungen in der Energiestruktur der Zustände aufbrechen, als auch die effektive Bandlücke verschieben können.
Aus den Berechnungen der exzitonischen Zustände lernen wir, dass der Grundzustand, welcher in vorherigen theoretischen Betrachtungen von kolloidalen Quantenpunkten stets

als dark state betrachtet wurde, nicht komplett spin-polarisiert ist, und daher ein nicht-verschwindendes Matrixelement hat, also Lumineszenz zeigt.
Unsere Analyse der Schwingungseigenschaften der Quantenpunkte liefert uns folgende Erkenntnisse: die Schwingungs-Eigenmoden, oder Phononen, des Systems können in klar voneinander abgegrenzte Gruppen eingeteilt werden, wobei die Gruppen anhand der Schwingungsenergien klassifiziert werden können. Die Phononen innerhalb einer Gruppe zeigen sehr ähnliche räumliche Verteilungen ihrer atomaren Dynamik; während die Phononen in einigen Gruppen eine Dynamik zeigen, die sehr der Dynamik von Phononen in Bulk-Halbleitern ähnelt, ist die Dynamik der Phononen in anderen Gruppen sehr stark räumlich lokalisiert, und ähnelt eher Molekül-Schwingungen.
Die Untersuchung der Kopplungsstärke der atomaren Schwingungen an verschiedene Übergänge des exzitonischen Systems brachte uns folgende Erkenntnis: nur ein kleiner Prozentsatz der Schwingungs-Eigenmoden zeigt eine signifikante Kopplung, und diese Schwingungsmoden liegen in wenigen, kleinen Teilen der Energie-Skala, was dazu führt, dass die Kopplungs-Spektren klare Peaks zeigen. Ausserdem zeigen die meisten Phononen, welche an das elektronische System koppeln eine atomare Dynamik, ähnlich der von Bulk-Halbleiter-Phononen.

Publications of the author

[1] Felix Nippert, Anna Nirschl, Tobias Schulz, Gordon Callsen, Ines Pietzonka, Steffen Westerkamp, Thomas Kure, Christian Nenstiel, Martin Strassburg, Martin Albrecht, and Axel Hoffmann, "Polarization-induced confinement of continuous hole-states in highly pumped, industrial-grade, green InGaN quantum wells", Journal of Applied Physics 119, 215707 (2016)

[2] G.M.O. Hönig, S. Westerkamp, A. Hoffmann, and G. Callsen, "Shielding Electrostatic Fields in Polar Semiconductor Nanostructures", Phys. Rev. Applied 7, 024004 (2017)

[3] Sarah Schlichting, Gerald Hönig, J. Müßener, P. Hille, T. Grieb, S. Westerkamp, J. Teubert, J. Schörmann, Markus Wagner, Andreas Rosenauer, M. Eickhoff, Axel Hoffmann, and G. Callsen, "Suppression of the quantum-confined Stark effect in polar nitride heterostructures", Nature Communications Physics (accepted), 2018

[4] G. Hönig, S. Westerkamp, and G. Callsen, "SEMICONDUCTOR DEVICE HAVING AN INTERNAL-FIELD-GUARDED ACTIVE REGION", European patent no. 17160160.2, 2018, US patent no. US 2018 / 0261719 A1, 2018

Contents

1 Introduction

Quantum dots have been a fascinating field of research for many years, because they exhibit similar characteristics to single atoms, but are much easier to control and produce. Self-organized quantum dots grown on bulk materials offer a manifold of possibilities for applications, from efficient light-sources [1], to sources of single photons [2] or entangled photon pairs [3]. The drawback for applications is the expensive and difficult to control fabrication process, using, for example, an MOCVD process [4].

Colloidal quantum dots share many of the promising characteristics of the quantum dots embedded in a bulk semiconductor matrix. Yet they are most often produced in liquid solution.

As a result, they are much simpler to produce, as they are the product of a chemical synthesis process [5]. Additionally, their fabrication process is much easier to scale, because it does not rely on expensive high-tech machinery, such as MOCVD production lines.

Their current and potential future applications are manifold: colloidal quantum dots are used in such diverse areas as background-lighting in LED television screens [6] and biological sensors in medicinal research [7, 8, 9].

Most theoretical studies of the electronic structure of colloidal quantum dots have utilized the very simple geometries of these systems to develop analytical solutions for the energies and wavefunctions [10, 11, 12] of their electron- and hole-states. Subsequently, these solutions have been utilized to develop a multi-particle picture [13, 14, 15], and a description of the expected radiative behaviour of these quantum dots.

These analytical results for the electronic structure has then been combined with calculations of the vibrational properties [16, 17] of the atomic structure of colloidal quantum dots, to assess electron-phonon coupling [18, 19].

In this work, we expand these theoretical descriptions, using a numerical approach to compute the electronic structure, and incorporating strain effects and internal electric potentials in these computations. The numerical calculation approach used in this work was developed by my predecessors in my workgroup, and originally applied to self-organized quantum dots grown in the Stranski-Krastanov growth mode. It was modified slightly to enable us to apply it to this new class of quantum dots, making it possible for us to assess the impact of these effects, that have not been the focus for studies of colloidal quantum dots before.

In this work, we will begin, in chapter 2, by describing in detail the computational methods and underlying theories employed for calculations of the electronic structure, the vibrational properties and the coupling between these two systems. A particular emphasis is placed on the 8-band $\mathbf{k}\cdot\mathbf{p}$ theory, outlining the differences between the two lattice structures.

Subsequently, in chapter 3, we will provide an overview over the preceding theoretical descriptions for colloidal quantum dots.

In chapter 4 we will present the results of the calculations of the internal strain distributions inside the quantum dots, and the internal electric potentials, again emphasising the differences that result from the different lattice structures.

We then proceed, in chapter 5, to the results of the single-particle results of the 8-band

k·p calculations, analysing in detail the energy-spectrum and the symmetries of the single-particle wavefunctions, as well as the impacts of our calculated internal potentials on these properties. Another aspect presented here is the impact of deviations from sphericity of the quantum dot shapes on the electronic structure.

Chapter 6 contains the results of the multi-particle 8-band **k·p** calculations. The energy structure and wavefunctions of the excitons are detailed, and, additionally, we perform an analysis of the spin-projections of the electron- and hole-components of the excitons as well as the excitonic lifetimes.

Thereafter, in chapter 7, we present the results for the coupling of the vibrational eigenmodes of the quantum dots to various transitions in the excitonic structure. The effects of lattice structure and quantum dot geometry on these couplings are examined, and general properties of exciton-phonon coupling in colloidal quantum dots are presented.

We then move on to present further analysis of the vibrational eigenmodes of the quantum dots, in chapter 8. We develop a method to classify different vibrational eigenmodes based on the spatial distribution of their atomic motion, and present the results of our application of this method. We also investigate the properties of the phonons that display significant coupling to the excitonic structure.

Finally, in chapter 9, we summarise the major results presented in this work, assess the limitations of our methods and results, and present an outline of promising future research to further our understanding of this particular field of research, and put the results of this work into perspective.

2 Methods

2.1 Overview

In this chapter, the conceptual and computational methods used in this work will be introduced.
A solid consisting of electrons and atomic nuclei can be generally described by the following Schrödinger equation:

$$H\ \Psi(\mathbf{r},\mathbf{R}) = E\ \Psi(\mathbf{r},\mathbf{R}) \quad , \tag{2.1}$$

where the wavefunction $\Psi(\mathbf{r},\mathbf{R})$ is dependent on the positions of both the electrons $\mathbf{r}$ and nuclei $\mathbf{R}$. The Hamiltonian has the general form

$$H = T_C(\mathbf{P}) + T_e(\mathbf{p}) + V_{C-C}(\mathbf{R}) + V_{e-e}(\mathbf{r}) + V_{e-C}(\mathbf{r},\mathbf{R}) \quad , \tag{2.2}$$

and consists of the kinetic energy operators for electrons, T_E, and nuclei, T_C, as well as the interactions between electrons, V_{e-e}, between nuclei, V_{C-C} and also interactions between electrons and nuclei, V_{e-C}.
Since the masses of electrons are much smaller than the nuclei masses, the timescales of the electron dynamics are much smaller compared to the atomic nuclei. Therefore, we can separate these dynamics, in what is called the Born-Oppenheimer-approximation, or adiabatic approximation.
Assuming that on the timescale of electron dynamics, the nuclei can be considered to be at their rest positions $\mathbf{R}^{(0)}$, the electron may only depend on the electron coordinates $\mathbf{r}$. If we furthermore neglect electron-electron interaction, the Schrödinger equation for the electrons becomes:

$$\left(\frac{\mathbf{p}^2}{2m} + V(\mathbf{r},\mathbf{R}^{(0)})\right)\Psi(\mathbf{r}) = E\Psi(\mathbf{r}) \quad , \tag{2.3}$$

with the electronic momentum operator $\mathbf{p}$, the electron mass m and the potential $V(\mathbf{r})$, which is generated by the static atomic nuclei.
On the other hand, when modeling the dynamics of the atomic nuclei, we can assume that they are affected by the electrons only by an effective potential $V_{\text{eff}}(\mathbf{R})$, which now only depends on the coordinates of the atomic nuclei. We then obtain the Schrödinger equation for the atomic nuclei as

$$\left(\sum_{i=1}^{N}\frac{\mathbf{P}_i^2}{2M_i} + V_{\text{eff}}(\mathbf{R}_1,...,\mathbf{R}_N)\right)\Psi(\mathbf{R}_1,...,\mathbf{R}_N) = E\ \Psi(\mathbf{R}_1,...,\mathbf{R}_N) \quad , \tag{2.4}$$

where $\mathbf{P}_i$ is the momentum operator and M_i are the atomic masses.
We have thus separated the electron dynamics from the dynamics of the atomic cores.

Now, we will solve these two parts independently, by employing different methods, which will be described in detail below:

1. The calculations for the electronic part are performed using single-particle and multi-particle $\mathbf{k}\cdot\mathbf{p}$-theory. These take into account strain effects as well as internal polarisation fields, and are performed employing a continuous media approach. Numerical implementation is performed on a finite differences voxel-grid. These methods are outlined in chapters 2.2, 2.3, 2.4 and 2.5.

2. The dynamics of the atomic nuclei are performed using an atomistic approach, and are outlined in chapter 2.6.

Finally, to compute the coupling between the electronic and the vibrational systems inside the quantum dot, we utilise the results of both these parts, which is outlined in chapter 2.7.
All computations will be performed for zincblende and wurtzite lattice structures.

2.2 Strain Calculation

Strain in solids is commonly described via a displacement vector field $\mathbf{u}(\mathbf{r})$, which represents the displacement of atoms from their equilibrium positions. One can then introduce a strain-tensor $\epsilon(\mathbf{r})$ which is related to the displacement field via

$$\epsilon_{ij} = \frac{\partial u_i}{\partial x_j} \quad . \tag{2.5}$$

Using Voigt-notation, we can express the relation, in linear approximation, of the strain tensor to the stress tensor σ by

$$\begin{pmatrix} \sigma_{xx} \\ \sigma_{yy} \\ \sigma_{zz} \\ \sigma_{yz} \\ \sigma_{xz} \\ \sigma_{xy} \end{pmatrix} = \mathbf{C} \begin{pmatrix} \epsilon_{xx} \\ \epsilon_{yy} \\ \epsilon_{zz} \\ 2\epsilon_{yz} \\ 2\epsilon_{xz} \\ 2\epsilon_{xy} \end{pmatrix} \quad , \tag{2.6}$$

where $\mathbf{C}$ is the (material-dependent) stiffness tensor. This expression is a generalisation of Hooke's Law in three dimensions.
Strain can be introduced into solids by external stress, lattice-mismatch, or thermal effects. In the case of the colloidal quantum dots that are the subject of this work, we consider only the strain caused by lattice mismatches. The total strain energy of the system, U, can then be expressed by [20]:

$$U = \int_V \frac{1}{2} \sum_{i,j,k,l} C_{ijkl} \epsilon_{ij} \epsilon_{kl} \mathrm{d}V \quad . \tag{2.7}$$

For zincblende lattice structure, the stiffness tensor is given by [21]

$$\mathbf{C} = \begin{pmatrix} C_{11} & C_{12} & C_{12} & 0 & 0 & 0 \\ C_{12} & C_{11} & C_{12} & 0 & 0 & 0 \\ C_{12} & C_{12} & C_{11} & 0 & 0 & 0 \\ 0 & 0 & 0 & C_{44} & 0 & 0 \\ 0 & 0 & 0 & 0 & C_{44} & 0 \\ 0 & 0 & 0 & 0 & 0 & C_{44} \end{pmatrix} \quad . \tag{2.8}$$

In the case of a wurtzite lattice structure, the stiffness tensor is [22]:

$$\mathbf{C} = \begin{pmatrix} C_{11} & C_{12} & C_{13} & 0 & 0 & 0 \\ C_{12} & C_{11} & C_{13} & 0 & 0 & 0 \\ C_{13} & C_{13} & C_{33} & 0 & 0 & 0 \\ 0 & 0 & 0 & C_{44} & 0 & 0 \\ 0 & 0 & 0 & 0 & C_{44} & 0 \\ 0 & 0 & 0 & 0 & 0 & \frac{C_{11}-C_{12}}{2} \end{pmatrix} . \tag{2.9}$$

Using equation 2.7, we can then iteratively calculate the strain distribution on a spacial voxel grid by minimising the total lattice strain energy U [23].
Strain effects on the electronic structure can be approximated by evaluating different types of strain. The hydrostatic strain

$$\epsilon_H = \epsilon_{xx} + \epsilon_{yy} + \epsilon_{zz} \tag{2.10}$$

shifts the conduction and valence-band energies, while the biaxial strain

$$\epsilon_B = \epsilon_{xx} + \epsilon_{yy} - 2\epsilon_{zz} \tag{2.11}$$

splits the band-edges of the highest energy valence-bands.

2.3 Internal Potentials

2.3.1 Piezoelectric Polarisation

In lattice structures without inversion symmetry, such as zincblende and wurtzite, the application of stress gives rise to an electric polarisation called piezoelectricity. This polarisation is given by:

$$\mathbf{P} = \mathbf{e} \cdot \epsilon \quad , \tag{2.12}$$

using the electromechanical tensor $\mathbf{e}$. In zincblende lattices, this tensor is given by:

$$\mathbf{e} = \begin{pmatrix} 0 & 0 & 0 & e_{14} & 0 & 0 \\ 0 & 0 & 0 & 0 & e_{14} & 0 \\ 0 & 0 & 0 & 0 & 0 & e_{14} \end{pmatrix} \quad , \tag{2.13}$$

whereas for wurtzite lattice structure it is of the following form:

$$\mathbf{e} = \begin{pmatrix} 0 & 0 & 0 & 0 & e_{15} & 0 \\ 0 & 0 & 0 & e_{15} & 0 & 0 \\ e_{31} & e_{31} & e_{33} & 0 & 0 & 0 \end{pmatrix} \quad . \tag{2.14}$$

The polarisation vectors are then given by

$$\mathbf{P}_{PZ}^{ZB} = 2e_{14} \begin{pmatrix} \epsilon_{yz} \\ \epsilon_{xz} \\ \epsilon_{xy} \end{pmatrix} \tag{2.15}$$

for zincblende and

$$\mathbf{P}_{PZ}^{WZ} = 2e_{15} \begin{pmatrix} \epsilon_{xz} \\ \epsilon_{yz} \\ 0 \end{pmatrix} + e_{31} \begin{pmatrix} 0 \\ 0 \\ \epsilon_{xx} + \epsilon_{yy} \end{pmatrix} + e_{33} \begin{pmatrix} 0 \\ 0 \\ \epsilon_{zz} \end{pmatrix} \tag{2.16}$$

for wurtzite structure.

2.3.2 Pyroelectric Polarisation

The wurtzite crystal structure additionally exhibits spontaneous (pyroelectric) polarisation due to not being centro-symmetric. This additional polarisation is modeled by a single material-parameter and is given by

$$\mathbf{P}_{SP}^{WZ} = \begin{pmatrix} 0 \\ 0 \\ P_{SP} \end{pmatrix} \quad , \tag{2.17}$$

for a system where the z-direction coincides with the wurtzite [0001]-direction.
The total polarisation for wurtzite is then given by the sum of piezo- and pyroelectric polarisations:

$$\mathbf{P}^{WZ} = \mathbf{P}_{PZ}^{WZ} + \mathbf{P}_{SP}^{WZ} \tag{2.18}$$

2.3.3 Potential calculation

The electric potentials $\Phi(\mathbf{r})$ corresponding to these polarisations are then determined by first calculating the polarisation charge densities ρ:

$$\rho(\mathbf{r}) = -\nabla \mathbf{P}(\mathbf{r}) \tag{2.19}$$

and subsequently solving the poisson-equation

$$\varepsilon_0 \nabla \cdot [\varepsilon_r(\mathbf{r}) \nabla \Phi(\mathbf{r})] = \rho(\mathbf{r}) \quad , \tag{2.20}$$

while accounting for the position-dependent relative permittivity $\varepsilon_r(\mathbf{r})$.

2.4 Localised electronic states: k·p-Theory

In a periodic potential, for example in a bulk semiconductor, electron- and hole wavefunctions are given as Bloch-waves, consisting of a plane-wave and a Bloch-function, which carries the same periodicity as the potential:

$$\Psi_{n,\mathbf{k}}(\mathbf{r}) = \exp(i\mathbf{k}\cdot\mathbf{r})u_{n,\mathbf{k}}(\mathbf{r}) \quad . \tag{2.21}$$

where n is the band-index and $\mathbf{k}$ is a wave-vector from the first Brillouin-zone. If we insert this Ansatz into equation 2.3, we arrive at a Schrödinger-equation for the Bloch-functions:

$$\left(\underbrace{\frac{\mathbf{p}^2}{2m} + V(\mathbf{r})}_{H_0} + \underbrace{\frac{\hbar^2\mathbf{k}^2}{2m} + \frac{\hbar\mathbf{k}\cdot\mathbf{p}}{m}}_{H_{\mathbf{k}\cdot\mathbf{p}}} \right) u_{n,\mathbf{k}}(\mathbf{r}) = E_{n,\mathbf{k}}u_{n,\mathbf{k}}(\mathbf{r}) \quad , \tag{2.22}$$

which has a term $H_{\mathbf{k}\cdot\mathbf{p}}$ that gives the theory its name.

2.4.1 Envelope-function Approximation

If we now consider semiconductor hetero-structures, we can no longer use the translational symmetry of the lattice, and therefore choose a different Ansatz for the wavefunctions, replacing the plane-waves with more general so called envelope-functions [24]:

$$\Psi_n(\mathbf{r}) = F_n(\mathbf{r})\ u_{n,\mathbf{k}=\mathbf{0}}(\mathbf{r}) \quad . \tag{2.23}$$

We are also now restricted to the Γ-Point in reciprocal space, and therefore replace all occurences of wave-vector entries k_i in the Hamiltonian by the corresponding real-space derivatives $i\partial_i$ which then yields a partial differential matrix equation for the envelope functions. These envelope functions are the wavefunctions we obtain in this work.

2.4.2 Hamiltonian

Since we are interested in the electronic structure around the Γ-point, only four electronic bands are taken into account: the lowest energy conduction band, as well as the three highest energy valence bands. When accounting for spin, this yields a total of eight electronic bands included in the Hamiltonian. The influence of the other bands is accounted for by Löwdin perturbation theory [25].
Following the Kane model [26], the Hamiltonian is expanded into the following basis of Bloch-functions:

$$\{|s\uparrow\rangle, |x\uparrow\rangle, |y\uparrow\rangle, |z\uparrow\rangle, |s\downarrow\rangle, |x\downarrow\rangle, |y\downarrow\rangle, |z\downarrow\rangle\} \quad ,$$

and takes the block matrix form

$$H = \begin{pmatrix} G(\mathbf{k}) & \Gamma \\ -\bar{\Gamma} & \bar{G}(\mathbf{k}) \end{pmatrix} \tag{2.24}$$

where $G(\mathbf{k})$ and Γ are 4x4-matrices. The matrix G is the sum of four different matrices:

$$G = G_1 + G_2 + G_{SO} + G_{st} \quad , \tag{2.25}$$

where G_1 accounts for the potential energy, G_2 for the kinetic energy, G_{SO} for the spin-orbit splitting and G_{st} for the strain dependent part [27, 28, 29, 30]. The matrix Γ accounts for the spin-orbit splitting between basis vectors of different spin.
The matrices G_1, G_2 and G_{st} differ between zincblende and wurtzite lattice structures. For zincblende, they are given by:

$$G_1 = \begin{pmatrix} E_C & iPk_x & iPk_y & iPk_z \\ -iPk_x & E'_V & 0 & 0 \\ -iPk_y & 0 & E'_V & 0 \\ -iPk_z & 0 & 0 & E'_V \end{pmatrix} \tag{2.26}$$

$$G_2 = \begin{pmatrix} A'\mathbf{k}^2 & Bk_yk_z & Bk_xk_z & Bk_xk_y \\ Bk_yk_z & L'k_x^2 + M(k_y^2 + k_z^2) & N'k_xk_y & N'k_xk_z \\ Bk_xk_z & N'k_xk_y & L'k_y^2 + M(k_x^2 + k_z^2) & N'k_yk_z \\ Bk_xk_y & N'k_xk_z & N'k_yk_z & L'k_z^2 + M(k_x^2 + k_y^2) \end{pmatrix} \tag{2.27}$$

$$G_{st} = \begin{pmatrix} a_c(\epsilon_{xx} & b'\epsilon_{yz} & b'\epsilon_{zx} & b'\epsilon_{xy} \\ +\epsilon_{yy} + \epsilon_{zz}) & -iP\epsilon_{xj}k^j & -iP\epsilon_{yj}k^j & -iP\epsilon_{zj}k^j \\ b'\epsilon_{yz} & l\epsilon_{xx} & n\epsilon_{xy} & n\epsilon_{xz} \\ +iP\epsilon_{xj}k^j & +m(\epsilon_{yy} + \epsilon_{zz}) & & \\ b'\epsilon_{zx} & n\epsilon_{xy} & l\epsilon_{yy} & n\epsilon_{yz} \\ +iP\epsilon_{yj}k^j & & +m(\epsilon_{xx} + \epsilon_{zz}) & \\ b'\epsilon_{xy} & n\epsilon_{xz} & n\epsilon_{yz} & l\epsilon_{zz} \\ +iP\epsilon_{zj}k^j & & & +m(\epsilon_{xx} + \epsilon_{yy}) \end{pmatrix} \tag{2.28}$$

where in equation 2.28, the Einstein summation index runs over $j = x, y, z$. The ϵ_{ij} are the components of the strain tensor from chapter 2.2.
The conduction band edge E_C and the valence band edge E'_V as well as the Kane-parameters A', L', M, N' and P and the strain coefficients l, m and n are given by [27, 26]:

$$
\begin{aligned}
E_C &= E_V + V_{ext} + E_G \\
E'_V &= E_V + V_{ext} + \frac{\Delta_{SO}}{3} \\
A' &= \frac{\hbar^2}{2m_0}\left(\frac{1}{m_e} - \frac{E_p}{E_0}\frac{E_0 + 2\Delta_0/3}{E_0 + \Delta_0}\right) \\
P &= \sqrt{\frac{\hbar^2}{2m_0}E_p} \\
L' &= \frac{P^2}{E_0} - \frac{\hbar^2}{2m_0}(1 + \gamma_1 + 4\gamma_2) \\
M &= -\frac{\hbar^2}{2m_0}(1 + \gamma_1 - 2\gamma_2) \\
N' &= \frac{P^2}{E_0} - \frac{3\hbar^2}{m_0}\gamma_3 \\
l &= 2b_v + a_c - a_g \\
m &= a_c - a_g - b_v \\
n &= \sqrt{3}d_v
\end{aligned}
$$

using the following parameters:

- the band gap E_G,
- the split-off energy Δ_{SO},
- the optical matrix parameter E_p,
- the valence band edge E_V,
- the relative electron mass at the Γ-point m_e,
- the Luttinger-parameters γ_1, γ_2 and γ_3,
- the Kane-parameter B,
- the hydrostatic conduction band deformation potential a_c,
- the hydrostatic band gap deformation potential a_g,
- the [100]-direction uniaxial valence band deformation potential b_v,
- the [111]-direction uniaxial valence band deformation potential d_v,
- the conduction band shear strain coupling parameter b',
- the external potential V_{ext}, as calculated in equation 2.20.

For wurtzite crystal structure, the matrices take the following form [30, 31, 32]:

$$G_1 = \begin{pmatrix} E_C + \Delta_{CR} & iP_2k_x & iP_2k_y & iP_1k_z \\ -iP_2k_x & E'_V + \Delta_{CR} & 0 & 0 \\ -iP_2k_y & 0 & E'_V + \Delta_{CR} & 0 \\ -iP_2k_z & 0 & 0 & E'_V \end{pmatrix} \tag{2.29}$$

$$G_2 = \begin{pmatrix} A'_2(k_x^2 + k_y^2) \\ +A'_1k_z^2 & B_2k_yk_z & B_2k_xk_z & B_1k_xk_y \\ B_2k_yk_z & L'_1k_x^2 + M_1k_y^2 \\ & +M_2k_z^2 & N'_1k_xk_y & N'_2k_xk_y - N'_3k_x \\ B_2k_xk_z & N'_1k_xk_y & M_1k_x^2 + L'_1k_y^2 \\ & & +M_2k_z^2 & N'_2k_xk_z - N'_3k_y \\ B_1k_xk_y & N'_2k_xk_y + N'_3k_x & N'_2k_xk_z + N'_3k_y & M_3(k_x^2 + k_y^2) \\ & & & +L'_2k_z^2 \end{pmatrix} \tag{2.30}$$

$$G_{st} = \begin{pmatrix} a_2(\epsilon_{xx} + \epsilon_{yy}) \\ +a_1\epsilon_{zz} & 0 & 0 & 0 \\ 0 & l_1\epsilon_{xx} + m_1\epsilon_{yy} \\ & +m_2\epsilon_{zz} & n_1\epsilon_{xy} & n_2\epsilon_{xz} \\ 0 & n_1\epsilon_{xy} & m_1\epsilon_{xx} + l_1\epsilon_{yy} \\ & & +m_2\epsilon_{zz} & n_2\epsilon_{yz} \\ 0 & n_2\epsilon_{xz} & n_2\epsilon_{yz} & m_3(\epsilon_{xx} + \epsilon_{yy}) \\ & & & +l_2\epsilon_{zz} \end{pmatrix} \tag{2.31}$$

where the ϵ_{ij} are the components of the strain tensor (from chapter 2.2) and the conduction and valence band edges E_C and E'_V, the dipole matrix parameters $P_{1/2}$, the parameters from the matrix G_2 as well as the strain parameters l_i, m_i and n_i are calculated by:

$$
\begin{aligned}
E_C &= E_V + E_G + V_{ext} \\
E'_V &= E_V + V_{ext} + \frac{\Delta_{SO}}{3} \\
P_{1/2} &= \sqrt{\frac{\hbar^2}{2m_0} E_{p1/2}} \\
A'_1 &= \frac{\hbar^2}{2}\left(\frac{1}{m_e^{\parallel}} - \frac{1}{m_0}\right) - \frac{P_1^2}{E_G}, \\
A'_2 &= \frac{\hbar^2}{2}\left(\frac{1}{m_e^{\perp}} - \frac{1}{m_0}\right) - \frac{P_2^2}{E_G}, \\
L'_1 &= \frac{\hbar^2}{2m_0}(A_2 + A_4 + A_5 - 1) + \frac{P_1^2}{E_G}, \\
L'_2 &= \frac{\hbar^2}{2m_0}(A_1 - 1) + \frac{P_2^2}{E_G}, \\
M_1 &= \frac{\hbar^2}{2m_0}(A_2 + A_4 - A_5 - 1), \\
M_2 &= \frac{\hbar^2}{2m_0}(A_1 + A_3 - 1), \\
M_3 &= \frac{\hbar^2}{2m_0}(A_2 - 1), \\
N'_1 &= \frac{\hbar^2}{2m_0} 2A_5 + \frac{P_1^2}{E_G}, \\
N'_2 &= \frac{\hbar^2}{2m_0}\sqrt{2}A_6 + \frac{P_1 P_2}{E_G}, \\
N'_3 &= i\sqrt{2}A_7, \\
l_1 &= D_2 + D_4 + D_5, \\
l_2 &= D_1, \\
m_1 &= D_2 + D_4 - D_5, \\
m_2 &= D_1 + D_3, \\
m_3 &= D_2, \\
n_1 &= 2D_5, \\
n_2 &= \sqrt{2}D_6
\end{aligned}
\tag{2.32}
$$

so that the Hamiltonian is parametrised by:

- the band gap E_G,
- the split-off energy Δ_{SO},
- the crystal field splitting energy Δ_{CR},
- the optical matrix parameters $E_{p,1}$ and $E_{p,2}$,
- the valence band edge E_V,

- the relative electron masses at the Γ-point $m_e^{\parallel}$, $m_e^{\perp}$ and the free electron mass m_0,
- the Luttinger-like parameters $A_1, A_2, A_3, A_4, A_5, A_6$ and A_7,
- the conduction band deformation potentials a_1 and a_2,
- the valence-band deformation potentials D_1, D_2, D_3, D_4, D_5 and D_6
- the external potential V_{ext}, as calculated in chapter 2.3

The parameters $B_{1/2}$ are due to the lack of inversion symmetry in wurtzite, and are set to zero in this work, since there are no reliable experimental values available.
The matrices Γ and G_{SO} are the same for both crystal structures and are given by

$$G_{SO} = \frac{i\Delta_{SO}}{3} \begin{pmatrix} 0 & 0 & 0 & 0 \\ 0 & 0 & -1 & 0 \\ 0 & 1 & 0 & 0 \\ 0 & 0 & 0 & 0 \end{pmatrix} \tag{2.33}$$

$$\Gamma = \frac{\Delta_{SO}}{3} \begin{pmatrix} 0 & 0 & 0 & 0 \\ 0 & 0 & 0 & 1 \\ 0 & 0 & 0 & -i \\ 0 & -1 & i & 0 \end{pmatrix} \tag{2.34}$$

where Δ_{SO} is the split-off energy.
The eigenvectors and eigenvalues of these Hamiltonians correspond to the electron- and hole wavefunctions and energies of the modeled quantum dots. We numerically calculate the states around the fundamental bandgap using an inner-eigenvalue solver, originally developed by Oliver Stier [33] and adapted to the wurtzite lattice structure by Momme Winkelnkemper [34]. The implementation is explored in further detail in the appendix in section A.1.

2.4.3 Valence-Band Structure

The basis chosen for the **k·p** model, referred to in the following as the Sxyz-basis, is convenient for the numerical implementation in rectangular coordinates. Additionally, the optical matrix elements in this basis are given simply by

$$\langle s| \mathbf{p_i} |j\rangle = \delta_{ij} P_i \quad , \quad i,j \in \{x,y,z\} \quad . \tag{2.35}$$

However, the Bloch-functions $|x\rangle$, $|y\rangle$ and $|z\rangle$ do not possess the same symmetry as the Bloch states that form the heavy-hole, light-hole and split-off bands in zincblende, or the A-, B- and C-bands in wurtzite. It is therefore necessary to expand the bloch-states corresponding to the highest valence bands into our rectangular bloch-basis. For wurtzite, this expansion is given by [31, 35]:

$$
\begin{aligned}
|A\uparrow\rangle &= \frac{1}{\sqrt{2}}(|x\uparrow\rangle + i\,|y\uparrow\rangle) && (2.36)\\
|A\downarrow\rangle &= \frac{1}{\sqrt{2}}(|x\downarrow\rangle - i\,|y\downarrow\rangle) && (2.37)\\
|B\uparrow\rangle &= \frac{1}{\sqrt{2}}a(|x\uparrow\rangle - i\,|y\uparrow\rangle) + b\,|z\downarrow\rangle && (2.38)\\
|B\downarrow\rangle &= -\frac{1}{\sqrt{2}}a(|x\downarrow\rangle + i\,|y\downarrow\rangle) + b\,|z\uparrow\rangle && (2.39)\\
|C\uparrow\rangle &= \frac{1}{\sqrt{2}}b(|x\uparrow\rangle - i\,|y\uparrow\rangle) - a\,|z\downarrow\rangle && (2.40)\\
|C\downarrow\rangle &= -\frac{1}{\sqrt{2}}b(|x\downarrow\rangle + i\,|y\downarrow\rangle) - a\,|z\uparrow\rangle && (2.41)
\end{aligned}
$$

where a and b are given by:

$$
\begin{aligned}
a &= \frac{1}{\sqrt{x^2+1}} && (2.42)\\
b &= \frac{x}{\sqrt{x^2+1}} && (2.43)\\
x &= \frac{-(3\Delta_{CR}-\Delta_{SO}) + \sqrt{(3\Delta_{CR}-\Delta_{SO})^2 + 8\Delta_{SO}^2} - \lambda_\epsilon}{2\sqrt{2}\Delta_{SO}} && (2.44)\\
\lambda_\epsilon &= D_1\epsilon_{zz} + D_2(\epsilon_{xx}+\epsilon_{yy}) && (2.45)
\end{aligned}
$$

In the case of zincblende, $\Delta_{CR} = 0$ and $\lambda_\epsilon = 0$, which then leads to the Bloch-functions for the three valence bands [26, 28]:

$$
\begin{aligned}
|HH\uparrow\rangle &= \frac{1}{\sqrt{2}}(|x\uparrow\rangle + i\,|y\uparrow\rangle) && (2.46)\\
|HH\downarrow\rangle &= \frac{1}{\sqrt{2}}(|x\downarrow\rangle - i\,|y\downarrow\rangle) && (2.47)\\
|LH\uparrow\rangle &= \frac{1}{\sqrt{6}}(|x\uparrow\rangle - i\,|y\uparrow\rangle) + \sqrt{\frac{2}{3}}\,|z\downarrow\rangle && (2.48)\\
|LH\downarrow\rangle &= -\frac{1}{\sqrt{6}}(|x\downarrow\rangle + i\,|y\downarrow\rangle) + \sqrt{\frac{2}{3}}\,|z\uparrow\rangle && (2.49)\\
|SO\uparrow\rangle &= \frac{1}{\sqrt{3}}[|x\uparrow\rangle - i\,|y\uparrow\rangle - |z\downarrow\rangle] && (2.50)\\
|SO\downarrow\rangle &= -\frac{1}{\sqrt{3}}[|x\downarrow\rangle + i\,|y\downarrow\rangle + |z\uparrow\rangle] && (2.51)
\end{aligned}
$$

These expansions can be used to understand the contribution of the respective valence bands to a calculated single-particle state. The set of basis functions obtained by these transformations will be referred to in the following as the SABC- or SHHLHSO-basis in the following.

2.5 Coulomb-interaction: Excitonic properties

Chapter 2.4 described the calculation of single-particle electron- and hole-states in quantum dots. In order to understand the luminescence of these quantum dot systems, however, it is necessary to include the Coulomb-interaction between different particles, leading to the formation of excitonic states. In this work, these interactions are treated by an iterative Hartree-Fock method.
We did not explore more advanced calculation techniques for the Coulomb-interaction, such as configuration interaction (CI), in this work because CI, while in theory providing more precise values for the excitonic energies, does not yield a well-defined excitonic wavefunction and charge density distribution. We, however, require the charge-density associated to the excitonic particles for our calculations of the Huang-Rhys factors, discussed in chapter 2.7.

2.5.1 Hartree-Fock

Consider a set ϕ_i of orthonormal single-particle solutions of the $\mathbf{k}\cdot\mathbf{p}$-Hamiltonian $\mathbf{H}_{kp}^{sp}$:

$$\mathbf{H}_{kp}^{sp}\phi_i = E_{kp}^{sp}\phi_i \quad ; \quad \langle\phi_i|\phi_j\rangle = \delta_{ij} \quad . \tag{2.52}$$

To account for Coulomb-interaction between the particles, we introduce an interaction operator $\mathbf{V}_{\text{Coulomb},i}$ for each particle, such that

$$\mathbf{H}_{HF} = \sum_{i=1}^{N}(\mathbf{H}_{sp,i}^{kp} + \mathbf{V}_{\text{Coulomb},i}) \tag{2.53}$$

$$\mathbf{V}_{\text{Coulomb},i} = \frac{1}{2}\cdot\frac{1}{4\pi\varepsilon_0\varepsilon_r}\sum_{j=1}^{N}\frac{q_i q_j}{|\mathbf{r}_i - \mathbf{r}_j|} \tag{2.54}$$

holds, where N is the number of particles in the multiparticle state. We now approximate the wavefunction Ψ_{HF} of the multi-particle state to be a Slater-determinant of the single particle states:

$$\Psi_{HF}(t_1, t_2, ..., t_N) = \frac{1}{\sqrt{N!}}\begin{vmatrix} \phi_1(t_1) & \phi_1(t_2) & ... & \phi_1(t_N) \\ \phi_2(t_1) & \phi_2(t_2) & ... & \phi_2(t_N) \\ ... & ... & ... & ... \\ \phi_N(t_1) & \phi_N(t_2) & ... & \phi_N(t_N) \end{vmatrix} \tag{2.55}$$

and calculate the energy E_{HF} of the multi-particle state:

$$E_{HF} = \langle\Psi_{HF}|\,\mathbf{H}_{HF}\,|\Psi_{HF}\rangle = \int \Psi_{HF}^{*}\mathbf{H}_{HF}\Psi_{HF}\mathrm{d}t_1...\mathrm{d}t_N \quad . \tag{2.56}$$

Expanding the left-hand determinant yields $N!$ terms that differ only in the order of their indices t_i, which can then be represented by a single one of these entries multiplied by $N!$.

Different signs in the single terms are compensated by changing the sign in the right-hand determinant where necessary.
After expanding the right-hand determinant, we can then eliminate all terms that contain multiplication of different single particle wavefunctions depending on the same set of coordinates, where these coordinates do not appear in the Hamiltonian, because of orthogonality:

$$\phi_i^*(t_k)\phi_j(t_k) = 0 \quad . \tag{2.57}$$

The remaining terms can then be grouped into three separate parts:

$$\begin{aligned} E_{HF} &= E_{sp} + E_{Coulomb} + E_{exchange} \\ E_{sp} &= \sum_{i=1}^{N} \int \phi_i^*(t_i) \cdot H_{sp,i}^{kp} \cdot \phi_i(t_i) \mathrm{d}t_i \qquad (2.58) \\ E_{coulomb} &= \frac{1}{2}\frac{1}{4\pi\varepsilon_0} \sum_{i,j}^{N} \int \frac{q_i q_j}{\varepsilon_r(\mathbf{r}_i)} \frac{\phi_i^*(t_i)\phi_j^*(t_j)\phi_j(t_j)\phi_i(t_i)}{|\mathbf{r}_i - \mathbf{r}_j|} \mathrm{d}t_i \mathrm{d}t_j \qquad (2.59) \\ E_{exchange} &= -\frac{1}{2}\frac{1}{4\pi\varepsilon_0} \sum_{i,j}^{N} \int \frac{q_i q_j}{\varepsilon_r(\mathbf{r}_i)} \frac{\phi_i^*(t_i)\phi_j^*(t_j)\phi_i(t_j)\phi_j(t_i)}{|\mathbf{r}_i - \mathbf{r}_j|} \mathrm{d}t_i \mathrm{d}t_j \qquad (2.60) \end{aligned}$$

E_{sp} represents the single particle energies of the N electrons/holes.
$E_{Coulomb}$ is the energy of the direct Coulomb-interaction between all pairs of particles, analogous to the Coulomb energy attributed to the interaction of classical charge distributions.
$E_{Exchange}$ is the exchange-part of the Coulomb-interaction, which does not have a classical analogon. It originates from the indistinguishability of the electrons. Note that for $i = j$: $E_{Coulomb} + E_{exchange} = 0$.
One can now employ a variational procedure on this expression for the energies, in order to obtain the wavefunctions ϕ_i:

$$\delta E^{HF} = \delta(E_{sp} + E_{Coulomb} + E_{exchange}) = 0 \quad . \tag{2.61}$$

Performing these variational calculations [36], one arrives at the Hartree-Fock equations

$$\left[H_i^{kp} + \sum_{j}^{N} \left(V_{\phi_j}^{Coulomb} - V_{ij}^{Exchange} \right) \right] \phi_i(t_i) = \lambda_i \phi_i(t_i) \quad . \tag{2.62}$$

The potential operators are given by

$$V_{\phi_j}^{Coulomb} = \int \frac{q_i q_j}{4\pi\varepsilon_0} \frac{1}{\varepsilon_r(\mathbf{r_j})} \frac{\phi_j^*(t_j)\phi_j(t_j)}{|\mathbf{r}_i - \mathbf{r}_j|} \mathrm{d}t_j \tag{2.63}$$

$$V_{ij}^{Exchange} = \int \frac{q_i q_j}{4\pi\varepsilon_0} \frac{1}{\varepsilon_r(\mathbf{r_j})} \frac{\phi_j^*(t_j)\phi_i(t_j)}{|\mathbf{r}_i - \mathbf{r}_j|} \mathrm{d}t_j \frac{\phi_j(t_i)}{\phi_i(t_i)} \quad . \tag{2.64}$$

Equation 2.62 is analogous to the situation for the single particle calculations described above, but with an additional potential containing direct Coulomb and exchange interaction. The difficulty is that this potential for particle i depends on the wavefunctions for all other particles in the multi-particle complex. Since these are not known beforehand, the N equations 2.62 are solved using an iterative scheme visualised in figure 2.1.

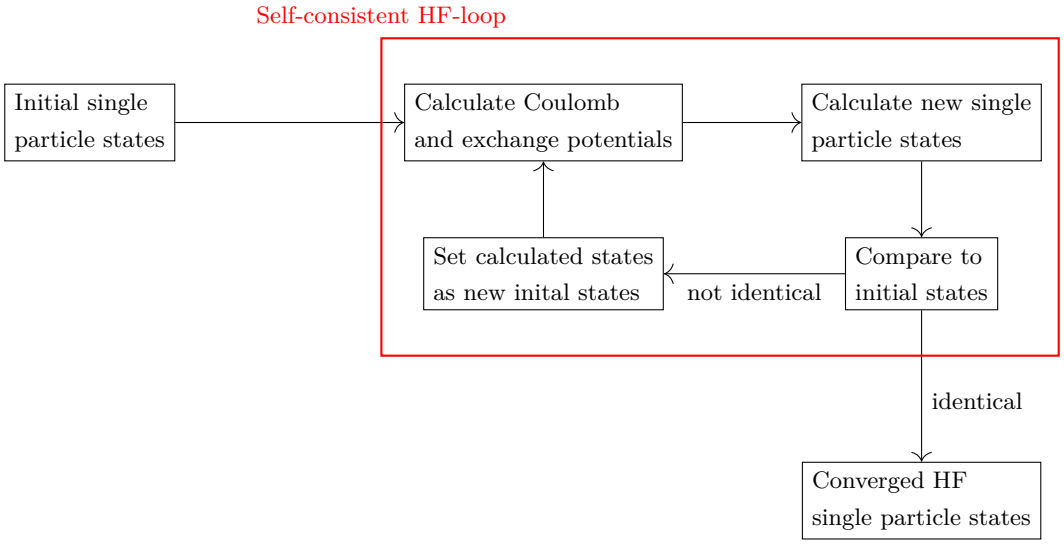

Figure 2.1: Iterative Hartree-Fock calculation scheme: Starting with the single particle states, Coulomb- and exchange-potentials are calculated. These are incorporated into the **k**·**p** Hamiltonian to calculate a new set of states. These new states are compared to the initial states, and, if they do not differ more than a predetermined threshold value, are the converged final exciton states. If there is still a significant difference, the calculated states are used as the input states for the next iteration of the Hartree-Fock loop

The iterative Hartree-Fock Scheme was implemented by Gerald Hönig for the wurtzite structure [37], and reimplemented for zincblende in this work.

2.6 Localised Phonons in Quantum Dots

This chapter outlines the concepts and methods used to obtain information about the dynamics of the atomic nuclei in the quantum dots.

2.6.1 Atomistic Approach

The Schrödinger-equation for the atomic cores in a solid is given by equation 2.4.
We model the vibrations as small deviations from the equilibrium positions $\mathbf{R}_i^{(0)}$:

$$\mathbf{R}_i = \mathbf{R}_i^{(0)} + \mathbf{u}_i \quad . \tag{2.65}$$

Following Czycholl [38] and using the abbreviation $\underline{\mathbf{R}} = (\mathbf{R}_1, ..., \mathbf{R}_N)$, we can expand the effective potential in powers of these deviations:

$$V_{eff}(\underline{\mathbf{R}}) = V_{eff}(\underline{\mathbf{R}}^{(0)}) + \sum_{i=1}^{N}\sum_{\alpha=1}^{3} \frac{\partial V_{eff}}{\partial R_{i\alpha}}|_{\underline{\mathbf{R}}^{(0)}} \cdot u_{i\alpha} + \frac{1}{2}\sum_{i,j=1}^{N}\sum_{\alpha,\beta=1}^{3} \frac{\partial^2 V_{eff}}{\partial R_{i\alpha}\partial R_{j\beta}}|_{\underline{\mathbf{R}}^{(0)}} u_{i\alpha}u_{j\beta} + ... \tag{2.66}$$

Since the equilibrium positions are minima in the potential energy surface, the first derivatives vanish. If we then cap the expansion after the quadratic term, we arrive at the harmonised effective potential for the atomic nuclei.
If we now perform a coordinate transformation into mass-weighted coordinates:

$$\bar{u}_{i\alpha} = \sqrt{M_i}u_{i\alpha} \quad , \quad \bar{p} = \frac{1}{\sqrt{M_i}}p_{i\alpha} \quad , \tag{2.67}$$

we can express the Hamiltonian as

$$H_{harm} = \frac{1}{2}(\underline{\bar{\mathbf{p}}}^T\underline{\bar{\mathbf{p}}} + \underline{\bar{\mathbf{u}}}^T D\ \underline{\bar{\mathbf{u}}}) \quad , \tag{2.68}$$

using the dynamical matrix D:

$$D_{i\alpha,j\beta} = \frac{1}{\sqrt{M_iM_j}}\Phi_{i\alpha,j\beta} = \frac{1}{\sqrt{M_iM_j}}\frac{\partial^2 V_{eff}}{\partial R_{i,\alpha}\partial R_{j,\beta}}|_{\underline{\mathbf{R}}^{(0)}} \quad . \tag{2.69}$$

Since we harmonised the potential, the matrix D is real, symmetric and positive definite, and can therefore be diagonalised by a suited orthogonal matrix C:

$$C \cdot D \cdot C^{\dagger} = \Omega \quad , \tag{2.70}$$

yielding the diagonal matrix of the eigenvalues of D, Ω.
After an orthogonal transformation of our coordinates, using $\underline{\bar{\mathbf{x}}} = C\underline{\bar{\mathbf{u}}}$, and a subsequent diagonalisation of the Hamiltonian, we arrive at:

$$H_{harm} = \frac{1}{2} \sum_{i=1}^{N} \sum_{\alpha=1}^{3} (\bar{p}_{i\alpha}^2 + \omega_i^2 \bar{x}_{i\alpha}^2) \quad . \tag{2.71}$$

For bulk-systems, the common description of phonons makes use of the translational symmetry of the crystal lattice. The phononic eigenmodes can thus be separated into the eigenmodes of the atoms in the unit cell, multiplied by a plane wave that extends these eigenmodes along the whole crystal.
For colloidal quantum dots, this translational symmetry is not present, as the quantum dot size is usually only a few nanometers.
To calculate the vibrational properties of these quantum dots, we therefore employ an atomistic method, modeling the interactions between the atoms with empirical pair potentials. We then necessarily have to calculate and diagonalise the dynamical matrix of the full system, which results in a size restriction on the systems that can be computed in reasonable time.

2.6.2 Effective Pair-Potentials

The last step to obtain the eigenmodes of the atomistic motion is therefore to define the effective potential $V_{eff}(\underline{\mathbf{R}})$ from equation 2.66. In our case, this is done by defining an effective pair-potential between all pairs of atomic nuclei inside the quantum dot, and taking the sum of all of these pairwise potentials.
The potential used to model the interactions between the nuclei is introduced by [16] for CdSe and extended to further materials in [39]:

$$V_{ij} = \frac{q_i q_j}{r_{ij}} + 4\epsilon_{ij} \left\{ \left(\frac{\sigma_{ij}}{r_{ij}} \right)^{12} - \left(\frac{\sigma_{ij}}{r_{ij}} \right)^{6} \right\} \quad , \tag{2.72}$$

where the first term represents the long-range Coulomb interaction and the second term is a Lennard-Jones potential modeling both the short-range repulsion and the Van-der-Waals attraction of the nuclei.
The indices i and j run over Cadmium, Selenium and Sulfur.
The parameters ϵ_{ij} and σ_{ij} for pairs of different atoms are constructed via the combining rules

$$\epsilon_{ij} = \sqrt{\epsilon_i \epsilon_j} \quad ; \quad \sigma_{ij} = \frac{1}{2}(\sigma_i + \sigma_j) \tag{2.73}$$

The parameter set used in references [16, 39] was obtained by fitting to experimental phonon dispersion data, with an emphasis on a good agreement with the acoustic phonon branches. We performed a refit on the same experimental data, focusing more strongly on the optical phonon branches, and obtained a separate set of parameters, which was used throughout this work. These parameters can be found in table C.3 in the appendix.

2.6.3 Calculation process

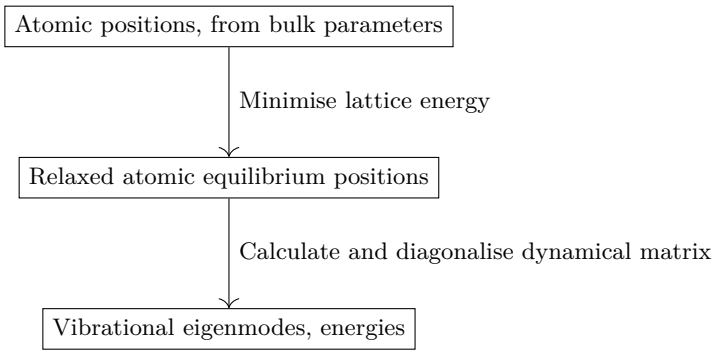

Figure 2.2: GULP calculation process: Starting from a set of atomic positions compiled from bulk lattice parameters, the lattice energy is iteratively minimised, leading to a set of relaxed atomic equilibrium positions. These are then utilised to determine the vibrational eigenmodes and their associated frequencies.

These potentials were then used, employing the GULP [17] program, to obtain the vibrational properties of the colloidal quantum dots.
The calculation procedure is outlined in figure 2.2 and consists of the following steps:

1. Create a set of atomic positions representing the quantum dot geometry, using the bulk lattice constants.

2. Using GULP, obtain a modified set of atomic positions, representing the equilibrium positions of the nuclei. These positions are created by minimising the total lattice energy.

3. Generate the dynamical matrix and diagonalise it, resulting in a complete set of vibrational eigenvectors, the phonons, and the corresponding eigenvalues, the phonon energies.

The implementation of these calculations is outlined in more detail in the appendix in section A.2.

2.6.4 Phonon analysis

Phonons in bulk lattices are easily classified by their symmetry as belonging to either an acoustic or optical phonon branch, and each phonon branch has an energy dispersion relation to their associated **k**-vectors.
The vibrational eigenmodes calculated above can not be as easily classified, for two reasons:

1. The absence of translational symmetry dictates that there is no dispersion in reciprocal space. As in the electronic calculations, we are limited to the Γ-point. For this reason, there are no phonon branches.

2. The eigenmodes can not be classified by their symmetry in any one unit cell. Therefore, we can not classify the vibrational modes into categories such as optical or acoustic.

Despite these limitations, we can still perform analysis on the vibrational eigenmodes. The following properties of the single eigenmodes yield valuable insight into the vibrational dynamics as a whole:

1. Localisation: How are the amplitudes of atomic motion distributed inside the quantum dot? Is the majority of the total amplitude limited to just a small area in the quantum dot or is it more evenly distributed throughout the system?

2. Core/Shell-modes: Are there modes where most of the vibrational amplitude is distributed inside the quantum dot core or the quantum dot shell?

3. Surface/Interface-modes: Similar to the core/shell-modes: Are there eigenmodes that exhibit most of their dynamics on atoms close to the surface or interface of the quantum dot?

In order to compute this information, we use the following method:

- Calculate a (normalised) scalar field $A(\mathbf{r})$ of amplitudes by adding a gaussian $g(\mathbf{r})$ at the position of each atom in the quantum dot, scaled by the vibrational amplitude a_j of the atom:

$$A(\mathbf{r}) = \sum_{j=1}^{N} g(\mathbf{r}_j) \cdot a_j \quad ; \quad \int A(\mathbf{r}) \mathrm{d}^3 r = 1 \quad . \tag{2.74}$$

  The variance of the gaussian function used is chosen to equal the mean distance between atoms.

- Calculate a (normalised) homogeneous scalar field $B(\mathbf{r})$ that is constant inside the quantum dot, and zero outside the quantum dot.

$$B(\mathbf{r}) = \begin{cases} \text{const} & ; \quad \mathbf{r} \text{ inside qd} \\ 0 & ; \quad \text{else} \end{cases} \quad ; \quad \int B(\mathbf{r}) \mathrm{d}^3 r = 1 \quad . \tag{2.75}$$

- The degree of localisation of the vibrational eigenmode is then given by:

$$l = \int |A(\mathbf{r}) - B(\mathbf{r})| \mathrm{d}^3 r \quad . \tag{2.76}$$

  If the amplitude distribution of an eigenmode would be completely homogeneously distributed over all atoms, the resulting scalar amplitude $A(\mathbf{r})$ field would be equal to the homogeneous scalar field $B(\mathbf{r})$, and therefore: $l = 0$. For eigenmodes with a lower degree of homogeneity, the value for l is increased, giving us a measure for phonon localisation.

- In order to determine the degree of motion amplitude d_R in a certain region R of the quantum dot, e.g. the surface or the interface, we simply calculate the sum of the amplitudes a_n of all the atoms inside the region, and then divide by the total amplitude a_{tot} of all atoms in the quantum dot. We then normalise this result by the volume fraction of the considered region in relation to the total quantum dot volume

$$d_R = \frac{V_{QD}}{V_R} \cdot \frac{1}{a_{\text{tot}}} \sum_{\substack{n, \\ n \text{ inside QD}}}^{N} a_n \quad . \tag{2.77}$$

  Thus, if $d_R = 1$, then the amplitude fraction inside the considered region is the same as the volume fraction of the region, and the eigenmode ist homogeneously distributed with regard to the considered region.

  Therefore, if $d_R > 1$, the eigenmode is more localised in the considered region than a homogeneous mode, and, for $d_R < 1$ the mode is less localised.

2.7 Electron-Phonon Interaction

The potential in equation 2.3 only depends on the equlibrium positions of the atomic nuclei. If we introduce atomic motion via the atomic displacements u_i, we can expand the potential around the equilibrium positions:

$$\begin{aligned} V(\mathbf{r}) &= \sum_{i=1}^{N} v(\mathbf{r}-\mathbf{R}_i) \\ &= \sum_{i=1}^{N} v(\mathbf{r}-\mathbf{R}_i^{(0)}-\mathbf{u}_i) \\ &= \underbrace{\sum_{i=1}^{N} v(\mathbf{r}-\mathbf{R}_i^{(0)})}_{V_{per}(\mathbf{r})} \underbrace{-\sum_{i=1}^{N} \nabla v(\mathbf{r}-\mathbf{R}_i^{(0)})\mathbf{u}_i}_{V_{el-ph(\mathbf{r})}} \quad . \end{aligned} \tag{2.78}$$

Hence, an additional potential term, proportional to the atomic displacements $\mathbf{u}_i$ is introduced in addition to the lattice periodic potential. This model for electron-phonon interaction is known as the Fröhlich-Model [40].

2.7.1 Huang-Rhys factors

Since there is an interaction between the electronic and vibrational properties in semiconductors, interactions of the electronic system with light, in the form of the formation or recombination of an exciton, can also couple to the vibrational system. This concept was first formalised by Huang and Rhys [41], who described it in the context of bulk phonons modifying the light-absorption properties of an F-center in diamond.
They introduced an electron-phonon coupling term H_{el-ph} into the Hamiltonian:

$$H = \sum_{\mathbf{k}} (\mathbf{p}_{\mathbf{k}}^2 + \omega_l^2 \mathbf{q}_{\mathbf{k}}^2 - \underbrace{\frac{1}{\sqrt{N}} \mathbf{A}'_{\mathbf{k}} \cdot \mathbf{q}_{\mathbf{k}}}_{H_{el-ph}}) \quad , \tag{2.79}$$

where $\mathbf{A}'_{\mathbf{k}}$ models the influence of the electric field $\mathcal{E}_{\mu'}$ of the F-center in the excitation state μ':

$$\mathbf{A}'_{\mathbf{k}} = \omega_l \left[\frac{1}{2\pi v_a} \left(\frac{1}{\epsilon_\infty} - \frac{1}{\epsilon_0} \right) \right]^{1/2} \int \mathrm{d}v \frac{\mathbf{k}}{|\mathbf{k}|} \mathcal{E}_{\mu'}(\mathbf{r}) \exp(i\mathbf{k}\mathbf{r}) \quad . \tag{2.80}$$

Since this new Hamiltonian is no longer diagonal in the original phonon coordinates, they introduce the following coordinate transformation:

$$\mathbf{q}'_{\mathbf{k}} = \mathbf{q}_{\mathbf{k}} - \frac{1}{\sqrt{N}} \frac{\mathbf{A}'_{\mathbf{k}}}{\omega_l^2} \quad , \tag{2.81}$$

which results in the following, diagonal Hamiltonian

$$H = \sum_{\mathbf{k}} (\mathbf{p}_{\mathbf{k}}^2 + \omega_l^2 \mathbf{q}_{\mathbf{k}}'^2 - \underbrace{\frac{1}{2\sqrt{N}} \frac{\mathbf{A}_{\mathbf{k}}'^2}{\omega_l^2}}_{E_{\mu',el-ph}}) \quad . \tag{2.82}$$

The two main physical consequences of the interaction between the phonons and the F-center are therefore:

- The electric field from the F-center shifts the coordinates of the phonon eigenmodes; they are still harmonic vibrations, but the equilibrium positions for the atomic nuclei are shifted by electron-phonon coupling, as detailed by the coordinate transformation in equation 2.81.
- The energy of the phononic system is changed by the constant $E_{\mu',el-ph}$.

If the F-center interacts with a photon, its excitation state is changed from μ' to μ'', and a parameter S is introduced which estimates the magnitude of the coupling with the phononic system for a given excitonic transition:

$$S = \frac{\hbar v_a}{2\omega_l^3} \int \mathrm{d}\mathbf{k} (A_{\mathbf{k}}' - A_{\mathbf{k}}'')^2 \quad . \tag{2.83}$$

This parameter is called the Huang-Rhys factor and is proportional to the square of the relative displacements of the equilibriom positions of the atomic nuclei introduced by the two different excitation states of the F-center.
The method employed in this work to calculate electron-phonon coupling in colloidal quantum dots is outlined in [19]. In contrast to the original work by Huang and Rhys, the electronic system now couples to the vibrational modes of the isolated quantum dots, not the bulk-phonons of the matrix material around an F-center.
We model the systems interaction with a phonon by assigning a different occupation of electronic states in the quantum dot to the state before the interaction and after the interaction.
In the simplest case, the emission of a photon from the quantum dot, before the emission the electron and hole ground-states would be occupied by one electron and hole, respectively, forming a ground-state exciton. This exciton would then recombine, emit one photon and result in no electronic states in the quantum dot being occupied thereafter.
We are not limited to this simple case, however, and can assume arbitrary occupations of the quantum dot for the before and after configurations. If we want to model photon emission, however, the state after the interaction should always be obtainable from the state before the interaction through the recombination of a single electron-hole pair.
We are, however, not numerically limited to these radiative recombination cases, and can numerically assume arbitrary electronic configurations for both the before state and the after state.
This gives us the ability to assess the coupling of the vibrational system to not just interactions of the electronic system with photons, but to any change in electronic configuration.

One example would be a spin-flip of an exciton, changing it from a dark to a bright state. If we assume a harmonic potential, the energies of the atomic lattice, when displaced by a small amplitude δ along a vibrational eigenmode $\mathbf{q}_i$,for these two different electronic configurations are given by

$$E_{g,i}(\delta) = \frac{\hbar\omega_i}{2}(\delta\mathbf{q}_i)^2 \quad , \quad E_{e,i}(\delta) = \frac{\hbar\omega_i}{2}(\delta\mathbf{q}_i - \Delta_i)^2 \quad , \tag{2.84}$$

where the Δ_i represents the displacement of the atomic equilibrium positions imposed by the changed electronic configuration, as introduced in equation 2.81, projected onto the phonon $\mathbf{q}_i$.
The energy-difference between excited and ground state, is then given by

$$E_{eg,i} = \frac{\hbar\omega_i}{2}(2\delta q_i\Delta_i + \Delta_i^2) \quad . \tag{2.85}$$

This allows us to express the displacement in the following way:

$$\Delta_i = \frac{1}{\hbar\omega_i}\frac{\mathrm{d}E_{eg,i}}{\mathrm{d}(\delta q_i)} \quad . \tag{2.86}$$

As shown above, the S-parameter, or Huang-Rhys factor is proportional to the square of the atomic equlibrium position displacement, and in our model is given simply by

$$S_i = \frac{1}{2}\Delta_i^2 \quad . \tag{2.87}$$

Since in colloidal quantum dots, there are a finite number of lattice vibrations, and not, as in bulk, a continuum of phonon states, we are able to assign a Huang-Rhys factor for each vibrational eigenmode, as opposed to integrating over the entire Brillouin-zone. This yields additional physical insight, as we know the energies of the vibrational eigenmodes, and can thus predict, which phonons will be more likely to couple to the excitonic transition. A global Huang-Rhys factor for the excitonic transition can simply be aquired by summing over all phonons:

$$S = \sum_i S_i \tag{2.88}$$

2.7.2 Numerical Procedure

The required information about the system is thus:

- Equlibrium positions and partial charges of all atoms in the quantum dot,
- Vibrational eigenmodes of the system in cartesian coordinates,

- Probability densities $|\Psi|^2$ of the electrons and holes in the quantum dot before and after the excitonic transition.

in order to calculate the displacements Δ_i according to equation 2.86, we need to calculate the difference in lattice energy for the two different electronic configurations at both the atomic equilibrium positions and the positions obtained when displacing the nuclei along the considered vibrational eigenmode.
The influence of the electronic states present in the quantum dot on the lattice energy is calculated by determining the charge density given by the probability density $|\Psi|^2$ of the wavefunctions. The partial charges Q_i of the atomic nuclei are then modified according to the value of the probability density value at their respective positions. These changes in the partial charges are then normalised, so that a wavefunction of an electron states introduces an additional charge of $-e$ into the system, while a hole-state introduces a charge of $+e$.
In the example of an exciton, consisting of an electron and a hole, the total additional charge would be zero, keeping the quantum dot charge-neutral. However, since the wavefunctions for the electron and hole are different, the distribution of partial charges is changed, leading to a change in lattice energy.
Since the change in lattice energy is brought about by the additional charge density which arises from the electronic wavefunctions, we consider only the Coulombic part of the lattice energy, neglecting the Lennard-Jones part of the interatomic potential given by equation 2.72.
We can therefore calculate the Coulombic part of the lattice energy for a given set of partial charges and positions of the atomic nuclei as:

$$E_C = \frac{1}{4\pi\epsilon_0\epsilon_r} \sum_{i<j=1}^{N} \frac{Q_i Q_j}{r_{ij}} \quad , \tag{2.89}$$

which allows us to calculate the derivative in equation 2.86 as a difference quotient, and subsequently yields the Huang-Rhys factors for any given electronic configurations and vibrational eigenmodes.

2.7.3 Phonon normalisation

It is worth noting, that equation 2.84 holds true only for normalised cartesian vibrational eigenmodes, which are defined by the property that when displacing the atomic equilibrium positions by one normalised phonon vector, the lattice energy is increased by $\hbar\omega_i/2$, with ω_i being the vibrational frequency associated to the vibrational eigenmode.
Since the vibrational eigenmodes calculated by GULP are not normalised in this way, we have to determine normalisation factors, to arrive at properly normalised Huang-Rhys factors.
To achieve this, we calculate the lattice energies $E_g(\delta_n)$ at several multiples δ_n of the phonon eigenmode.
We can then utilise equation 2.84 to fit a parabolic function

$$E_{parabolic}(\delta) = a \cdot \delta^2 + b \tag{2.90}$$

to the obtained energies, and can then derive a normalisation factor, such that

$$E_{parabolic}(\delta = 1) = E_{parabolic}(\delta = 0) + \hbar\omega_i/2 \quad . \tag{2.91}$$

These normalisation factors have to be calculated for every vibrational eigenmode, in order to obtain correct Huang-Rhys factors.

3 Prior theoretical work

Electronic properties of spherical semiconductor quantum dots have been a topic of interest for a long time.
Electronic structure calculations for spherical systems were first reported by Efros [12], approximating the structures as a spherical potential well of infinite height. He then calculated wavefunctions and energies, based on earlier work on spherical impurity states in semiconductors [11, 10].
The electron energies are determined to be [13]:

$$E_{1S} = \frac{\hbar^2 \pi^2}{2 m_e a^2} \tag{3.1}$$

with the radius of the quantum dot a , while the wavefunctions are given by

$$\Psi_\alpha(\mathbf{r}) = \sqrt{\frac{2}{a}} \frac{\sin(\pi r/a)}{r} Y_{00}(\Omega) | S\alpha >, \tag{3.2}$$

while the hole energies are

$$E_{3/2}(\beta) = \frac{\hbar^2 \varphi^2(\beta)}{2 m_{hh} a^2} \quad , \tag{3.3}$$

where $\beta = m_{lh}/m_{hh}$ is the ratio of light-hole to heavy-hole mass and $\varphi(\beta)$ is the first root of the following equation:

$$j_0(\varphi) j_2(\sqrt{\beta}\varphi) + j_2(\varphi) j_0(\sqrt{\beta}\varphi) = 0 \quad . \tag{3.4}$$

The $j_n(x)$ are spherical Bessel functions. The hole wavefunctions are expressed by:

$$\Psi_M(\mathbf{r}) = 2 \sum_{l=0,2} R_l(r) (-1)^{M-\frac{3}{2}} \times \sum_{m+\mu=M} \begin{pmatrix} \frac{3}{2} & l & \frac{3}{2} \\ \mu & m & -M \end{pmatrix} Y_{lm}(\Omega) u_\mu \quad , \tag{3.5}$$

where the Y_{ii} denotes a spherical harmonic function, the expression in the brackets is a Wigner-3j-symbol und the u_μ are the Bloch-functions of the valence band Γ_8, given by

$$u_{3/2} = \frac{1}{\sqrt{2}}(X+iY)\uparrow \quad , \tag{3.6}$$

$$u_{-3/2} = \frac{1}{\sqrt{2}}(X-iY)\downarrow \quad , \tag{3.7}$$

$$u_{1/2} = \frac{i}{\sqrt{6}}[(X+iY)\downarrow -2Z\uparrow] \quad , \tag{3.8}$$

$$u_{-1/2} = \frac{i}{\sqrt{6}}[(X-iY)\uparrow +2Z\downarrow] \quad . \tag{3.9}$$

$$\tag{3.10}$$

And $R_l(r)$ describes the radial dependency of the wavefunctions, given by

$$R_2(r) = \frac{A}{a^{3/2}}\left[j_2(\varphi r/a) + \frac{j_0(\varphi)}{j_0(\varphi\sqrt{\beta})}j_2(\varphi\sqrt{\beta}r/a)\right] \quad , \tag{3.11}$$

$$R_0(r) = \frac{A}{a^{3/2}}\left[j_0(\varphi r/a) + \frac{j_0(\varphi)}{j_0(\varphi\sqrt{\beta})}j_0(\varphi\sqrt{\beta}r/a)\right] \quad . \tag{3.12}$$

A is a normalization constant, and the j_n, β and φ are the same functions used for the electron states.

Note the similarity of the hole Bloch-functions to the valence-band Bloch-function transformations utilized for the $\mathbf{k}\cdot\mathbf{p}$-implementation used in this work.

Based on these results for the single-particle states, extensive work has been done to compute multiparticle states, focusing strongly on exciton finestructure, bright- and dark-states [13], and also biexcitons [14].

To compute excitonic states on the basis of the single-particle states introduced above, an interaction Hamiltonian is introduced for the eight excitonic product-wavefunctions $\Psi_{\alpha,M} = \Psi_\alpha(r_e)\Psi_M(r_h)$ leading to five distinct exciton energy-levels, named for their total spin: $0^U, 0^L, \pm1^U, \pm1^L, \pm2$. The energies are then calculated for quantum dots of different sizes and shapes.

Radiative rates for the various excitons are calculated as well, finding that the ±2 and 0^L exciton levels are optically forbidden dark-states, while the other excitons are bright states.

It is noted that the lowest-energy exciton is always a dark-state, seemingly in contradiction with experimental evidence [15] of luminescence attributed to this ground-state.

This incongruence has led to the proposal of several mechanisms enabling the dark-state to become optically active, including interactions with magnetic fields [13, 15], phonon-assisted recombination [15], or coupling to magnetic polarons formed by dangling bonds on the quantum dot surface [42].

What all of the above works have in common, however, is the assumption of complete spherical symmetry, leading to electronic wavefunctions reproducing this symmetry. It is therefore difficult to assess the impact of e.g. electric polarization fields, which break this spherical symmetry, on the electronic structure.

The aim of this work is to integrate strain and internal electric potentials, and analyse their impact on the energies and radiative behaviour of the excitons found in these quantum

dots.

The single-particle results from Efros *et al* have been utilized by Kelley [18, 19] to study electron-phonon coupling in CdSe colloidal quantum dots. She proposed the model used in this work and outlined in detail in chapter 2.7.2, to calculate Huang-Rhys factors for different CdSe quantum dots. The result was, that only very few vibrational eigenmodes display notable exciton-phonon coupling strength, and those who do are located at only two distinct frequency ranges: at very low wavenumbers and around 200 cm^{-1}, which is close to the frequency of the bulk LO-phonon of CdSe.

These results proved the validity of the coupling model, and allowed for the analysis of the dependance of exciton-phonon coupling strength and phonon energies on the geometry of the quantum dots.

In a further work [43], the impact of surface phonons on the Huang-Rhys factors was examined, but only for single-material CdSe quantum dots.

Recently, a study [44] has been published that discusses the influence of piezoelectricity on the electronic wavefunctions in colloidal core-shell quantum dots. In this work, multiband $\mathbf{k}\cdot\mathbf{p}$-theory is used to assess the impact of piezoelectric potentials on the wavefunction separation of excitons in wurtzite colloidal CdSe/CdS quantum dots of varying shape. It is found, that the piezoelectricity leads to wavefunction separation and increase in radiative lifetimes. The role of pyroelectricity, however, was not accounted for.

4 Strain and Electrical Potentials

4.1 Strain distribution

The results of the strain calculations are displayed for one quantum dot geometry A2-6 in figure 4.1 for wurtzite lattice structure and in figure 4.2 for zincblende lattice structure. The figures show hydrostatic and biaxial strain values, as defined in chapter 2.2, on three two-dimensional cuts through the quantum dot center along the x-, y- and z-directions, respectively. Furthermore, the following shear strain-components are displayed:

- ε_{xy}, plotted along the xy-plane
- ε_{xz}, plotted along the xz-plane
- ε_{yz}, plotted along the yz-plane

The shear strain components are not displayed along any other planes, because their values are zero there.
The results for both lattice structures are quite similar and exhibit the following notable common features:

- The quantum dot core displays hydrostatic compressive strain, that is homogeneous inside the core. The shell displays tensile strain, which is also homogeneously distributed through the whole shell. This is the direct result of the larger lattice constant of Cadmium Sulfide compared to Cadmium Selenide. The magnitude of the hydrostatic strain of the core region is larger than that of the tensile strain in the shell, which can be attributed to the shell having the larger total volume in this geometry.
- The biaxial strain resides almost exclusively in the quantum dot shell, vanishing almost completely inside the core. There are two regions of positive biaxial strain at the core-shell interface oriented along the [001]-direction (or [0001]-direction for wurtzite) and a ring of negative biaxial strain near the interface, oriented in the (001)-plane (or (0001)-plane for wurtzite).
- The shear strain components are negligible inside the quantum dot core. Inside the shell, all three shear strains display a similar shape in their respective planes, having alternating positive and negative peaks along the diagonals, while vanishing along the principal axes.

The differences between the two lattice structures are the following:

- While the values for the hydrostatic strain are very similar between the two lattice structures, the biaxial strain is slightly more pronounced for the zincblende lattice structure.
- In contrast to that, the shear strain amplitudes are more pronounced in the wurtzite lattice structure.

- Since in zincblende there is no preferred axis inside the crystal, and our exemplary quantum dot geometry is also perfectly symmetrical, the plotted shear strain values are interchangeable for all three shear strains. In the wurtzite case, the [0001]-axis is a preferred axis of the crystal, and therefore the values for ε_{xy} are slightly smaller than for the two other shear strains, which are again interchangeable.

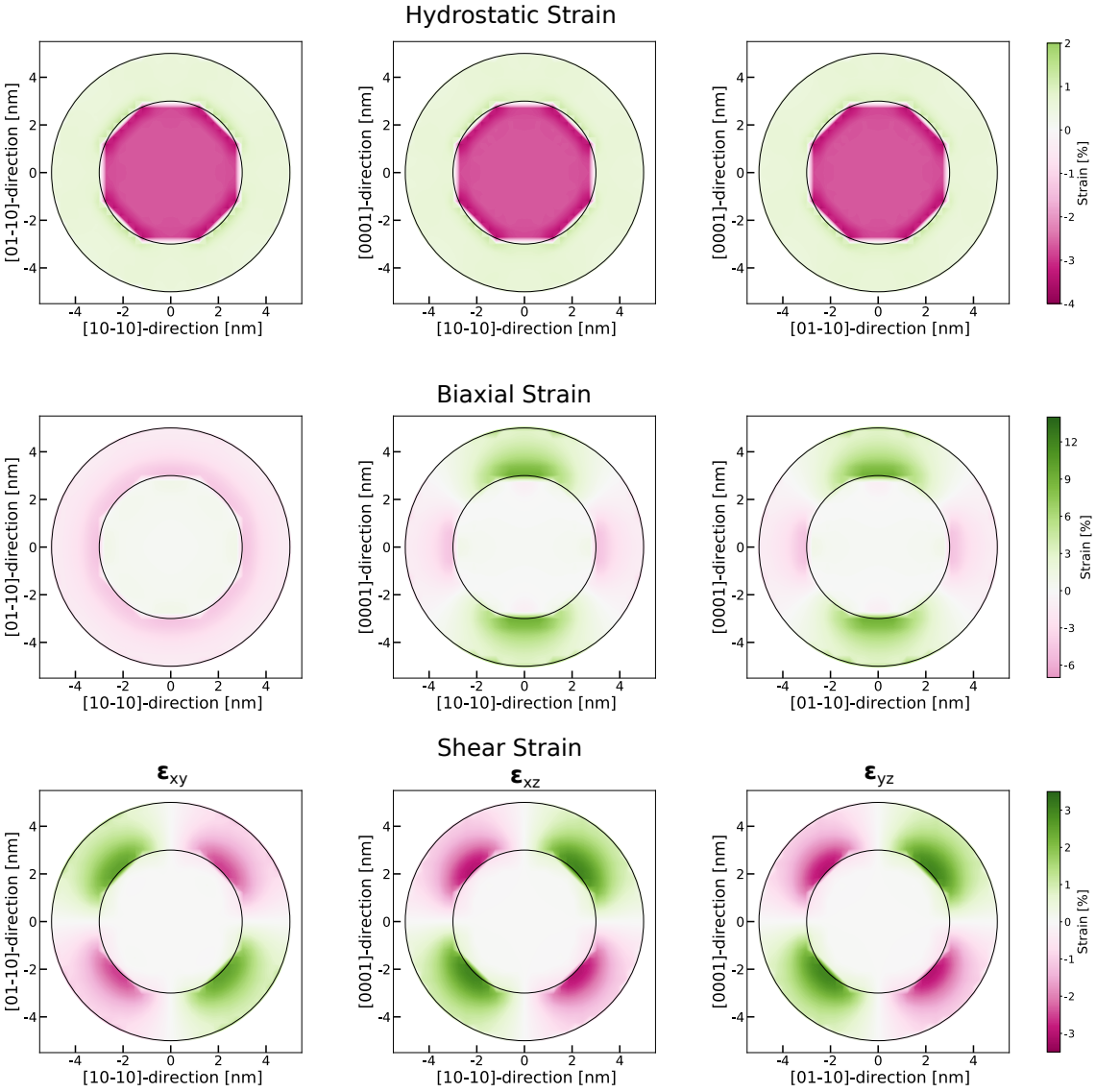

Figure 4.1: Strain distribution for quantum dot geometry A2-6 with wurtzite lattice structure. All data is plotted on 2D-cuts along the xy-plane, xz-plane and yz-plane respectively. All 2D-cuts are incorporating the quantum dot center. In the first row, the hydrostatic strain components are displayed, showing a homogeneous compressive strain inside the quantum dot core and a homogeneous tensile strain in the quantum dot shell. The second row of plots displays the biaxial strain component. The values for the xz- and yz-planes are identical, showing positive values in the shell above and below the core along the lattice c-axis, while the xy-plane displays homogeneous positive entries in the core and homogeneous negative values in the shell. In the third row, the three different shear strain components ε_{xy}, ε_{xz} and ε_{yz} are displayed in the respective 2D-cuts. All three shear strains show a similar symmetry, yet the amplitude for ε_{xy} is slightly diminished compared to the other two shear strain components.

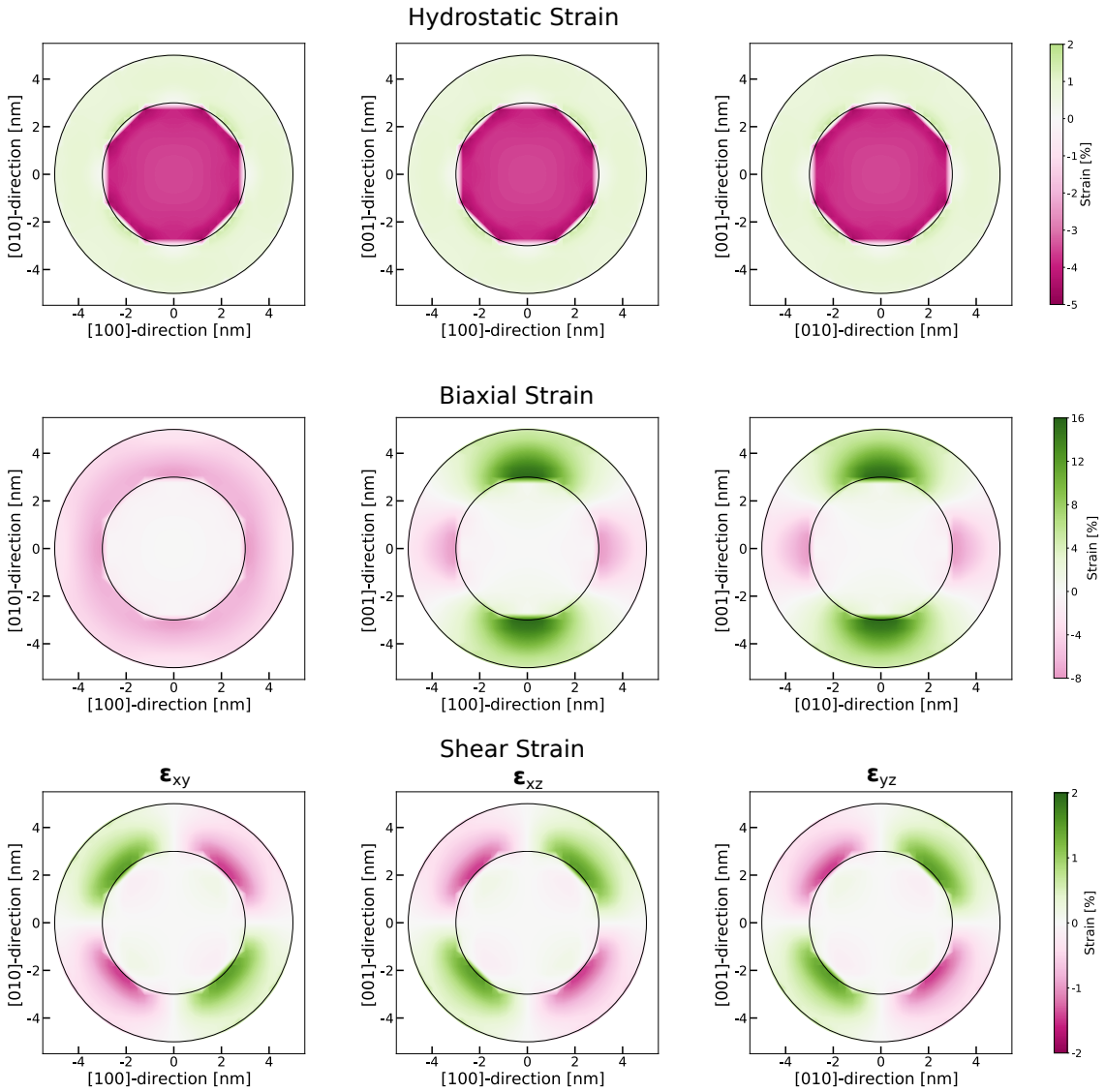

Figure 4.2: Strain distribution for quantum dot geometry A2-6 with zincblende lattice structure. All data is plotted on 2D-cuts along the *xy*-plane, *xz*-plane and *yz*-plane respectively. All 2D-cuts are incorporating the quantum dot center. In the first row, the hydrostatic strain components are displayed, showing a homogeneous compressive strain inside the quantum dot core and a homogeneous tensile strain in the quantum dot shell. The second row of plots displays the biaxial strain component. The values for the *xz*- and *yz*-planes are identical, showing positive values in the shell above and below the core along the lattice *c*-axis, while the *xy*-plane displays homogeneous neutral entries in the core and homogeneous negative values in the shell. In the third row, the three different shear strain components ε_{xy}, ε_{xz} and ε_{yz} are displayed in the respective 2D-cuts. All shear strains show an identical symmetry and identical amplitudes, which is due to the zincblende lattice having no preferred axis.

4.2 Piezoelectric and Pyroelectric Potentials

Calculated piezoelectric and pyroelectric potentials for quantum dot geometry A2-6 are plotted in figure 4.3. The potentials are displayed both as 3D-isosurfaces and 2D-contourplots on cuts through the quantum dot center.

In addition, linescans of the potentials for quantum dots with several different core-sizes

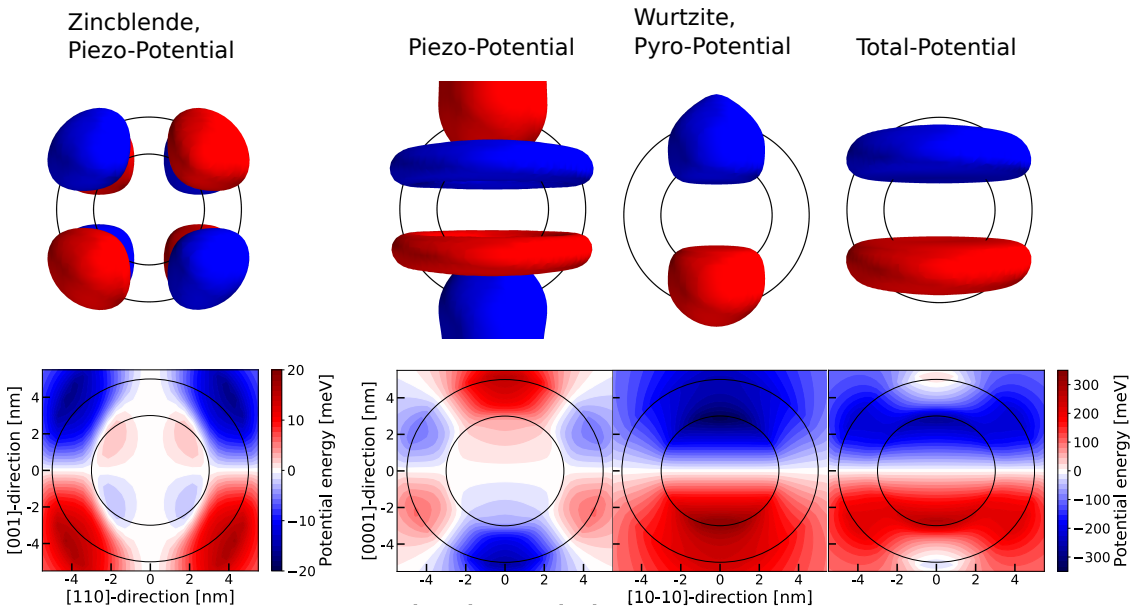

Figure 4.3: Piezo- and Pyroelectric potentials for both zincblende and wurtzite lattice structure for quantum dot geometry A2-6. In the top row, 3D isosurface plots of the potentials are displayed, while in the bottom row, 2D contour-plots of the same potentials are shown. The 3D plots are oriented so that the xz-plane is perpendicular to the viewing direction, with the z-axis pointing upward. The 2D cuts for these plots are along the [110]- and [100]-directions for the zincblende lattice structure, and along the [10-10]- and [0001]-directions for the wurtzite lattice structure. Positive values are depicted in red, while negative values are depicted in blue. In the leftmost column, the piezoelectric potential for the zincblende lattice structure is shown. The 3D plot shows alternating maxima and minima along the [111] group of directions. In the second column, the piezoelectric potential for the wurtzite lattice structure is displayed, showing a polarisation along the z-axis, with two torus-shaped regions of opposite polarisation in the shell region. The third column is displaying the pyroelectric potential for the wurtzite lattice structure, showing a strong polarisation along the z-axis, opposite to the piezoeletric potential. The fourth column depicts the total potential for the wurtzite case, showing a polarisation in the same direction as the pyroelectric potential, due to its higher amplitude compared to the piezoelectric potential.

from series A2 are displayed in figure 4.4. The total radius of all these quantum dots is 5nm.

We observe several key differences between the two lattice structures:

- The shape of the piezoelectric potentials is completely different between the different lattice structures. For zincblende, the potential has alternating maxima and minima along the space-diagonals, thus replicating the symmetry of the zincblende lattice, which has no preferred axis. For wurtzite structure, however, the piezoelectric potential is aligned along the lattice c-axis, inducing an electric field in this direction.

- The amplitude of the piezoelectric potential is an order of magnitude higher in the wurtzite lattice structure.

For both lattice structures, the piezoelectric potentials are much stronger in the quantum dot shell, compared to the core.

The pyroelectric potential of the wurtzite quantum dot has an even larger magnitude than the piezoelectric potential, and also displays a gradient along the lattice c-axis. These two

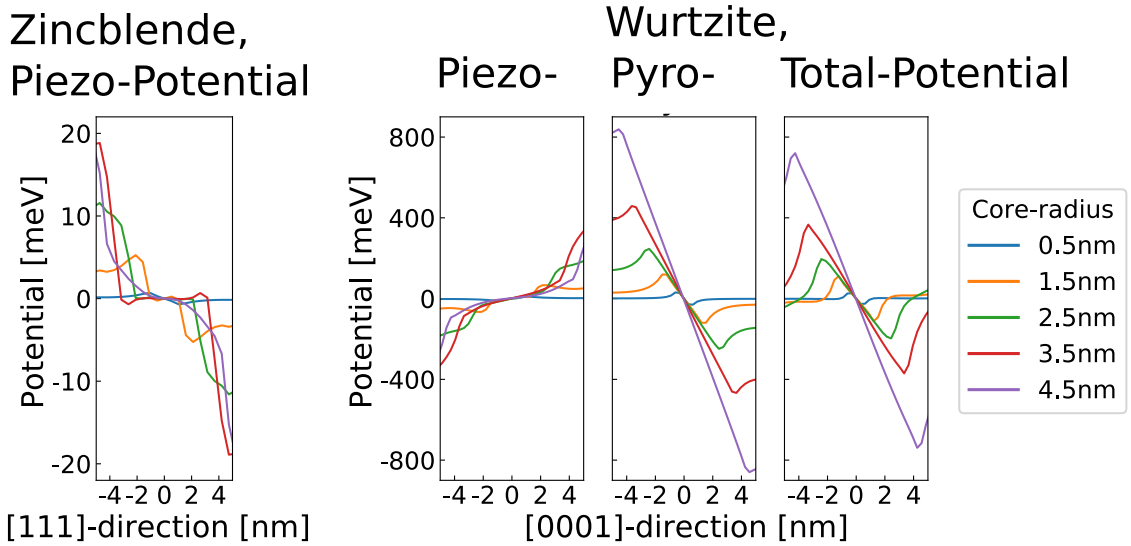

Figure 4.4: Linescans of the piezo- and pyroelectric Potentials for both zincblende and wurtzite lattice structure for quantum dots of series A2. The leftmost plot shows linescans of the piezoelectric potential for the zincblende case along the [111]-direction, showing increased potential amplitudes for increasing core diameters. Along with the increasing amplitude, the potential maxima and minima shift outwards following the core-shell interface. The three plots on the right side show linescans of the piezoelectric, pyroelectric- and total potential for the wurtzite case, respectively. All linescans are along the [0001]-direction. The piezoelectric potential shows a similar trend to the zincblende case, albeit with a much stronger amplitude. The pyroelectric potential has a linear slope inside the quantum dot core, which increases in steepness for increasing core diameter. Outside of the core, the potential decreases on an exponential slope. The total potential has a shape very similar to the pyroelectric potential, yet slightly decreased in amplitude by the piezoelectric part, which has an antiparallel polarisation.

gradients, however, have opposing signs, leading to the total potential displaying a slightly smaller potential gradient than the pyroelectric potential.

The potential gradient along the c-axis for wurtzite can be studied in more detail in the linescans in figure 4.4: inside the core, the potential decreases linearly, leading to a constant electric field inside the quantum dot core. This electric field is increased for larger core sizes, due to the pyroelectric potential gradient being larger for larger cores, while the gradient of the piezoelectric potential remains largely constant inside the core for varying core sizes.

For zincblende, the linescans are taken along the [111]-direction, as the potential vanishes on all principal axes. For larger core sizes, the potential values in the quantum dot shell increase, yet inside the core, the potential remains approximately zero, therefore inducing no electric field inside the core.

4.3 Influence of the dielectric environment

In our calculations, the relative permittivity, ε_r, is position dependent, as it is a property of the material found at the respective position. Furthermore, changing the permittivity at one position alters the resulting potential not only at this position, but globally.

This implies that we have to assign a value for the relative permittivity of the spacial region outside of the quantum dot. Because colloidal quantum dots are not embedded in a well-defined matrix material, this value is difficult to assess. The quantum dots can

be surrounded by air or vacuum, by a variety of polymer coatings, or be in solution in water, meaning that the relative permittivity of the quantum dot environment can be in the range of 1-80 [45, 46].
We have therefore calculated the potentials for one quantum dot geometry (A2-6) for a range of values of the environment ε_r.
2D contour-plots of these potentials are shown in figure 4.6, while linescans of the same potentials are displayed in figure 4.5.
We can draw several conclusions from these calculations:

- The effects of the change of relative permittivity are mostly affecting the potentials in the quantum dot shell and in the area outside the quantum dot. The changes observed inside the quantum dot core are relatively minor.
- For wurtzite, the changes in the piezo- and pyroelectric potentials inside the quantum dot core mostly offset each other, leading to an almost constant total potential inside the quantum dot core for the whole range of values for the environment permittivity.

Because of the smaller bandgap of the quantum dot core compared to the shell, we expect most wavefunctions to be largely confined to the core, where the electric potential ist not drastically changed by the environment permittivity. Therefore, all further calculations are performed with the environment permittivity $\varepsilon_r = 1$.
It is worth noting, however, that for quantum dots with thin shells, there could be a non-negligible influence of the dielectric environment on the electronic structure of the quantum dots.

4.3.1 Surface charges

As introduced in chapter 2.3, pyroelectricity is modeled by a single material parameter. This in turn leads to charges arising at material interfaces, where the value of this parameter changes. Since the outside of the quantum dot is not a semiconductor material, there is no reasonable value we can assign to the pyroelectric parameter outside of the quantum dot area.
However, setting it to zero would introduce large charge densities at the quantum dot surface. This would be an unphysical result, since the calculation method employed here is only valid for interfaces of semiconductor materials. Additionally, we can not account for any charged particles in the environment, which could be attracted by the surface charges, and could to some extent neutralise them.
Since we do not possess a viable method for determining the charge densities at the quantum dot surface, we artificially set them to zero for all calculations. Note, that for the case of neutralisation of the charges by additional charges in the quantum dot environment, this would be the correct result.
If the quantum dots were, for example, in solution in water, one would expect any surface charges to be neutralised by the partial charges of the water molecules. The same principle applies for any other kind of charged particles in the quantum dot environment, which makes the artificial omission of these surface charges a realistic approximation of the true charge densities at the surface.

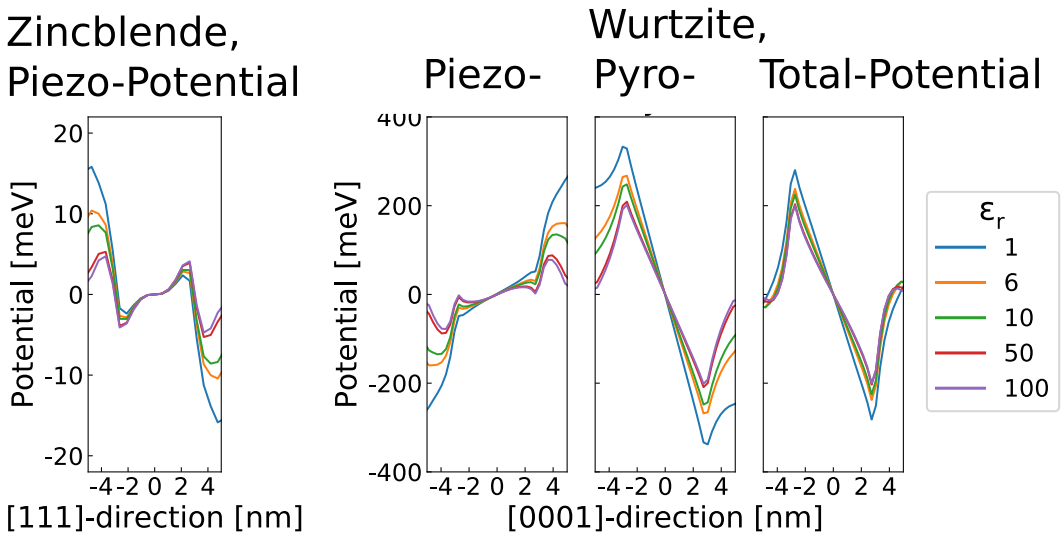

Figure 4.5: Linescans of the electric potentials for zincblende and wurtzite lattice structures for varying values between 1 and 100 of the dielectric permittivity of the environment for quantum dot geometry A2-6. The leftmost plot displays the results for the zincblende case, plotted along the [111]-direction. The potential inside the quantum dot core is not strongly affected by the change in permittivity, while the potential values in the quantum dot shell are increasingly diminished with increasing values of ε_r. The three plots on the right side depict the linescans of the Piezoelectric, Pyroelectric and total potential for the wurtzite lattice structure, plotted along the [0001]-direction. Here, the change in potential is also more pronounced in the quantum dot shell, but clearly noticeable inside the quantum dot core, as well.

4.3.2 Band-edge energies

The band-edges inside the quantum dot are affected by both strain and electric potentials. The band-edge energies for one exemplary quantum dot geometry are plotted for wurtzite lattice structure in figure 4.7 and for zincblende lattice structure in figure 4.8. The results are displayed both in a 2D contour-plot through the quantum dot center, as well as using linescans along the [0001]-direction (or [001]-direction in the case of zincblende).

For zincblende structure, the bandgap in the quantum dot core is slightly decreased, while the bandgap in the shell is slightly increased. This can be attributed to the effects of the hydrostatic strain, displayed in figure 4.2. The observed shifts are distributed homogeneously across the entire core and shell area. The effect of the electric potential is not observable in the plot, being negligible compared to the strain-induced energy shifts.

In the wurtzite case, we also observe a slight homogeneous shift in the bandgap effected by the hydrostatic strain. Much more pronounced, however, is the potential gradient along the c-axis introduced by the electric potential, which is particularly strong inside the quantum dot core.

Since the bandgap is smallest inside the core, we expect the electron and hole wavefunctions to be localised there. Therefore we should expect the potential to induce the separation of wavefunctions as well as a strong impact on the calculated energies of both electrons and holes.

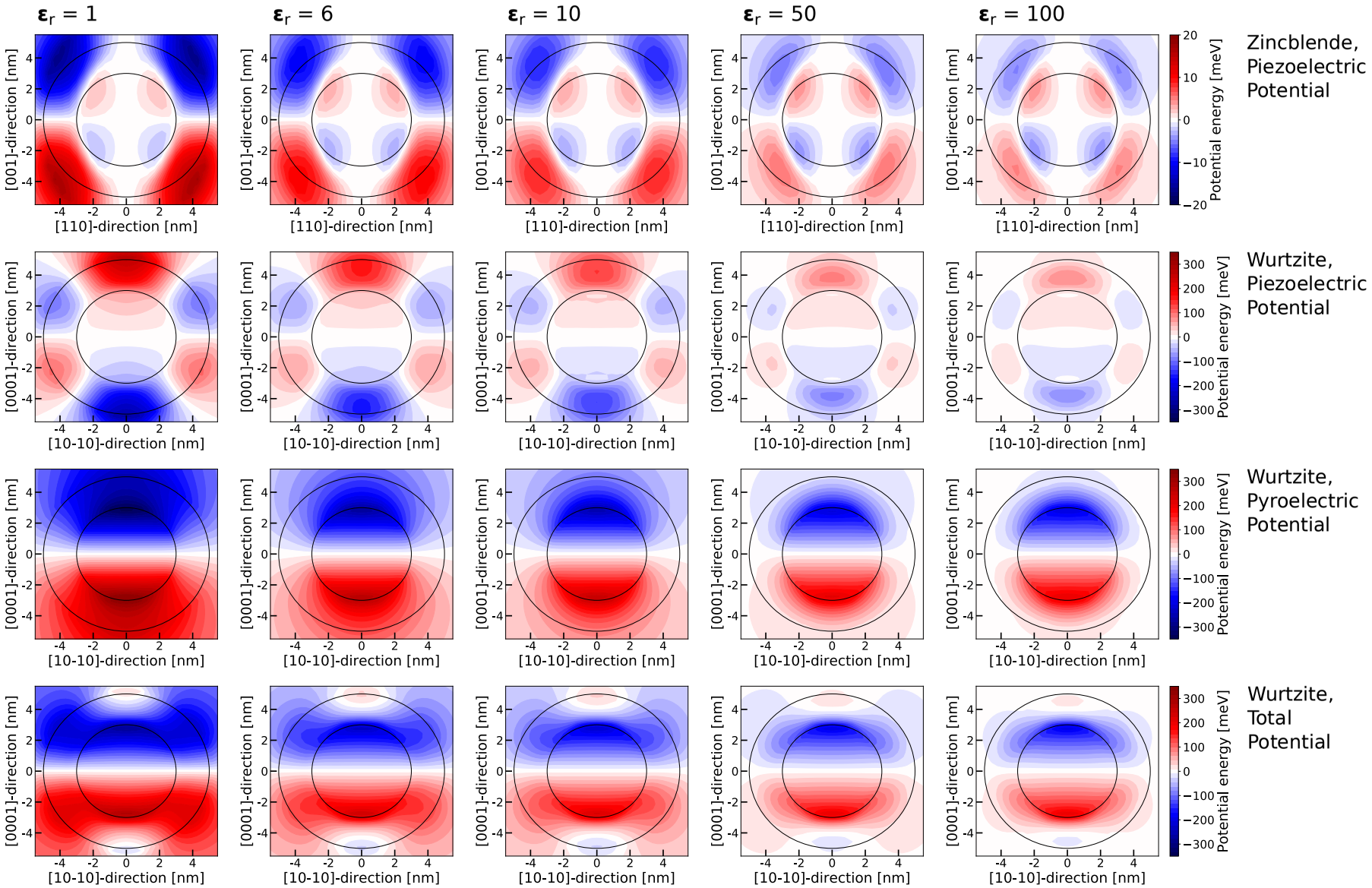

Figure 4.6: 2D-plots of potentials for an quantum dot geometry A2-6 for both zincblende and wurtzite lattice structure with varying values of relative dielectric permittivity of the environment: The top row of plots depicts the piezoelectric potentials for zincblende, plotted along the [110]- and [001]-directions. The second to fourth row show the piezoelectric, pyroelectric and total potential for wurtzite, respectively. These are all plotted along the [10-10]- and [0001]-directions. The columns correspond to increasing values of ε_r from 1 to 100, from left to right. The amplitude of all depicted potentials is strongly decreased in the quantum dot shell and the quantum dot environment for increasing environment permittivity, while the potentials inside the quantum dot core are not strongly affected.

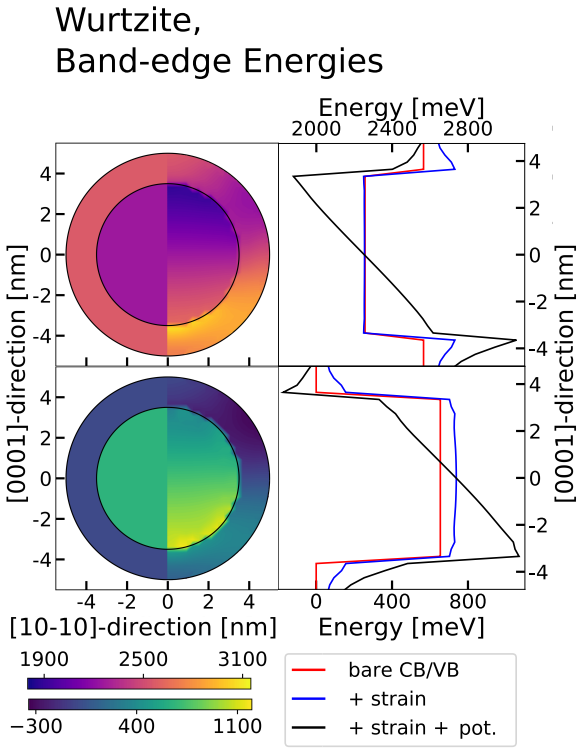

Figure 4.7: Calculated band-edge energies for quantum dot geometry A2-7 for wurtzite lattice structure. The top two images show the conduction band, the bottom two images show the highest-energy valence band. On the left side, a 2D-contour plot through the quantum dots center is displayed, while on the right side, a linescan along the *c*-axis is shown. For the linescan, the band-edges are shown with and without the effects of strain and electric potentials.

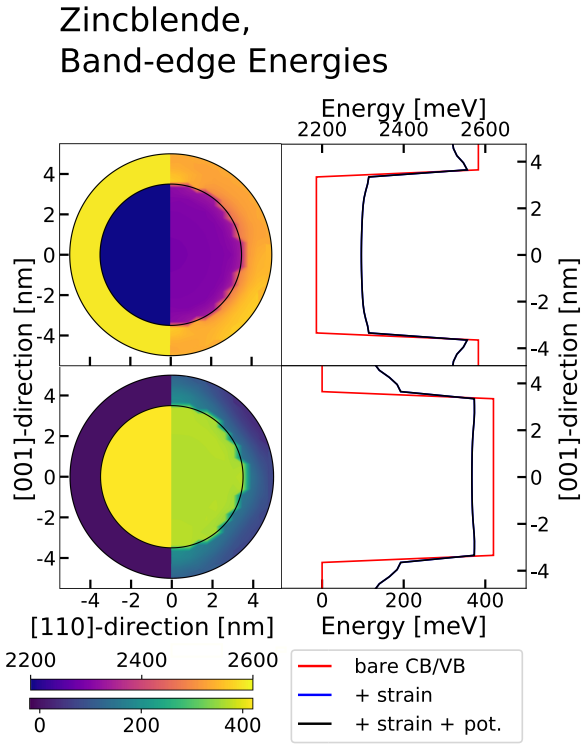

Figure 4.8: Calculated band-edge energies for quantum dot geometry A2-7 for zincblende lattice structure. The top two images show the conduction band, the bottom two images show the highest-energy valence band. On the left side, a 2D-contour plot through the quantum dots center is displayed, while on the right side, a linescan along the [001]-direction is shown. For the linescan, the band-edges are shown with and without the effects of strain and electric potentials.

4.3.3 Multishell Quantum dots

This work is mainly focused on core-shell quantum dots. It is, however, possible to fabricate colloidal quantum dots with arbitrary numbers of shells, making use of a variety of semiconductor materials [47, 48]. These quantum systems have been called "nano-onions" in some publications [49].
In this section, we will explore the effects on the calculated potentials of adding additional shells to the core-shell quantum dots, alternating CdS and CdSe for each additional shell. Figure 4.9 shows the calculated potentials of quantum dots from series C with wurtzite lattice structure with 2, 3, 4 and 5 shells, respectively. All potentials are displayed as 2D contour-plots as well as linescans along the [0001]-direction. Here, we only examine quantum dots with wurtzite lattice structure, as the electric potentials are much more pronounced in this case.
Examining the piezoelectric potential, we can see that the general shape of the potential of a quantum dot with a single shell, as depicted in figure 4.3, is repeated for each additional shell, with alternating signs. For each additional shell, the potential amplitude is increased. This leads to the formation of an alternating potential landscape, where the overall slope along the c-axis is dependent on the number of shells being even or odd, because of the dominant effect of the potential associated to the outermost shell. One can see from the linescans, that the values of the piezoelectric potentials of the quantum dots with an even number of shells are increasing along the c-axis, while for quantum dots with odd number of shells the potential values are decreasing overall.
Deviations between the quantum dots with different numbers of shells are more pronounced toward the surface of the quantum dot, whereas they are very similar in the area of the core and the innermost shell.
The pyroelectric potentials display an even stronger dependancy on the number of shells, as the overall gradient along the c-axis is almost completely reversed between quantum dots with odd or even numbers of shells, respectively. One can see in the linescan plot, that the potentials for 2 and 4 shells are almost perfectly identical inside the inner 2 shells, as are the potentials for 3 and 5 shells inside the inner 3 shells.
In contrast to the piezoelectric potential, however, the pyroelectric potential inside the quantum dot core is also strongly affected by the number of shells. For an odd number of shells, there is a strong potential gradient along the c-axis inside the core, as is the case for the basic core-shell quantum dot. For an even number of shells, however, the potential gradient is strongly decreased, and also has a different sign.
In contrast to that, the potential gradient in the innermost shell is much larger for the quantum dots with an even number of shells, while it is strongly decreased in the case of an odd number of shells.
Since the amplitude of the pyroelectric potential is dominant, the total potential mostly follows the trends of the pyroelectric potential. This means that the potential inside the quantum dot core, where the electronic single-particle wavefunctions are mostly confined, can be very easily switched on and off by changing the number of shells grown on the quantum dot.

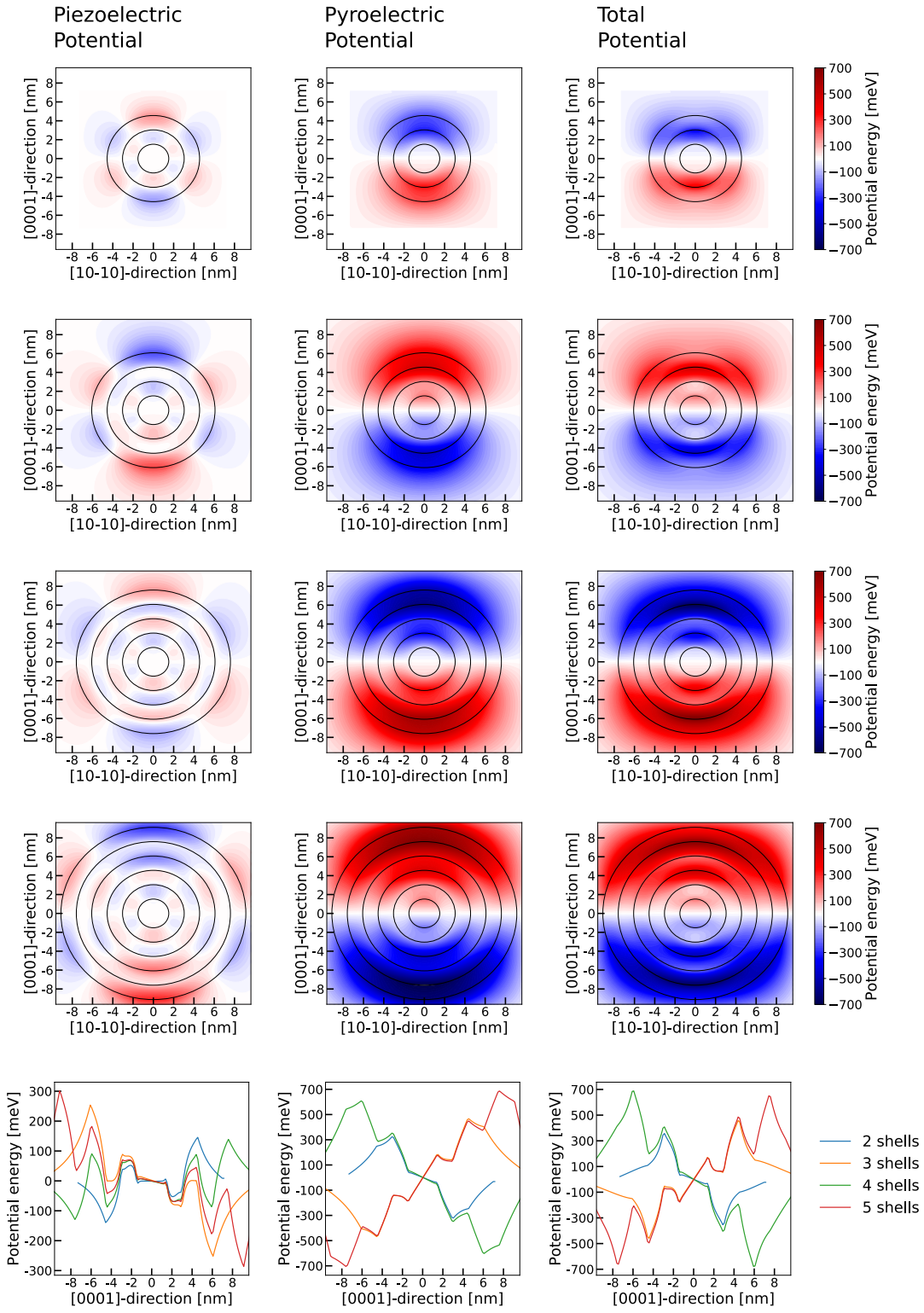

Figure 4.9: 2D contour-plots and line-scans of potential calculations for multi-shell quantum dots from series C with 2, 3, 4 and 5 shells, respectively. All quantum dots have wurtzite lattice structure. The top four rows of plots show 2D contour-plots of the potentials of multi-shell quantum dots with 2, 3, 4 and 5 shells. respectively. The last row depicts line-scans of the same potentials along the c-axis. The left column shows the piezoelectric potentials, the middle column displays the pyroelectric potentials and the right column the total potentials.

4.3.4 Macroscopic Equivalent: IFGARD

Similar to the change in pyroelectric polarisation in the quantum dot core introduced by additional shells, a way of controlling pyroelectric polarisation in an active region of a semiconductor device through additional layers of semiconductor material outside the active region was published in [50] and patented [51].
In this case, quantum wells and epitaxial quantum dots were studied, and it was shown that the pyroelectric polarisation inside the active region could be completely switched off by applying an additional layer of the material of the active region as a blocker layer (called an IFGARD-layer) on both sides of the active region. This is the same effect described above for additional shells on the colloidal quantum dots.
The upper part of figure 4.10 shows calculated band-edges for a single quantum well without (in red) and including the IFGARD-layers. The gradient inside the quantum well in the case without these layers is due to the potential gradient from the pyroelectricity of the material. If the IFGARD-layers are introduced, the gradient inside the quantum well is eliminated completely. This behaviour is similar to the change in potentials inside the quantum dot core introduced by additional shells discussed above.
The fact that, for spherical quantum dots, the pyroelectric potential can not be completely eliminated, but only decreased, is due to the fact that the interfaces between shells increase in size for additional shells, leading to larger charges being introduced into the system with each additional shell, causing the increased potential amplitudes found for the outermost shells.
In contrast to this, the interfaces of the quantum wells remain exactly the same size, leading to the complete elimination of the internal potentials through IFGARD.
An additional patent [52] was filed for the slightly different scenario where the IFGARD-layers are not made from the same material as the active region, but consist of a material composition from a range between the active region material and the matrix material. This allows for precise tuning of the potential gradient inside the quantum dot, instead of eliminating the potentials, allowing for e.g. the compensation of bias-voltage induced gradients in electrically driven devices.
One could imagine a similar application for colloidal multishell quantum dots, where the material of an additional shell would be $CdSe_xS_{1-x}$, with x between 0 and 1. This would presumably also allow for the possibility of tuning the potential gradient inside the quantum dot core. We did, however, not perform any numerical analysis of this scenario.

4.4 Summary

While the strain distributions are similar for wurtzite and zincblende quantum dots, they give rise to strongly different piezoelectric potentials. These piezoelectric potentials reflect the symmetries of the crystal lattices: for zincblende, the alternating minima and maxima along the [111]-directions lead to the interchangeability of the x-, y- and z-axes, while for wurtzite there is a pronounced potential gradient along the crystal c-axis.
In the wurtzite case, the additional pyroelectric part of the electric potentials also possesses a strong gradient along the c-axis, yet with opposite sign. Its larger amplitude leads the gradient of the total potential being aligned with the pyroelectric gradient.

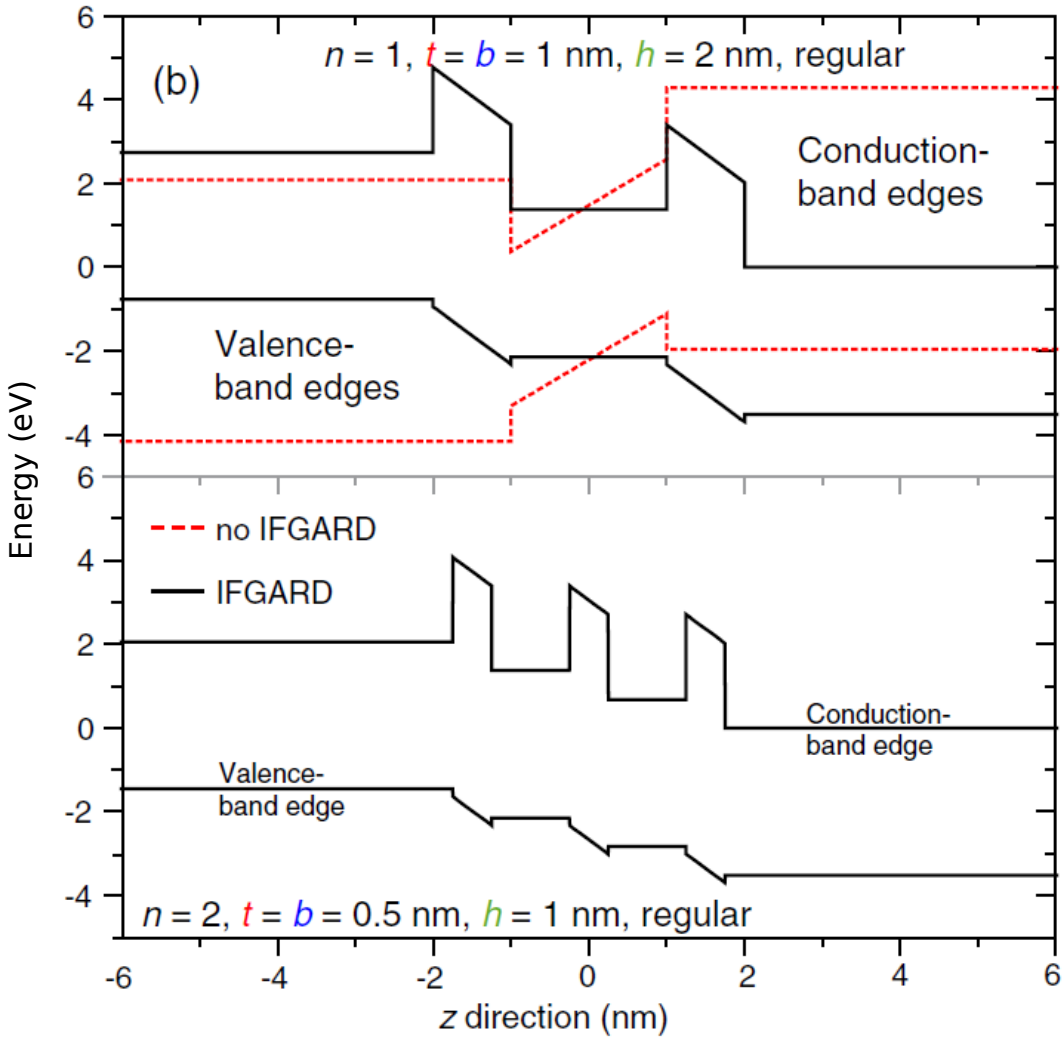

Figure 4.10: From: [50]. Top: Band-diagrams for a single quantum well with and without IFGARD layers. Bottom: Band-diagram for a double quantum well with IFGARD layers. The band-edges inside the quantum wells are constant, when IFGARD-layers are present, indicating the absence of a potential gradient. When there are no IFGARD layers, the band-edge energies have a gradient, resulting from the gradient of the electric potentials inside the quantum dot.

Variations in the dielectric constant of the quantum dot environment were shown to strongly affect the calculated potentials in the quantum dot shell, with the potential inside the core being largely unaffected. However, for thin shells, there still might be non-negligible effects of the environment on the potential inside the quantum dot core.
We also analysed the effects on the potentials of additional quantum dot shells, finding that the polarity of the pyroelectric part of the potential is switched when changing between even and odd numbers of shells. The gradient amplitude inside the quantum dot core is also strongly affected when changing between even and odd numbers of shells. This effect is similar to the concept of IFGARD-layers in epitaxial quantum structures, on which the author was a contributor.

5 Electron and Hole Single Particle Calculations

In this chapter, we present the results of the single-particle calculations for the different quantum dot series. The impact of the internal electric potentials as well as non-sphericity on the electronic structure will be evaluated for both lattice structures.

5.1 Single particle energies and wavefunctions

Figure 5.1 shows the calculated single-particle energies for electrons and holes for quantum dot series A2 with wurtzite lattice structure. Results are shown both for calculations including electric potentials and calculations omitting them.
In figure 5.2, results for series A2 for zincblende lattice structure are shown. Here, only results including electric potentials are displayed, as the difference between the two scenarios is negligible, with the largest deviation in single-particle energies being below 0.4 meV.
In both figures, the energies of the four lowest-energy electron orbitals as well as the six highest-energy hole orbitals are displayed, with each orbital representing two single-particle states, due to spin-degeneracy.
The energy scale has been chosen so that the unstrained valence band maximum of the quantum dot shell is at zero energy.
Wavefunctions are displayed for the four orbitals closest to the band-edge, for both electrons and holes. The wavefunction plots show the values of $|\Psi|^2$ in both a 3D isosurface-plot and a 2D contour-plot along a cut through the quantum dot center.
Analysing the energies first, we see that for all considered quantum dot series, the difference between electron and hole energies decreases for larger core sizes. This is due to the decrease in confinement energy, as the wavefunctions are primarily located in the quantum dot core, which has the lower bandgap compared to the shell.
We make the following key observations concerning differences between the two lattice structures:

- For zincblende, the first and second hole orbitals are energetically degenerate, which is in agreement with prior analytical calculations [13]. Likewise, the third and fourth orbitals, as well as the fifth and sixth orbitals also display energetic degeneracy. We do not observe energetically degenerate hole orbitals for wurtzite quantum dots.

- For both lattice structures, the first electron orbital is energetically well separated from the higher electron orbitals.

- For zincblende quantum dots, the second, third, and fourth electron orbitals all display the same energy, whereas in the wurtzite case, only the second and third orbital display degeneracy, with the fourth orbital being energetically split from them. This separation is more pronounced when electric potentials are included.

When comparing the single-particle energies for wurtzite quantum dots with and without the inclusion of intrinsic electric potentials, we make the following observations:

- For small core sizes, the single-particle energies are similar between the two cases, but diverge strongly with increasing core sizes. When potentials are omitted, energies

do not display strong changes for quantum dots with core radius 3 nm or above. However, including electric potentials changes this completely, leading to a strong shift in energies for quantum dots with larger core sizes.

- The energy-separation between the fourth electron orbital and the second and third electron orbitals is more pronounced when internal potentials are included in the calculations. When the potentials are omitted, the energy separation almost vanishes for large quantum dot cores.

- The energy-separation between the different hole orbitals is not as strongly affected by the internal potentials. Only for large core sizes is the energy difference between the first and sixth hole orbital noticeably smaller when internal potentials are omitted.

When analyzing the wavefunctions, we first note that the hole wavefunctions are more closely confined to the quantum dot core than the electrons wavefunctions, and also that the wavefunctions of the holes are less spatially extended than for electrons, even for quantum dots with rather large cores. This is attributed to the larger effective mass of the holes.
When comparing the wavefunctions for the two lattice structures, we find the following:

- Electron and hole groundstates for both lattice structures exhibit s-type symmetry. The two degenerate groundstate hole orbitals for zincblende structure both exhibit s-type symmetry.

- For wurtzite lattice structure, the second and third electron orbitals as well as the second and third hole orbitals have the form of a torus, oriented in the (0001)-plane. This toroidal shape arises from a hybridisation of p_x- and p_y-type symmetries. The fourth electron and hole orbitals, by contrast, possess p_z type symmetry.

- The wavefunctions for the three energetically degenerate electron orbitals for zincblende lattice structure are all hybridisations of p_x-, p_y-, and p_z-type symmetries. The wavefunction of the second orbital has the shape of a hollow sphere, the wavefunction for the third orbital has a dumbbell shape, oriented along the [111]-direction, and the wavefunction of the fourth orbital has the shape of a torus, oriented in the (111)-plane.

- In zincblende, the wavefunctions of the third and fourth hole orbitals display a symmetry similar to the wavefunctions of the third and fourth electron orbitals.

When examining the effects of the electric potentials on the wavefunctions for the wurtzite quantum dots, we find the following:

- The inclusion of electric potentials leads to a separation of the electron- and hole-wavefunctions along the c-axis. The shape of the wavefunctions does not change significantly, except for the p_z-shaped fourth orbital for both electrons and holes, where the probability density of the center-aligned half of the dumbbell-shape is increasingly diminished.

In figure 5.3, the single-particle energies for series A3 are plotted. In this case, wavefunctions are not shown, as they are very similar to the results shown above.
For the zincblende calculations, we observe the same orbital degeneracies as in series A2 above. We also see a similar energy shift as above, thus decreasing the effective bandgap for larger dots, which, again, is attributed to a decrease in confinement energy as the core increases in size.
In the wurtzite case, we observe the same general trends as in the series above, superimposed by the energy shift due to the inclusion of the electric potentials.
Figure 5.4 shows single-particle energies for one wurtzite quantum dot (geometry A2-6) for different values of the environment permittivity ε_r, ranging from 1 to 100. We did not include results for zincblende lattice structure, as the single-particle energies for zincblende are almost completely unaffected by this parameter, with a maximum deviation for any single-particle energy of below 0.3 meV.
Evidently, increasing the permittivity of the environment increases the effective bandgap, with the electron single-particle energies rising by the same magnitude as the hole single-particle energies decrease. The energy shifts are uniform for all calculated orbitals, except the fourth electron orbital, where the energy upshift is strongly decreased. From figure 5.1, we can see that the wavefunction corresponding to this orbital has p_z-symmetry, and that it is most strongly confined on the upper part of the quantum dot core.
One hypothesis regarding the origin of the decreased energy shift for this orbital is, that the associated wavefunction has the smallest area of high probability density at the core-shell interface, where the change of the electric potentials induced by the variation in environment permittivity is the strongest, as can be seen in figure 4.6.

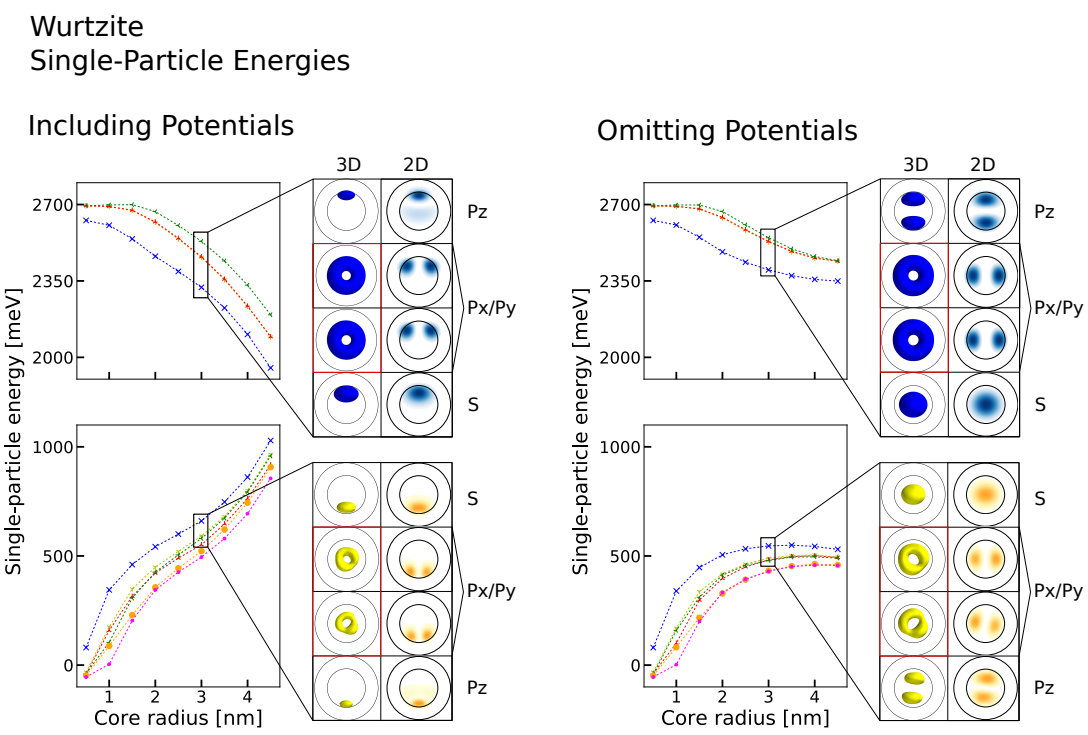

Figure 5.1: Energies and wavefunctions of single particle states for quantum dots of series A2 for wurtzite lattice structure. The left side of the figure depicts results for calculations including internal potentials, while on the right side results of calculations without internal potentials are shown. The upper part of the energy-plot depicts the single-particle electron energies for the four lowest energy electron orbitals, each consisting of two energetically degenerate states. In the lower part of the energy-plot, the energies of the six highest energy hole orbitals are displayed. The top part of the wavefunction visualisation shows the wavefunctions associated to the four lowest energy electron orbitals, plotted in blue, while the bottom part shows the wavefunctions for the four highest energy hole orbitals, plotted in yellow. There are both 3D isosurface and 2D contour-plots of the wavefunctions. All wavefunction plots, except the ones marked by a red border, are shown with a viewing direction parallel to the y-axis, while for the plots marked by a red border the viewing direction is along the z-axis.

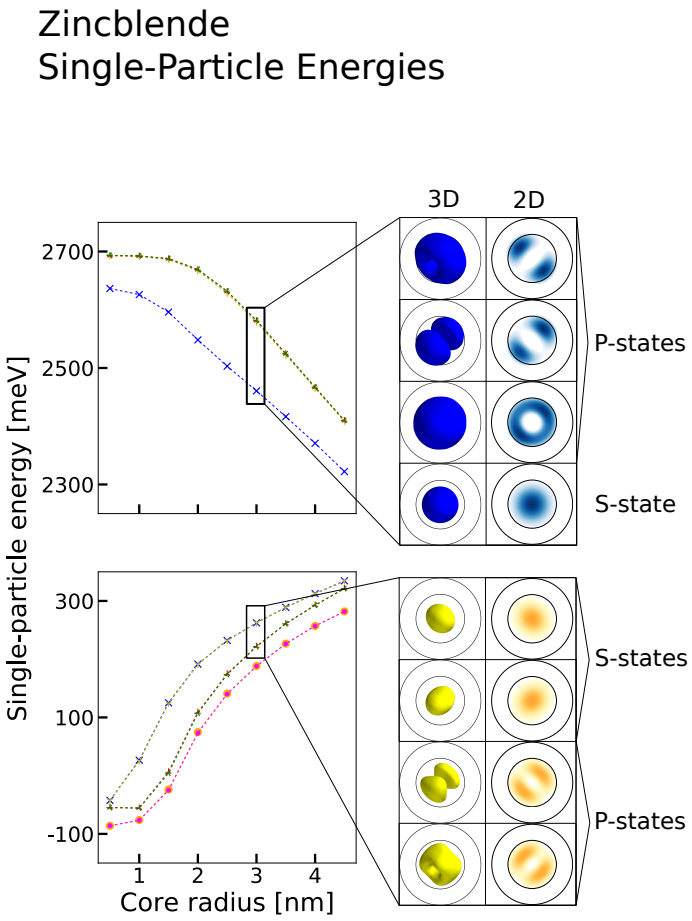

Figure 5.2: Energies and wavefunctions of single particle states for quantum dots of series A2 for zincblende lattice structure. The upper part of the energy-plot depicts the single-particle electron energies for the four lowest energy electron orbitals, each consisting of two energetically degenerate states. In the lower part of the energy-plot, the energies of the six highest energy hole orbitals are displayed. The top part of the wavefunction visualisation shows the wavefunctions associated to the four lowest energy electron orbitals, plotted in blue, while the bottom part shows the wavefunctions for the four highest energy hole orbitals, plotted in yellow. There are both 3D isosurface and 2D contour-plots of the wavefunctions. All wavefunction plots are shown with a viewing direction parallel to the y-axis

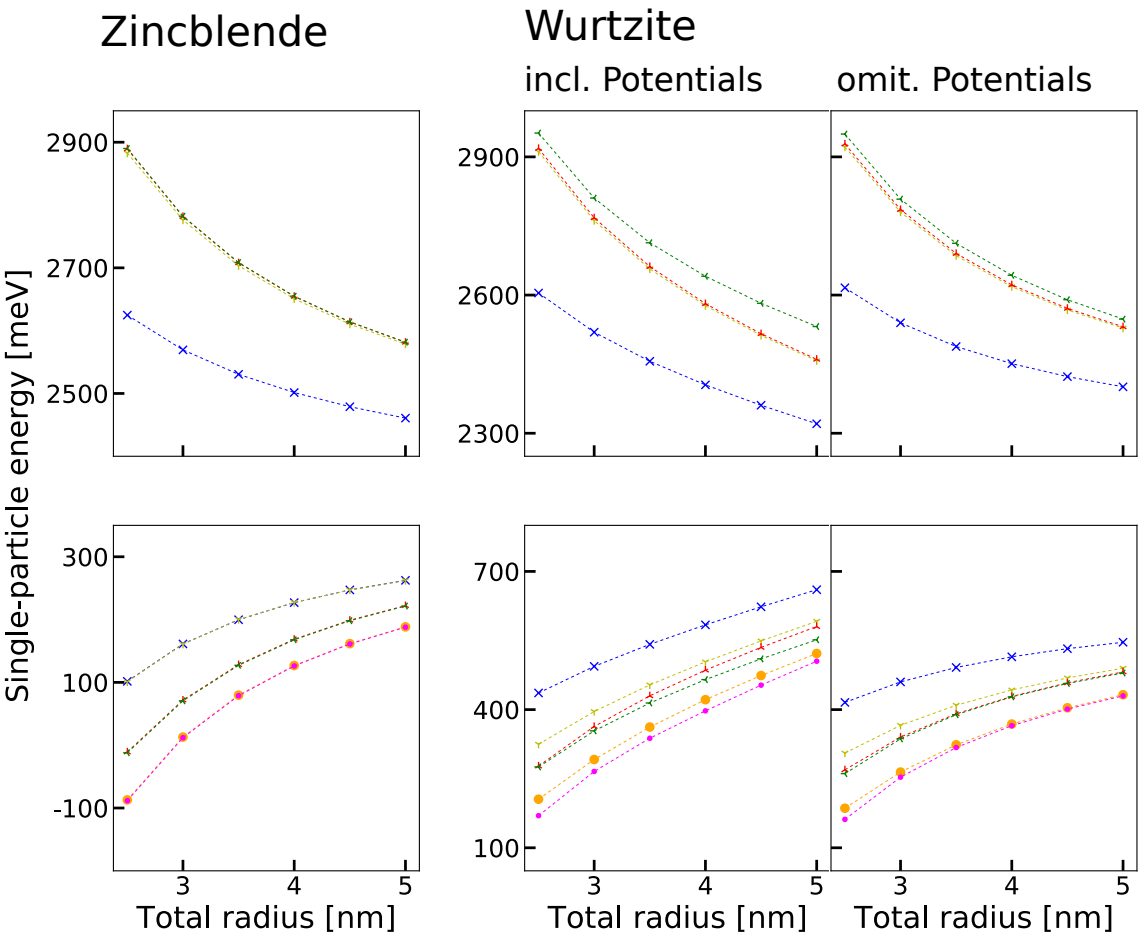

Figure 5.3: Energies of single particle states for quantum dots of series A3 for both crystal structures. Wurtzite results are displayed both including and omitting electric potentials. The upper part of the energy-plot depicts the single-particle electron energies for the four lowest energy electron orbitals, each consisting of two energetically degenerate states. In the lower part of the energy-plot, the energies of the six highest energy hole orbitals are displayed.

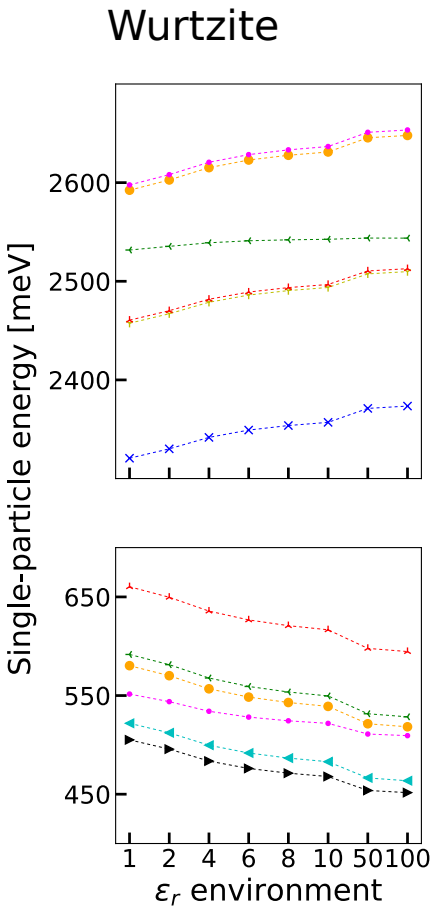

Figure 5.4: Energies of single particle states for varying values of environment permittivity for quantum dot geometry A2-6 in wurtzite lattice structure. The six lowest-energy electron orbitals are plotted in the top part of the plot, while the six highest energy hole orbitals are plotted in the bottom part.

5.1.1 Ellipsoidal quantum dots: degeneracy and symmetry-breaking

After examining single-particle calculation for spherical quantum dots with varying core-sizes, we now present results for ellipsoidal quantum dots of series B1 and B2. The material volumes of the core and the total quantum dots are the same for all quantum dots in the series, with only the aspect ratio of the ellipsoids varying between the quantum dots in these series. This provides us with the opportunity to examine the effects of a reduced spacial symmetry on the single-particle states, while excluding the size effects on both the confinement energy and the potentials, which we analysed in detail in the previous subsection.
Figure 5.5 contains single-particle energies and wavefunctions for wurtzite lattice structure with the aspect-ratio being varied along the [10-10]-direction. The wavefunctions are plotted as 2D contour plots in the xz-plane and the yz-plane, to enable an easier comparison of the different geometries.
Figure 5.7 contains single-particle energies for wurtzite lattice structure with the aspect ratio variation along the [0001]-direction.
In figure 5.6 the corresponding results for zincblende lattice structure are displayed, with the aspect ratio being varied along the [100]-direction. No additional aspect ratio series along a different direction was performed for zincblende lattice structure, because of all three principal lattice directions being equivalent.
When analyzing the results in figure 5.5, we find the following:

- At aspect ratio 1, the results from the spherical dots are replicated, including the energetically degenerate second and third electron orbitals. As we change the aspect-ratio, however, this degeneracy is split, leading to an approximately linear shift in energy along the aspect ratio for both these orbitals, but with different sign.

- The geometry of the associated wavefunctions is also changed, from both orbitals having a torus-shape to one orbital wavefunction being a dumbbell-shape in x-direction and the wavefunction of the other orbital being a dumbbell-shape in y-direction.

- The lowest electron orbital is only lightly affected by the change in aspect ratio, as is the fourth electron orbital.

- Similar to the electrons, the second and third hole orbitals also show a crossing behaviour, as well as the same kind of change in wavefunction geometries.

- In contrast to the electrons, all hole orbital energies show a strong downshift for higher aspect ratios. The amplitude of this downshift is similar for all orbitals, except for the one associated to the p_y-shaped wavefunction.

We can understand the observed energy shifts by looking at the interplay of confinement energy and influences of the electric potential. For the wurtzite lattice structure, we observed a strong potential gradient along the [0001]-direction. This leads to the displacements of the wavefunctions and the change of single-particle energies, lowering the effective bandgap. For aspect ratios below 1, the core is more extended along the [0001]-direction,

leading to a larger area of this strong potential gradient. For aspect ratios above 1, the opposite is true, and the length of the gradient is diminished. This directly leads to the strong shifts in energies observed for the hole orbitals.
The shift is much stronger for holes than for electrons because of the more confined nature of the hole wavefunctions, allowing them to follow the potential gradient to a much stronger extent than the electrons. Additionally, the more the quantum dot geometry deviates from sphericity, we increase the confinement energy imposed on the particles. This effect is more strongly observed for the electrons, as their wavefunctions are much more extended in space.
Due to the design of the ellipsoidal geometries, this effect is more strongly observed for smaller aspect ratios than for larger ones, as the curvature radius at the uppermost point (along the [0001]-direction) of the core-shell interface is smaller for aspect ratios below 1. This is another factor explaining why the shift in electron energies is that much smaller than for holes.
The splitting observed for the second and third orbitals for both particle types can be understood by analysing the confinement energy changes induced by the change in aspect ratio. For aspect ratios above 1, the quantum dot extent is larger in x-direction than y-direction, leading to a lowering of the energy associated to the p_y-shaped wavefunction. For aspect ratios smaller than 1, the opposite is true, leading to the observed splitting behaviour.
If we compare this to the aspect ratio series in z-direction, plotted in figure 5.7, we observe the following differences:

- The second and third orbitals for both electrons and holes no longer display energy-splitting. In the case of electrons, they are degenerate, as is the case in spherical quantum dots. For holes, their energies are almost degenerate, too.
- The energy shift for the holes is more strongly pronounced than before.
- The fourth electron orbital displays a slight downshift for higher aspect ratios, while the other orbitals shift up.

These energy-shifts can again be explained by the interplay of confinement energy and electric potentials: As we elongate our ellipsoidal quantum dot along the [0001]-direction, the area of the potential gradient is increased much more strongly than before, leading to the even stronger shifts displayed for the holes.
The increase in confinement energy, however, is also larger than for the series discussed before, as both curvature radii on the uppermost part of the core-shell interface are smaller than the values for the series discussed above. This leads to a reversal in energy shift for the three lowest energy electron orbitals, as the influence of the confinement energy exceeds the shift induced by the electric potential. The energy shift of the fourth electron orbital is due to the wavefunction being much more spacially confined than the other wavefunctions, and therefore being less affected by the increase in confinement energy.
Since the geometries for this aspect ratio series are identical in x- and y- direction, the energy splitting from the series discussed before is not observed here.
For zincblende lattice structure, we make the following observations from figure 5.6:

- The lowest energy electron orbital is not strongly affected by the change in aspect ratio.

- The second, third and fourth orbitals, however, display a linear change in energy over aspect ratio, as well as a change in the geometry of their associated wavefunctions: One orbital displays a downshift in energy with increasing aspect ratio, with its associated wavefunction having a p_x dumbbell geometry. The other two orbitals remain energetically degenerate and display an energy upshift for increasing aspect ratios, with the associated wavefunctions having the shape of a torus, oriented in the yz-plane.

- The two highest energy hole orbitals, being energetically degenerate for spherical systems, are likewise shifted in opposite directions for changing aspect ratios. The associated wavefunctions continue to exhibit s-type symmetry, but differ slightly from each other, in terms of their spacial extension in the different directions. The wavefunction associated to the orbital energies displayed in yellow, is more extended in x-direction, visible for aspect ratios greater than 1, while the other wavefunction displays greater spacial extension in the yz-plane, visible for aspect ratios below 1.

- The third and fourth hole orbitals also display an energy upshift for aspect ratios differing from one, and their degeneracy is broken as well. It is notable, that the wavefunction geometries are similar between the two orbitals, yet differ strongly for aspect ratios below and above 1.

Since the zincblende lattice does not give rise to the strong polarising potential seen in the wurtzite case, these results can be understood by only assessing the impact of the confinement.
As the wavefunction for the lowest energy electron orbital is located in the center of the quantum dot, the confinement effects of changing the shape of the quantum dot core do not greatly affect the orbital energy. The three next highest orbitals, however, are made up by wavefunctions that are hybridisations of all three p-state orientations, which is due to the perfect symmetry of the spherical confinement. As we change the aspect ratio, we break this confinement symmetry, to the effect that, in the case of aspect ratios above one, the confinement is weaker in x-direction, and stronger in the yz-plane. As a result, the wavefunction hybridisation is broken, with one wavefunction now having the shape of a dumbbell in x-direction, and corresponding lower confinement energy for larger aspect ratios, while the wavefunctions corresponding to the other two orbitals having the shape of a torus in the yz-plane, with lower confinement energies for lower aspect ratios. This is very similar to the results found for spherical wurtzite quantum dots, where the spherical symmetry is broken by the internal potentials, rather than the quantum dot shape.
The wavefunctions associated with the hole orbitals undergo a similar transformation, with the geometry changes in the associated wavefunctions being less pronounced than for the electrons.
In conclusion, we make the following observations for ellipsoidal quantum dot geometries:

1. Deviations from the spherical geometry lift the energetic degeneracies observed for the perfect spherical case discussed above.

2. By elongating the quantum dots in one direction, a preferred axis is created, thus splitting the threefold electron p-state degeneracy in zincblende into a separate level and a twofold degeneracy. In wurtzite, the potentials already delineate one preferred axis, the observed twofold p-state degeneracy can then be further split by introducing the geometric preferred direction along another axis. If we elongate the quantum dot along the c-axis, the twofold degeneracy of the p-states is retained.

3. The shape of the calculated wavefunctions is strongly impacted by deviations from spherical symmetry, eliminating the hybridisation observed for the wavefunctions associated to degenerate energy orbitals.

4. Non-sphericity can induce large shifts in single-particle energies and the effective bandgap, even while keeping the total quantum dot volume constant. This is observed particularly for wurtzite lattice structure, owing to the strong gradients observed in the pyroelectric potential.

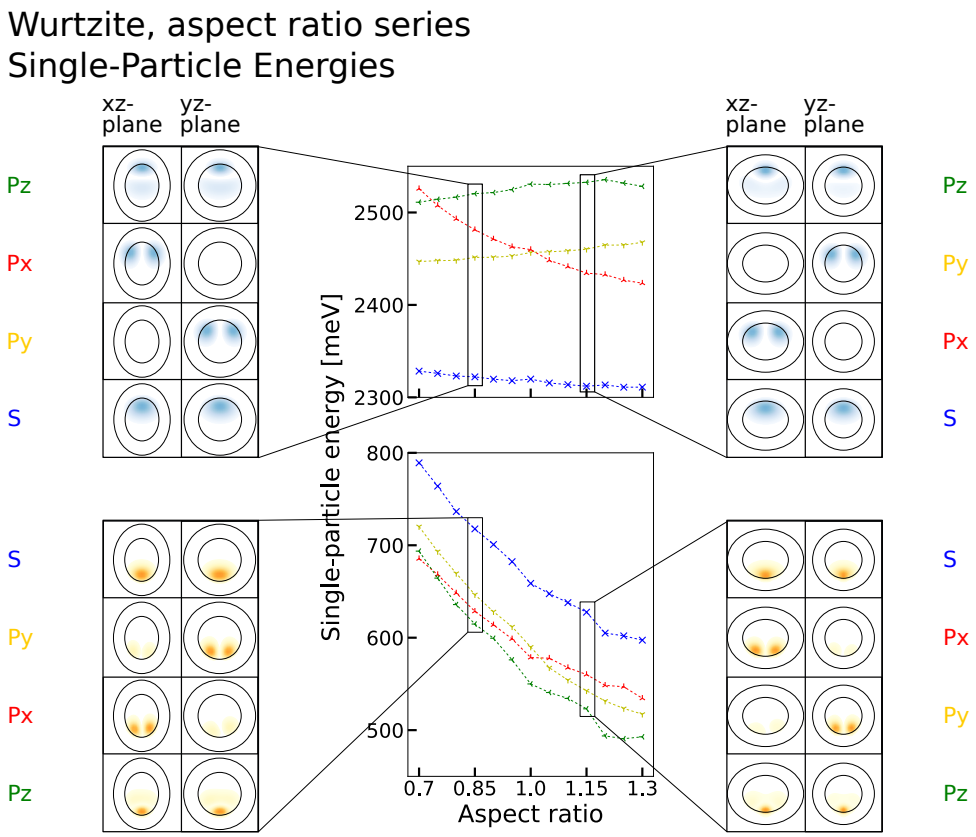

Figure 5.5: Energies and wavefunctions of single particle states for an aspect ratio series of ellipsoids (series B1) with wurtzite lattice structure. The energies of the four lowest energy electron orbitals are depicted in the upper part of the energy plot, while the energies of the four highest energy hole orbitals are depicted in the lower part. Wavefunctions for each orbital are plotted for aspect ratios of 0.85 on the left side, and aspect ratio 1.15 on the right side. Electrons are plotted in blue, while holes are plotted in yellow. All wavefunctions are shown as 2D contour-plots in the xz-plane and the yz-plane. The quantum dot shape is indicated by black ellipses.

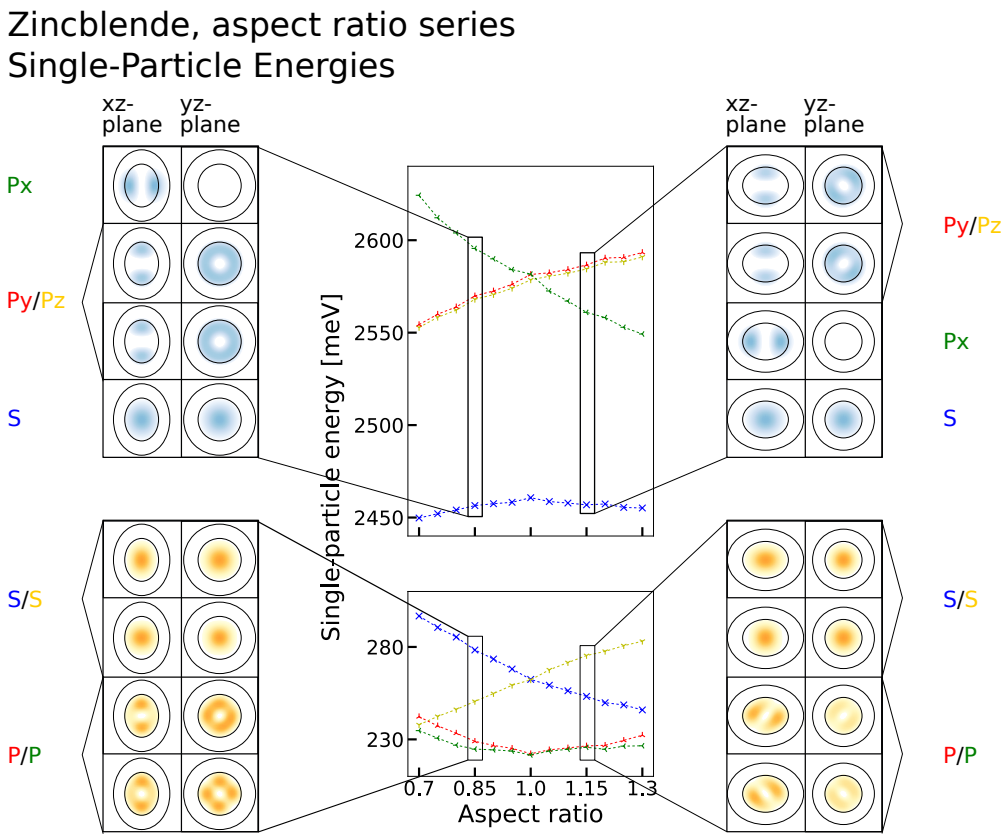

Figure 5.6: Energies and wavefunctions of single particle states for an aspect ratio series of ellipsoids (series B1) with zincblende lattice structure. The energies of the four lowest energy electron orbitals are depicted in the upper part of the energy plot, while the energies of the four highest energy hole orbitals are depicted in the lower part. Wavefunctions for each orbital are plotted for aspect ratios of 0.85 on the left side, and aspect ratio 1.15 on the right side. Electrons are plotted in blue, while holes are plotted in yellow. All wavefunctions are shown as 2D contour-plots in the xz-plane and the yz-plane. The quantum dot shape is indicated by black ellipses.

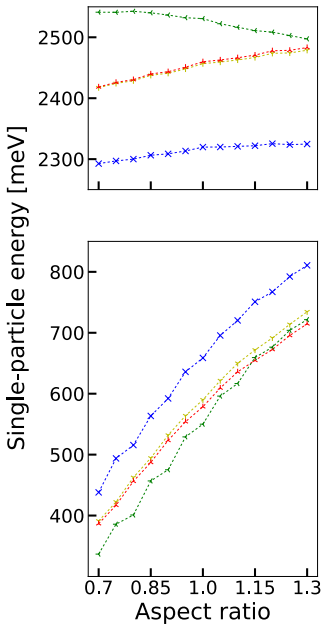

Figure 5.7: Energies of single particle states for an aspect ratio series of ellipsoids (series B2) with wurtzite lattice structure. The aspect ratio change is along the lattice c-axis. The energies of the four lowest energy electron orbitals are depicted in the upper part of the energy plot, while the energies of the four highest energy hole orbitals are depicted in the lower part.

5.2 Single-Particle lifetimes

The radiative ground-state lifetimes for the spherical quantum dot series A2 and A3 are shown in figure 5.8. Here, lifetimes are plotted for calculations both including and omitting electric potentials. The lifetimes for the ellipsoidal quantum dot series B1, B2, B3 and B4 are given in figure 5.9. Results for zincblende and wurtzite lattice structures are plotted together here, to allow for easier comparisons.
Analysing the results for spherical quantum dots, we note the following points:

- For zincblende structure, the lifetimes are not affected by the inclusion of electric potentials. This is in good agreement with the fact, that the single-particle energies and wavefunctions are also hardly affected by these potentials.

- For wurtzite, however, we see a drastic increase in lifetimes for larger core-sizes, or larger total quantum dot size when including the electric potentials, while mirroring the zincblende behaviour when omitting them.

- The wurtzite lifetimes in absence of intrinsic potentials are about twice as large as in the case of zincblende. This originates from the fact that the zincblende hole ground state is energetically fourfold degenerate, and thus the number of radiative paths is doubled compared to wurtzite.

- Lifetimes for wurtzite quantum dots with internal potentials included grow exponentially with increasing core sizes or quantum dot sizes. This is attributable to

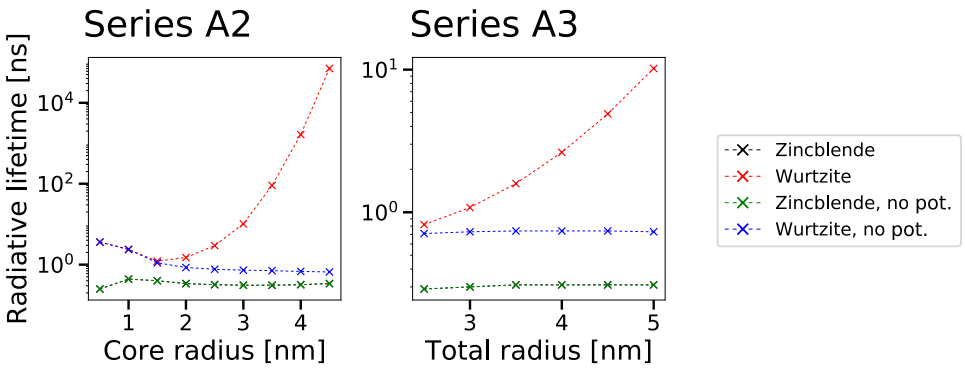

Figure 5.8: Radiative lifetimes for spherical quantum dots with different core-sizes for both lattice structures. Results including and omitting electric potentials are displayed.

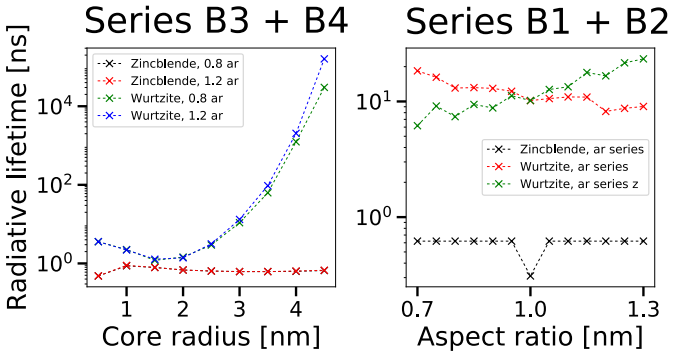

Figure 5.9: Radiative lifetimes for ellipsoidal quantum dots with different aspect ratios for both lattice structures.

the growing degree of wavefunction separation, leading to decreasing electron-hole wavefunction overlap.

The results for ellipsoidal quantum dots can be summarised as follows:

- The lifetimes for the core size series with fixed aspect ratio very closely mirror the spherical core size series.
- The zincblende aspect ratio series does not show any dependance of the lifetime on aspect ratios, except for aspect ratio 1, where it is exactly half of the value for all other aspect ratio. This is due to the hole ground state orbital degeneracy being lifted for non-spherical quantum dots, leading to the number of radiative paths being halved.
- The two different wurtzite aspect ratio series both display a dependance of lifetimes on aspect ratio. This is due to the extent of the core in [0001]-direction being slightly diminished for larger aspect ratios, when extending along the x-direction, decreasing wavefunction separation, while for the aspect ratio being changed along the z-direction, the wavefunction separation is increased for higher aspect ratio, leading to an increase in lifetime.

5.3 Summary

To summarise the results from the single-particle calculations:

1. The electric potentials strongly influence the energies and wavefunctions for wurtzite quantum dots, while the zincblende results are largely unaffected.

2. The combination of energy shifts towards a decreased effective bandgap, a wavefunction separation of electrons and holes, and strongly increased radiative lifetimes is also found in other wurtzite nanostructures, and is usually called the Quantum Confined Stark Effect.

3. Deviations from spherical geometries have impacts on the single particle energies and wavefunctions, these impacts are again much stronger for the wurtzite lattice structure.

6 Coulomb-Interaction: Excitonic Properties

In this chapter we will present the results of the Multi-Particle Hartree-Fock Calculations outlined in chapter 2.5. In chapter 3, we presented the exciton-structure obtained by Efros *et al* for spherical quantum dots. We will compare these results to our own findings, focusing on the impact of the intrinsic electric potentials.
We have calculated eight different exciton states for every quantum dot geometry, four of which arise from the single-particle electron and hole ground-states and form the excitonic ground states of the quantum dots. The other four excitons arise from the single-particle electron ground state and the first excited hole state, and make up the first excited excitonic states.
First we will introduce the nomenclature used for describing the different excitons calculated: we identify each exciton by the spins of the electron and the hole, as well as a number, indicating if it belongs to the ground states or the excited states. So the exciton with both electron and hole spin up and belonging to the excitonic ground states would be designated as $X_1 \uparrow\Uparrow$ with the electron spin indicated by the single-line arrow, and the hole spin given by the double-lined arrow. The index 1 indicates it being an exciton ground state. The exciton with identical spin-configuration, but belonging to the excited exciton states is designated as $X_2 \uparrow\Uparrow$.
We will begin by presenting the exciton energies and energy-splittings for different quantum dot series. After that we will analyse the projections of the calculated hole-states of the excitons on the different valence bands as well as their spin projections, which will provide us with some insight regarding the experimentally observed luminescence from the spin-forbidden states.
Finally, the exciton lifetimes will be discussed and compared to previous investigations.

6.1 Exciton Energies

The exciton energy structure is very similar for all series investigated here. The X_1 and X_2 excitons have very similar total energies, respectively. Yet there is an energy splitting within the two groups of excitons between the excitons with parallel electron and hole spins and the excitons with antiparallel spins.
The two excitons within the same group with parallel spins are energetically degenerate, as are the two excitons with antiprallel spins.
Therefore, exciton energy plots are structured in the following way. In part (a), the total energy of the excitons is displayed. In part (b), the energy difference between the X_1 excitons and the X_2 excitons is given. In part (c), we display the energy splitting of the X_1-excitons and in part (d), the splitting of the X_2-excitons is plotted.
Exciton energies for wurtzite quantum dots from series A2 are displayed in figure 6.1, while the results for the same quantum dots, but without inclusion of the internal potentials in the calculations, are given in figure 6.2.
When we compare the total exciton energies for these two cases, we can clearly see, as we did before for the single-particle results, that the internal potentials are lowering the exciton energies for increasing core sizes, an effect that is not observable if these potentials

are omitted in the calculation process.
Even if the internal potentials are omitted, however, the energies are still decreasing towards larger quantum dot cores, which can be attributed to a decrease in quantum confinement, and was also observed in the single-particle picture.
The energy difference between the X_1 and X_2 excitons is very similar for both scenarios, showing a decrease towards larger core-sizes, which can also be attributed to the decrease in quantum confinement.
The energy splitting results between excitons with parallel and antiparallel spin give us the following information:

- Excitons with parallel electron and hole spins have a lower total energy than excitons with antiparallel spins for all quantum dots.
- The energy splitting for the X_2 excitons is almost exactly half that of the X_1 excitons. An explanation for this can be found in the different shape of the hole wavefunction for the X_2 excitons, to be discussed in detail later, leading to a smaller electron-hole overlap.
- The energy splitting decreases for larger core-sizes for both exciton groups and independently of the inclusion of internal potentials in the calculations. This, too, is caused by decreasing electron hole wavefunction overlap, induced by the decreasing quantum confinement.
- The energy splitting for both exciton groups is very similar between the two calculations for small core sizes, but diverges for increasing core sizes: When internal potentials are included, the energy splitting decreases toward zero, while there remains a splitting energy of close to 1meV for the X_1 excitons and 0.5meV for the X_2 excitons, respectively, when internal potentials are omitted. This is due to the wavefunction separation caused by the pyroelectric potentials, which decreases the wavefunction overlap, an effect that is not observed when internal potentials are omitted.

One interesting consequence of the internal potentials, then, is that the wavefunction separation leads to fourfold degenerate exciton levels for quantum dots with core sizes of 4 nm and above. Additionally, we observe the same effects already detailed for the single-particle results, namely wavefunction separation and energy decrease, summarily described as the quantum confined Stark effect (QCSE).
To compare these results to smaller quantum dots, the exciton energies of series A1 are shown in figure 6.3. The total energies for quantum dots with the same core sizes are closely resembling the ones for the larger dots, indicating that the shell thickness does not have a strong influence on exciton energy. The separation between the X_1 and X_2 excitons is also closely reproduced for the small quantum dots.
The energy splitting due to exchange energy follows the same trend as with the larger quantum dots, decreasing for increasing quantum dot size, but is increased in amplitude for quantum dots with the same core size, by a factor of 1.5 .

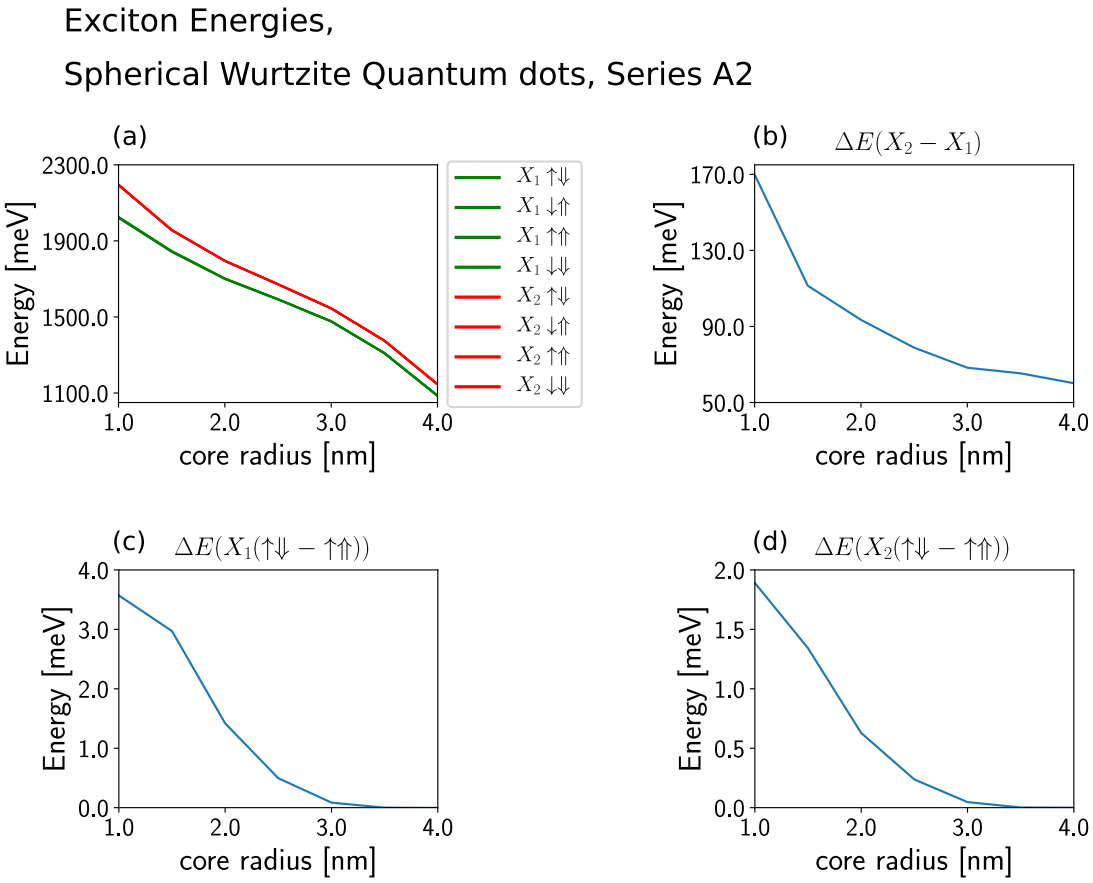

Figure 6.1: Exciton energies for spherical wurtzite quantum dots of series A2. (a) Total exciton energies for all calculated exciton states. (b) Energy difference between the X_1 and X_2 excitons. (c) Energy splitting between X_1 excitons with parallel and antiparallel electron and hole spin. (d) Energy splitting between X_2 excitons with parallel and antiparallel electron and hole spin.

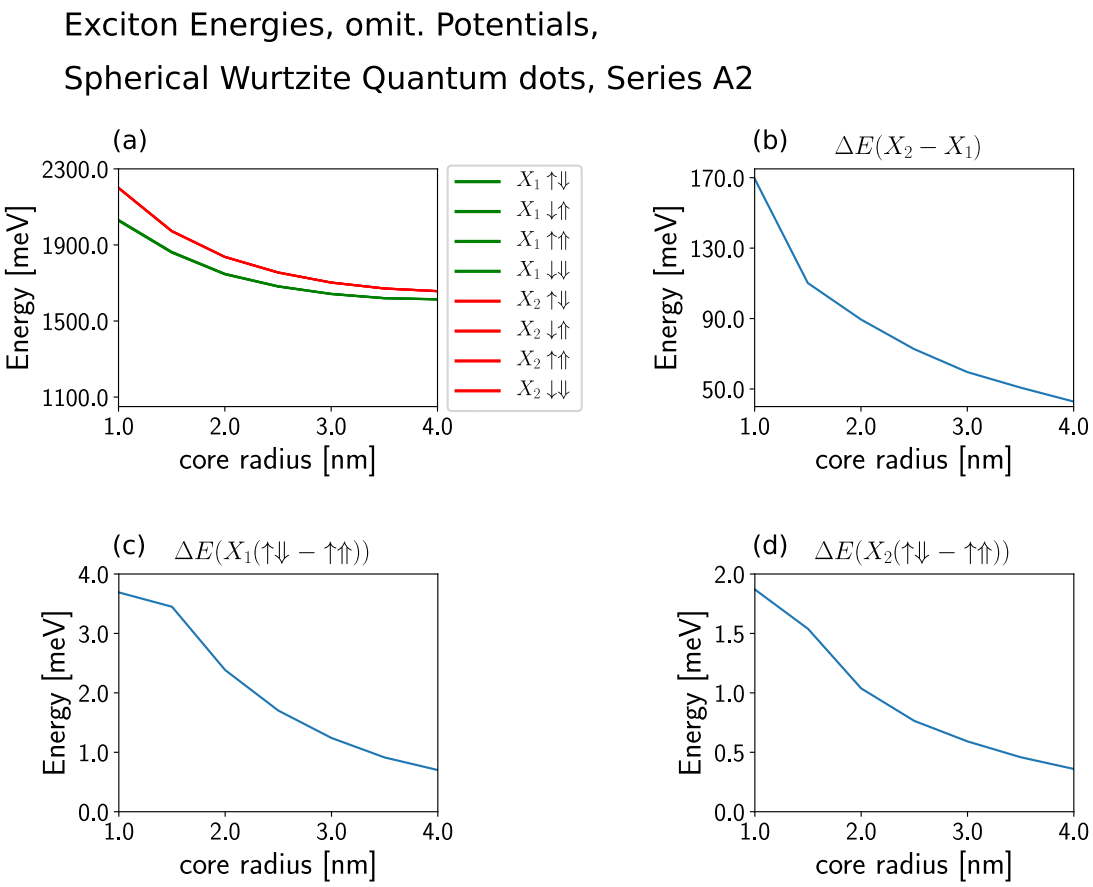

Figure 6.2: Exciton energies for spherical wurtzite quantum dots of series A2. Internal potentials are omitted. (a) Total exciton energies for all calculated exciton states. (b) Energy difference between the X_1 and X_2 excitons. (c) Energy splitting between X_1 excitons with parallel and antiparallel electron and hole spin. (d) Energy splitting between X_2 excitons with parallel and antiparallel electron and hole spin.

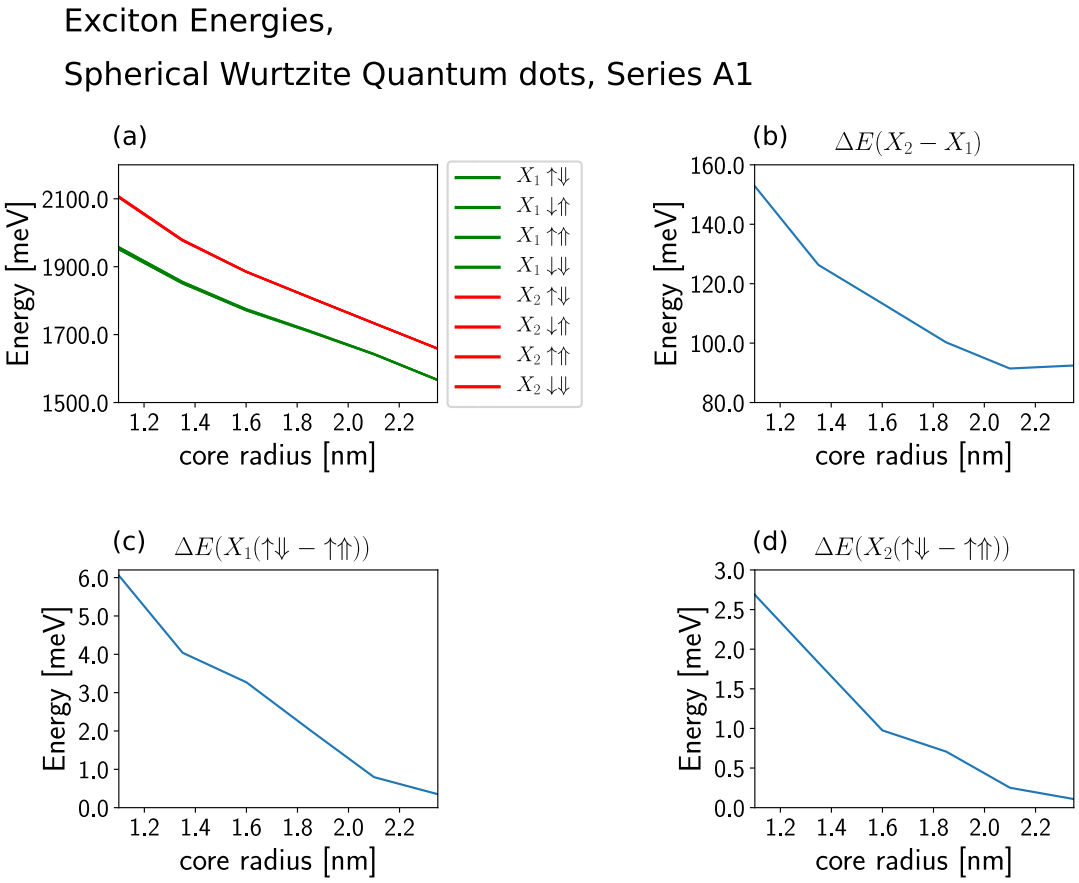

Figure 6.3: Exciton energies for spherical wurtzite quantum dots of series A1. (a) Total exciton energies for all calculated exciton states. (b) Energy difference between the X_1 and X_2 excitons. (c) Energy splitting between X_1 excitons with parallel and antiparallel electron and hole spin. (d) Energy splitting between X_2 excitons with parallel and antiparallel electron and hole spin.

6.2 Valence-band and spin projections

Before we turn our attention to the radiative lifetimes associated to the different excitons, we will examine the projections of the calculated hole-wavefunctions onto the different valence-bands and determine their spin-projection. We do not further study the projections of the electron wavefunctions, because they almost completely consist of the contributions of the conduction band, as would be expected.
Since our implementation of the $\mathbf{k}\cdot\mathbf{p}$ method utilises a basis of Bloch-functions containing $|x\rangle$, $|y\rangle$ and $|z\rangle$ for the valence bands, we first have to utilise the transformations outlined in chapter 2.4.3 to obtain a representation of wavefunctions in the Bloch-basis corresponding to the true valence-band structure.
To then obtain the distribution of the wavefunctions among the different valence bands (and the conduction band associated to $|s\rangle$), we integrate their amplitude corresponding to each band, and divide by the overall amplitude over all subbands.
The results of these calculations are displayed in figure 6.4. We make the following observations:

- The four X_1 excitons have identical values of band projections for all four bands. The same is true for all four X_2 excitons.
- All exciton hole-wavefunctions have only minute contributions of the conduction band (below 0.03 for all quantum dots), as is expected of hole-states.
- The largest share for all excitons in all quantum dots is the contribution of the A-band, with the lower-energy X_1-excitons exhibiting an even larger share of A-band contribution than the higher energy X_2-excitons. This share increases further with increasing core-sizes for all excitons.
- For the X_1 excitons, the contribution of the B-band is slightly higher than that of the C-band, and both are slightly decreasing towards larger cores. For X_2 excitons, the contribution of the C-band exceeds that of the B-band for small cores, but decreases stronger, leading to an equal share for both bands at large core-sizes.

We conclude, therefore, that all calculated excitons are A-excitons, but with contributions from both the B- and C-bands (and very small contributions of the conduction band).
We will now examine the spin projections of the same exciton hole-wavefunctions. Because the single-particle $\mathbf{k}\cdot\mathbf{p}$ theory does not employ a spin-dependant Hamiltonian, the spin distribution is arbitrary between the two wavefunctions making up the energy-degenerate orbitals. Wavefunctions obtained via the Hartree-Fock method, however, are expected to be completely spin-polarised, because spin-dependent exchange-interaction effects are now being taken into account.
When examining the basis transformations described in chapter 2.4.3, we notice that the contributions of the $|z\rangle$ Bloch function are included with opposite spin than the contributions of the $|x\rangle$ and $|y\rangle$ Bloch functions. Therefore, a wavefunction that is completely spin-polarised in the original basis, would be less than completely spin-polarised in the valence-band basis, if it has a contributions from the $|z\rangle$ Bloch state.

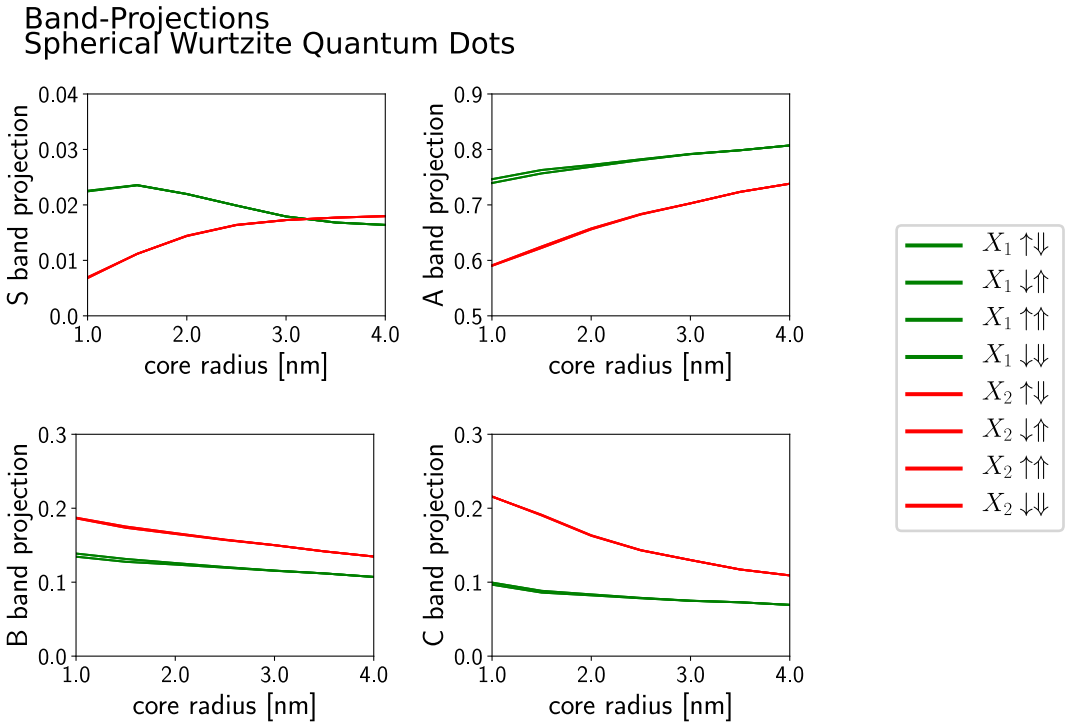

Figure 6.4: Exciton band projections for spherical wurtzite quantum dots of series A2. The contributions of the four bands S, A, B and C are plotted for all calculated excitons in four separate plots.

In figure 6.5, we have plotted the spin projections of the exciton hole-wavefunctions for both Bloch-bases for wurtzite quantum dots from series A2. Excitons with hole spin up are marked by a dashed line, while excitons with hole spin down are marked by a solid line.

We can see that in the original Bloch basis, the spin polarisation is not complete, varying between 0.8 and 0.87. After applying the basis-transformation, however, the spin polarisation is above 0.97 for all excitons. We conclude, therefore, that the hole-wavefunctions of the Hartree-Fock excitons converge in the spin-polarisations attributed to the real valence-band structure, not in the Bloch-basis implemented for the $\mathbf{k}\cdot\mathbf{p}$ Hamiltonian. We can further deduce, that since there is a difference in spin polarisation between the two bases, there are contributions from the $|z\rangle$ spin-up band for the excitons with spin down holes, and contributions from the $|z\rangle$ spin-up band for the excitons with spin-down holes found in every considered exciton. This has consequences for the calculation of the radiative lifetimes, which we will explore in the next chapter.

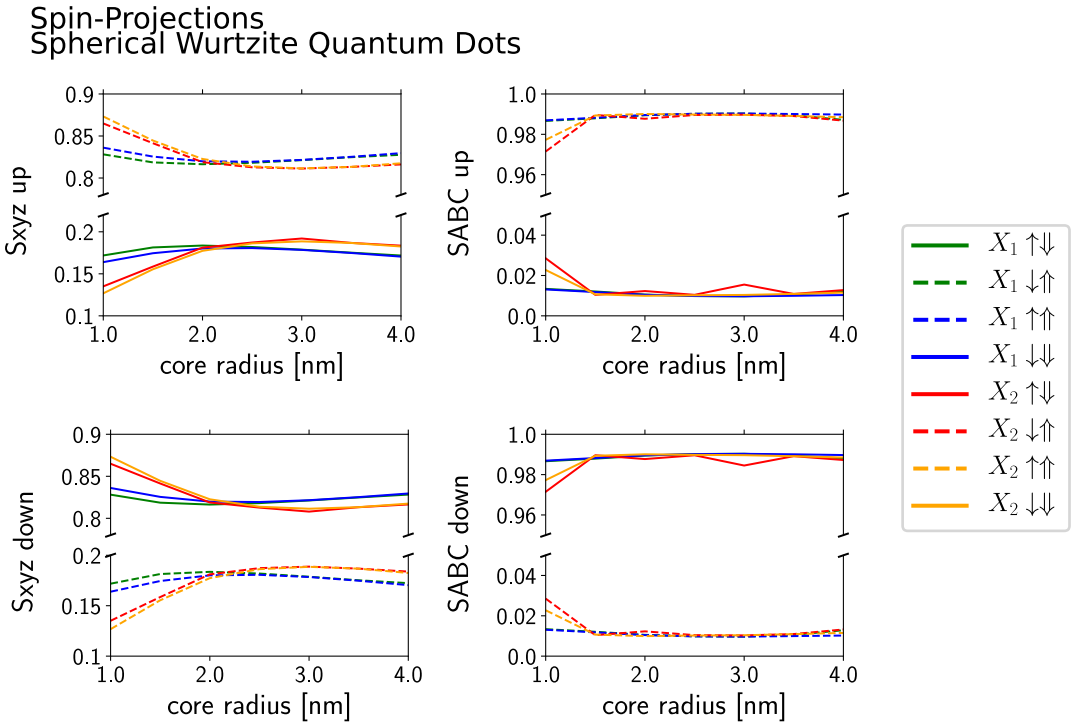

Figure 6.5: Exciton hole-wavefunction spin projections for spherical wurtzite quantum dots of series A2. Projections on the spin up direction are displayed in the top row, while projections on the spin down direction are displayed on the bottom row. In the left column, spin projections performed in the Sxyz-basis are displayed, while the right column shows projections performed in the SABC-basis. Results for excitons with upward hole spin are plotted using dashed lines, while the results for excitons with downward spin are plotted using solid lines.

6.3 Exciton lifetimes

The radiative lifetimes of the calculated excitons are displayed in figures 6.6 and 6.7 for the quantum dots from series A2 with and without included internal potentials, and in figure 6.8 for quantum dots from series A1 with included internal potentials.

For all quantum dot series, the lowest lifetimes are found for the X_1 excitons with antiparallel spin, with the lifetimes associated to the X_1 excitons with parallel spins are increased by a factor of 4 to 5. The lifetimes of the X_2 excitons are strongly enhanced, compared to the X_1 excitons.

This is in sharp contrast to the behaviour found in epitaxial quantum dots, where the lowest energy excitons are typically split up into bright states, with antiparallel spins , and dark states, with parallel spins, with the lifetimes for the dark states being several orders of magnitude larger than the bright states. The analytic calculations by Efros [13] predict a dark state with infinite lifetime as the exciton ground state, as discussed in chapter 3.

The decreased lifetimes, or increased radiative rates, calculated for the excitons with parallel spin, which represent the lowest energy excitonic states, is due to the contributions in the wavefunctions of the bands associated to the $|z\rangle$ Bloch-function, which has opposite spin compared to the $|s\rangle$, $|x\rangle$ and $|y\rangle$ Bloch states, as was shown in the previous chapter. Fermi's golden rule, which is employed for the radiative rate calculation, is independent

of our choice of basis vectors, therefore we calculate the radiative rates in the basis implemented for the **k·p** Hamiltonian. The $|z\rangle$-band contribution therefore leads to a share of inverted hole spin, leading to a finite radiative rate for these otherwise spin-forbidden recombinations.

If we compare the trend of the lifetimes for increasing core sizes in figures 6.6 and 6.7, we notice that the incorporation of internal potentials leads to strongly increasing lifetimes for all excitonic state when the core-size is increased. This is due to the separation of electron- and hole-wavefunctions leading to reduced wavefunction overlap. If the internal potentials are omitted, the lifetimes remain constant for core sizes of 2nm and larger for the X_1 excitons, while the lifetimes for the X_2 excitons display a slight increase, which is much smaller than the increase observed for the calculations incorporating internal potentials. We attribute this to the overlap being decreased for decreased confinement in the quantum dot core, because of the shape of the X_2 hole-wavefunctions.

The lifetimes for series A1 also show an increase for larger core-sizes for the X_1 excitons. This effect is not as noticeable here, due to the smaller core-sizes not allowing for strong wavefunction separation.

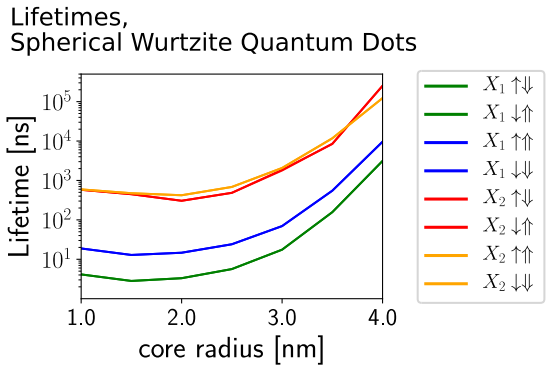

Figure 6.6: Exciton lifetimes for spherical wurtzite quantum dots of series A2. Results are displayed on a logarithmic scale.

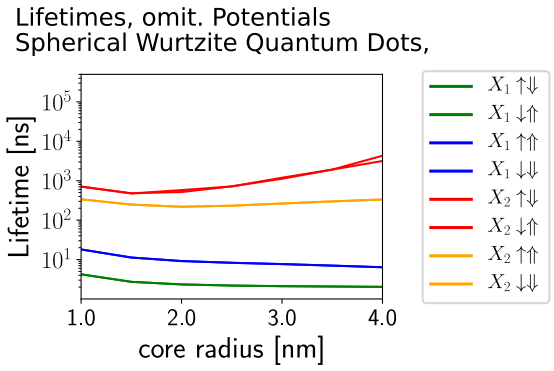

Figure 6.7: Exciton lifetimes for spherical wurtzite quantum dots of series A2. Internal potentials have been omitted in this calculation. Results are displayed on a logarithmic scale.

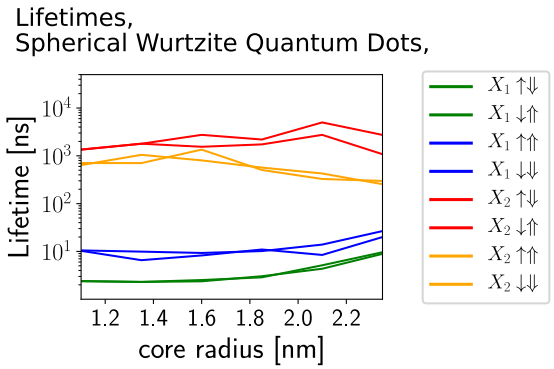

Figure 6.8: Exciton lifetimes for spherical wurtzite quantum dots of series A1. Results are displayed on a logarithmic scale.

6.4 Exciton wavefunctions

Figure 6.9 depicts the excitonic electron- and hole-wavefunctions for quantum dot geometry A2-6 with and without included internal potentials.
We first note that the shape of the wavefunctions for the $X_1 \uparrow\Uparrow$ and $X_1 \uparrow\Downarrow$ excitons are identical, as they differ only in their spin-polarisations. Both their electron- and hole-wavefunctions display s-type symmetry.
The electron wavefunction of the $X_2 \uparrow\Downarrow$ strongly resembles the ones of the X_1 excitons, while the hole wavefunction has the shape of a torus in the xy-plane and therefore exhibits p-type symmetry.
The shapes of the wavefunctions are closely resembling the ones seen in the single-particle picture, depicted in figure 5.1.
If we analyze the influence of the internal potentials, we notice, as we did for the single-particle states, the separation of the electron- and hole-wavefunctions along the c-axis, while their symmetries are retained.

6.5 Summary

We have performed an analysis of the wavefunctions, energies, and lifetimes of eight different Hartree-Fock excitons.
The symmetries of the wavefunctions and the separation of electron and hole induced by the internal potentials for wurtzite lattice quantum dots closely resemble the results obtained in the single-particle picture in chapter 5. We also reproduce the impact of the internal potentials of decreased exciton energies and increased lifetimes for increasing quantum dot core size, summarised as the quantum confined Stark effect (QCSE).
Yet the Hartree-Fock method gives us additional insight in the exciton fine structure and the lifetimes of the different excitons. We discover, that in contrast to the work of Efros, outlined in chapter 3, and results typical for epitactical quantum dots [37], the lowest exciton level is not divided into distinct bright and dark states, where only the bright states exhibit radiative recombination. Instead, while we also find an energy splitting between the excitons with parallel spins and those with antiparallel spins, both these excitons show finite radiative lifetimes, differing by a factor between four and five.
We attribute this unusual behaviour of the nominal "dark state", the exciton with parallel

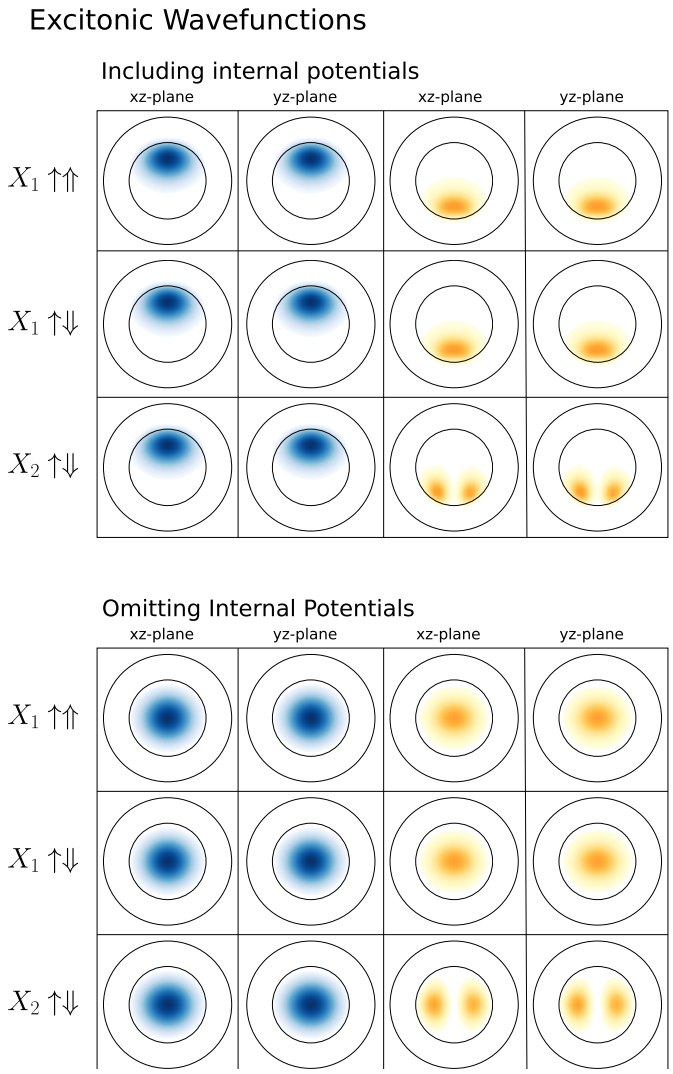

Figure 6.9: Exciton wavefunctions for quantum dot geometry A2-6 with wurtzite lattice structure. The top part shows wavefunctions calculated while including internal potentials in the calculations, while on the bottom part, wavefunctions are displayed that were obtained while omitting these potentials. Electron wavefunctions are depicted in blue, while hole wavefunctions are shown yellow. The quantum dot geometry is indicated by black circles. All wavefunctions are plotted in 2D contourplots in both the xz-plane and the yz-plane.

electron and hole spin, to the contribution of the valence band associated to the $|z\rangle$ Bloch-basis-function, which is projected into the basis of Bloch-functions describing the correct symmetry of the valence bands with opposite spin polarisation than the contributions associated to the other basis states. While this leads to complete spin polarisation in the SABC-basis of the obtained exciton hole wavefunctions, the polarisation is not complete in the Sxyz-basis, leading to a finite lifetime in the optical calculations.

While this is an unexpected result in the framework of the employed Hartree-Fock implementation, it might explain the fact that luminescence from the nominal dark state is consistently observed in measurements [15]. This circumstance has led to several different mechanisms being proposed that explain this dark state luminescence, outlined in more detail in chapter 3.

Our results offer a different explanation of the measured luminescence, since the spin-distribution leads to finite lifetimes even for the exciton with parallel spins.

7 Exciton-Phonon Interaction: Huang Rhys factors

We now present the results of the electron-phonon coupling calculations. As outlined in section 2.7, we obtain a coupling constant, called a Huang-Rhys factor, for every vibrational eigenmode, for each modeled transition of the electronic configuration inside the quantum dot.
We are limited in our analysis to quantum dots with a radius of 2.6 nm, due to strong superlinear scaling of the necessary computation time with system size. Therefore, we restrict our study of Huang-Rhys factors to quantum dots from series A1.
Our analysis will start with the simplest electronic transition: the recombination of the ground-state exciton, where we construct the exciton wavefunction from the ground-state wavefunctions of the single-particle electron and hole calculations. The final electronic state in this case is an empty quantum dot.
Then, we will compare this to the recombinations of excitons where either the electron or hole wavefunction is taken from an excited state, with the final state once again being the empty quantum dot.
Finally, we will examine the recombination of the Hartree-Fock excitons described in section 6 and the changes introduced by the Coulomb interactions, when compared to the results based on single-particle calculations.
In the last part, the transitions between different Hartree-Fock excitons are studied, which may allow us to determine if these transitions might be phonon-assisted.
All calculations are performed for 10 different sets of atomistic phonon calculations, because the atomistic representation of a quantum dot is not unique to the geometry as specified only be core radius and total radius. This is explained in more detail in appendix A.

7.1 Ground-state transition

Figure 7.1 shows calculated Huang-Rhys spectra for three exemplary quantum dot geometries. Results are shown for both zincblende and wurtzite lattice structure, with the wurtzite results shown both for including and omitting the internal potentials. We do not present zincblende results without internal potentials, as they are almost identical to the results including potentials.
The following characteristics of the calculated Huang-Rhys factors stand out:

- Only a small percentage of vibrational eigenmodes display substantial coupling to the electronic transition. There are more than 7000 eigenmodes for every quantum dot, yet more than 90 % of them display no notable coupling strength.
- Only eigenmodes in specific frequency regions display sizeable Huang-Rhys factors, leading to distinct peaks in the Huang-Rhys spectra.
- Coupling strengths are larger for wurtzite structure when compared to zincblende, and larger when including internal potentials than when omitting them. Also, there is a much larger number of eigenmodes displaying notable coupling strength in the case of wurtzite lattice structure.

- For both zincblende and wurtzite with included internal potentials, the overall magnitude of the couplings remains similar for all three exemplary geometries, while for the case of wurtzite without internal potentials, there is a sizeable decrease in overall coupling strength towards larger core-sizes.

To further analyse the calculated Huang-Rhys factors and examine trends and changes along the series of geometries, we separate the energy axis into four distinct regions, to analyse the behaviour of the four different peaks we observe in the spectra.
These regions are:

1. 0 - 70 cm^{-1}: In this frequency region, there is a distinct peak in all calculated Huang-Rhys spectra. In bulk semiconductors, acoustic phonons would be associated to frequencies in this range, which is why we refer to it as the acoustic region.

2. 70 - 160 cm^{-1}: Eigenmodes in this frequency range display the lowest electron-phonon coupling; in some cases, no eigenmode displays any coupling strength, while for some quantum dots, there is a distinct peak, with lower amplitude than the other observable peaks. We refer to this frequency range as the intermediate region.

3. 160 - 250 cm^{-1}: For all quantum dots, there is a peak observable at around 200 cm^{-1}, which is quite close to the optical phonon energies of bulk CdSe. For this reason, we refer to this area as the CdSe region.

4. 250 - 400 cm^{-1}: Similarly, most quantum dots show a peak at around 300 cm^{-1}, or around the energies of the bulk CdS phonons. Therefore, we refer to this energy region as the CdS region.

To analyze the Huang-Rhys peaks in these areas, we calculate the following properties for each area, considering only those eigenmodes, whose Huang-Rhys factors are above a certain threshold:

1. Peak Frequency: To determine the center frequency of the peak, we calculate a weighted average of the eigenmode frequencies in each area, with the Huang-Rhys factors as the weights. Usual methods of determining peak frequencies in, for example, measured photoluminescence spectra, e.g. the fitting of an appropriate function to the data, are not feasible here, since even in the areas of the peaks, the majority of eigenmodes display close to zero coupling.

2. Peak Sum: The peak sum is determined by adding all contributing Huang-Rhys factors in the considered frequency range.

3. Peak Width: To assess the width of the observed peaks, we calculate the standard deviation from the weighted average used for the determination of the center frequency.

Since there are 10 different atomistic calculations performed for every quantum dot geometry, we calculate the above properties for all frequency ranges for all dots, and then average over all 10 atomistic iterations.

Figure 7.2 displays the results of this analysis, with results displayed for both zincblende and wurtzite lattice structure, and with results for calculations with included internal potentials as well as omitted internal potentials.
Analyzing the peak positions first, we make the following observations:

- The peak positions for wurtzite lattice structure do not show strong dependencies on the inclusion of internal potentials. The main deviations observable, in case of excluded internal potentials, are a slight decrease in CdSe peak positions, an increase in intermediate peak positions, as well as a decrease in acoustic peak positions, all only observable for large cores (above 1.85nm).

- The results for zincblende do not show any dependancy on the presence of internal potentials, which is why we excluded the spectra without internal potentials from figure 7.1.

- The positions of the CdSe and CdS peaks for both zincblende and wurtzite structures display similar trends: the CdS peak position decreases, while the CdSe peak position increases with increasing core sizes.

- The CdS peak position is on average 6 wavenumbers higher for zincblende compared to wurtzite, excluding the quantum dot with the largest core radius, where it drops considerably.

- For core sizes of 0.6 nm and below, the CdSe peak position for zincblende is lower than for wurtzite by an average of 5 wavenumbers, while for larger core sizes, there is no difference between the lattice structures in terms of CdSe peak position.

- The position of the intermediate peak is considerably decreased for wurtzite lattice structure. It is worth noting, however, that the peak sums of the intermediate peak for zincblende structures are vanishingly small, making the determination of a center peak frequency very noisy.

- For wurtzite lattice structure, the acoustic peak appears at higher frequencies than for zincblende, excluding the quantum dot with the smallest core size. For both lattice structures, this peak frequency remains rather constant for all core sizes, except for the wurtzite calculations omitting the internal potentials, where the peak position decreases for larger core sizes.

Regarding the peak sums, the following observations can be made:

- The peak sums, in contrast to the center frequencies, display a very strong dependance on the inclusion of internal potentials for wurtzite lattice structure. While for core sizes of 0.85 nm and below the results are quite similar, the omission of internal potentials induces a reduction in peak sums by more than an order of magnitude for quantum dots with larger cores. This reduction affects all four different peaks included in this analysis.

- The calculated Huang-Rhys peak sums are larger for wurtzite lattice structure by an order of magnitude, except when omitting internal potentials, and even then only for quantum dots with large core sizes.

- By contrast, for zincblende the peak sums are unaffected by the omission of internal potentials, as were the center frequencies.

- For zincblende, the sum of the intermediate peak is almost zero, while the sum of the acoustic peak shows a slight decrease from 0.7 at a core size of 0.85 nm to slightly below 0.3 for the largest core size of 2.35 nm.

  The CdS peak sum has a maximum of 2.4 at a core size of 0.85 nm and decreases to almost zero for the largest core size, while the CdSe peak sum is continually increasing from almost zero for the smallest core size to 2.5 at a core size of 2.1nm, before slightly decreasing for the largest core.

- In the case of wurtzite lattice structure including internal potentials, the acoustic peak sum has a maximum of 34.3 at a core size of 0.6nm, then decreases to values around 5 for larger cores, before increasing again to 10.5 for the largest core size.

  The intermediate peak is much less pronounced, while following the general trend of the acoustic peak in terms of the positions of its maxima.

  The CdS peak sum has two maxima, one at a core size of 0.6 nm at a value of 11.7 and another one at a core size of 1.6nm with a value of 7.7 . It decreases for the largest quantum dots, yet in contrast to the zincblende case, does not approach zero, reaching a minimal value of 3.8 .

  Similar to the zincblende case, the sum of the CdSe peak is increasing for larger core sizes, with the increase being largest for core sizes of 1.6nm and above. The quantum dot with the largest core size also exhibits the largest Huang-Rhys sum for the CdSe peak, at 31.3 .

- If the internal potentials are omitted for the wurtzite structure, the peak sums for quantum dots with core sizes larger than 0.85 nm are drastically decreased, to values comparable to the zincblende results. Both the acoustic peak and the CdS peak decrease to zero at the largest core size, while the intermediate peak is already at effectively zero for core sizes starting from 1.6 nm. The CdSe peak also decreases with increasing core-sizes, reaching a value of 0.44 for the largest core.

Lastly, we analyse the variation of the peak widths:

- The widths of all observed peaks are between 10 and 30 wavenumbers, confirming the fact that we are really examining well defined peaks, as opposed to random variations in coupling strength.

- As a general trend for all examined quantum dot series, the width of the CdS peak is constant around 10 wavenumbers for smaller core sizes, before strongly increasing up to about 25 wavenumbers for core sizes starting at 1.6 nm.

- For the zincblende quantum dots, the widths of the other three peaks are all relatively constant at around 7-10 wavenumbers, a result consistent with the well-defined peaks in the spectra in figure 7.1
- For wurtzite lattice structure including internal potentials, the CdSe and acoustic peak widths both exhibit a maximum at a core size of 0.35 nm and remain constant thereafter, at about 15 wavenumbers, while the width of the intermediate peak is the largest of all peaks, increasing to over 25 wavenumbers for large core-sizes.
- When omitting the internal potentials, the widths remain mostly identical up to a core-size of 1.35 nm, after which the acoustic, intermediate and CdSe peak widths all strongly decline, compared to the case with potentials included, and all reach values between 5 and 10 wavenumbers for the largest core-sizes.

We conclude that the peak widths are generally larger for quantum dots with wurtzite structure, which changes when internal potentials are omitted. Then the widths become very similar to the zincblende case, but only for larger quantum dot cores. In experiment, this might be visible in the width of raman peaks or phonon satellites in photoluminescence measurements, provided the excitation lightsource is sufficiently spectrally narrow, and the examined quantum dots display only very small size or shape variations.

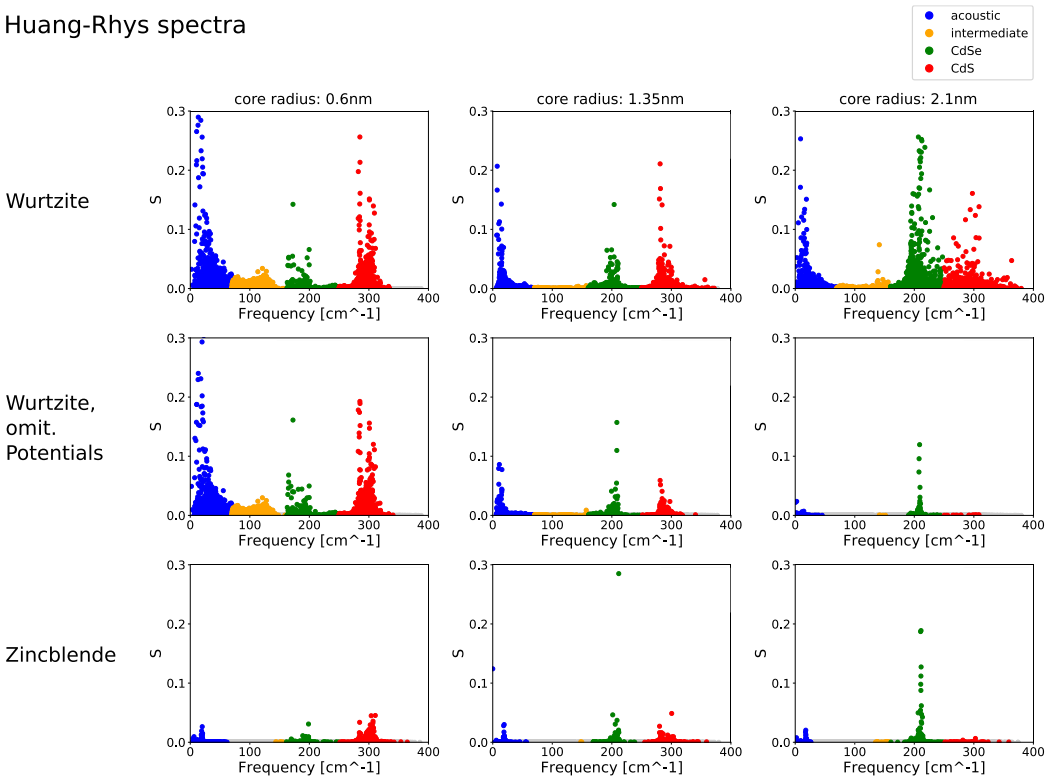

Figure 7.1: Calculated Huang-Rhys spectra for three different exemplary geometries from series A1. In the first row of plots, results for wurtzite lattice structure are displayed for calculations including the internal electric potentials. The second row of plots shows results for wurtzite structure, where internal potentials have been omitted. In the bottom row, results for zincblende lattice structure are shown. The left column shows results for quantum dot geometry A1-3, with a core radius of 0.6 nm. The middle column shows results for quantum dot geometry A1-6, with a core radius of 1.35 nm. The right column shows results for quantum dot geometry A1-9, with a core radius of 2.1 nm.

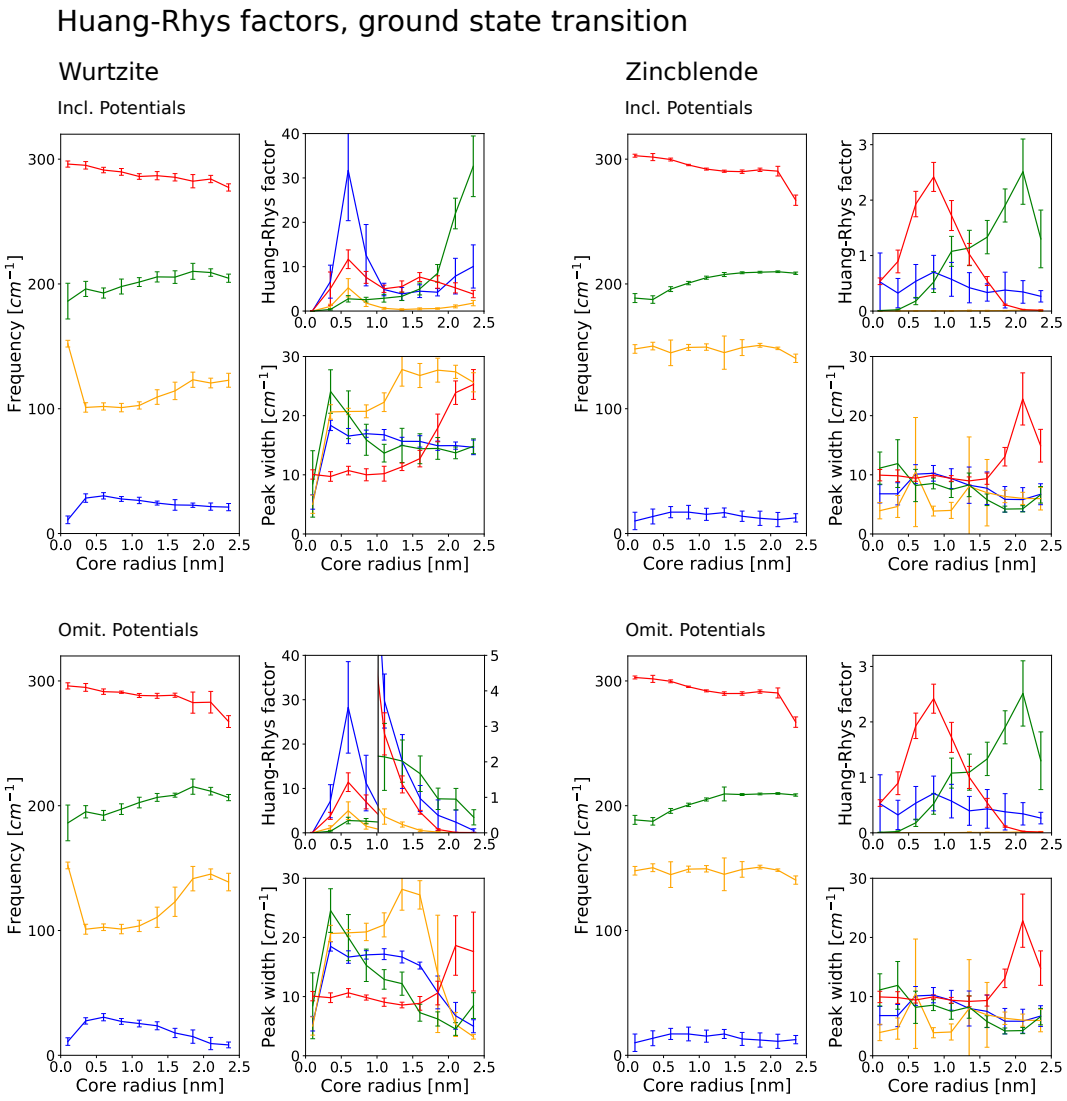

Figure 7.2: Analysis of the peaks observed in the Huang-Rhys spectra for the electronic ground state transition based on single-particle wavefunctions. Results are for quantum dot geometries of series A1. Results for wurtzite lattice structure are shown on the left half of the figure, while results for zincblende are given on the right side. The top row depicts results obtained from single-particle wavefunctions calculated including internal electric potentials, while the bottom row details results where these potentials are omitted. Each set of results contains three plots, showing the peak center frequency, the sum of the peaks Huang-Rhys factors, and the peak width, for all four analyzed peak regions. The plot of the peak-sums for the wurtzite case with internal potentials omitted is a combination of two plots: results for core-sizes up to 1 nm are plotted on a different y-axis than results for larger core-sizes.

7.2 Excited state transitions

We continue our analysis of the Huang-Rhys calculations by turning our attention to a different transition of the electronic configuration: instead of the lowest exciton state, formed by the ground-states of both the electron and hole single-particle calculations, we study the radiative decay of two different exciton states, one of which consists of the ground state of the hole and the first excited state of the electron, while the other consists of the electron ground-state and the first excited state of the hole. The final state of the electronic transition is the empty quantum dot, as was the case in our prior analysis.

The Huang-Rhys spectra resulting from these transitions share the same characteristics as the ones displayed in figure 7.1 above, and are therefore not plotted. Analysis data of the different peaks found in the spectra are displayed in figure 7.3 for the two transitions described above, for quantum dots in zincblende and wurtzite structure. In the case of wurtzite, we again differentiate between two cases, one of which includes the internal potentials in the calculation, and one where they are omitted.
We will analyse the differences compared to the ground-state exciton above for each of the cases separately.
In the case of the transition with an excited electron state for wurtzite quantum dots including potentials the results are very similar to the ground-state exciton. For the transition involving the excited hole state, however, the peak sums for quantum dots with small core sizes are strongly decreased, and the width of the CdSe peak is also decreased in the same core-size range.
When omitting the internal potentials of the wurtzite quantum dots, the peak center frequencies for both the excited electron and the excited hole case remain largely unaffected, when compared to the ground state exciton case. For the transition involving the excited electron state, the peak sums display the same decrease towards larger core sizes, except the sum of the CdSe-peak, which is strongly enhanced when compared to the ground state exciton transition. The values for the CdS peak sum are also enhanced for smaller core sizes. The peak widths are largely unaffected, except for the intermediate peak, where the width is increased slightly. In the case of the excited hole state transition, the peak sums are reduced by a factor of 2, with the acoustic peak sum even more strongly suppressed. The CdSe peak displays the same trend towards large core sizes as in the case of the excited electron state transition. The peak width are similar to the excited electron case.
For the zincblende dots the frequencies of the peaks match the data for the ground-state transition for both transitions discussed here. For the excited electron transition, the peak sums display the same general trends seen in the ground-state transition, yet their magnitude is increased by more than a factor of 2. The peak widths are also increased, but only for smaller core-sizes. In the case of the transition with an excited hole state, the peak sums are greatly decreased, with no single sum being above a value of 0.5, while the peak widths match the behaviour seen for the ground state transition.

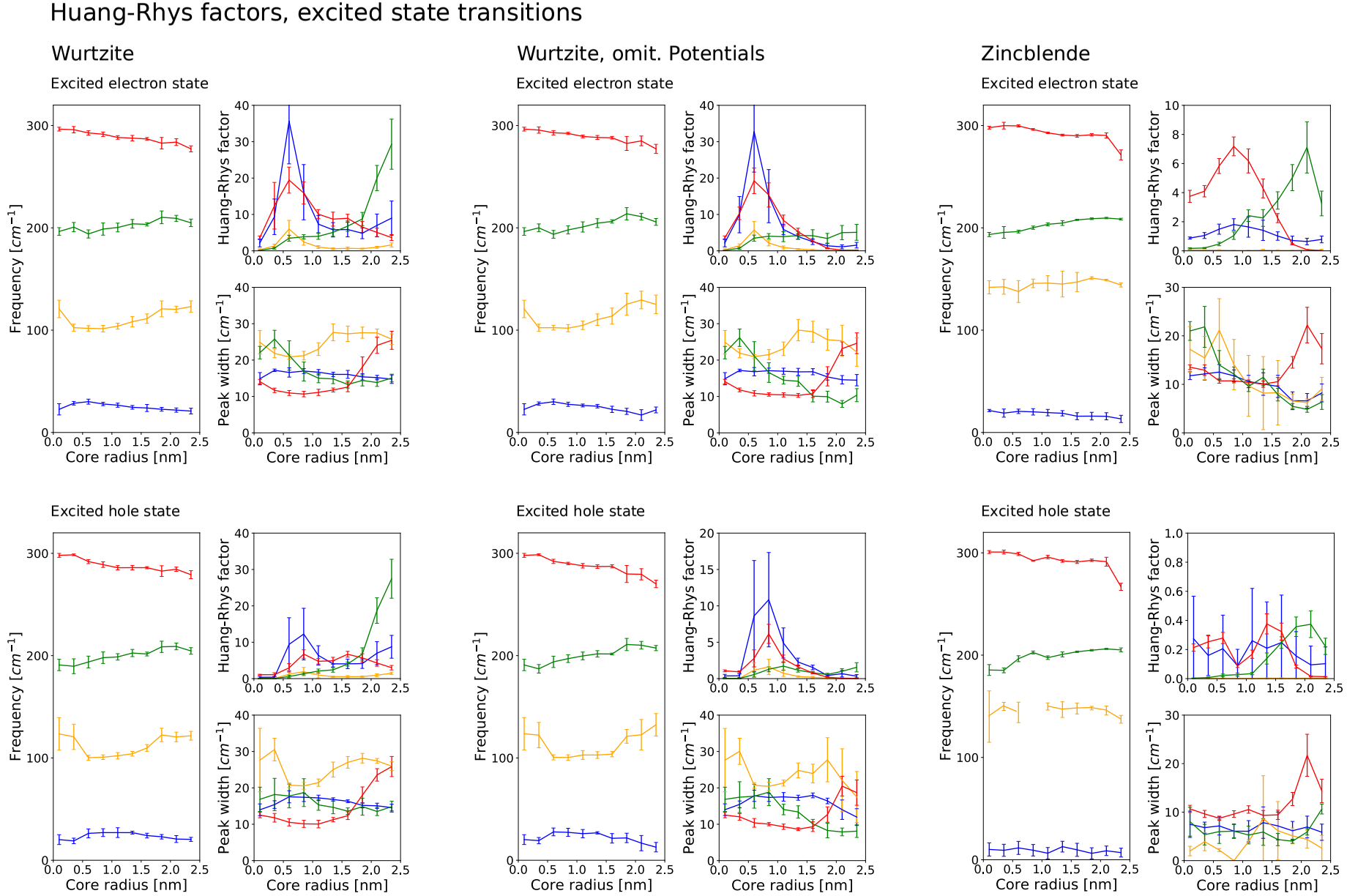

Figure 7.3: Analysis of the peaks observed in the Huang-Rhys spectra for the higher energy electronic state transitions based on single-particle wavefunctions. Results are for quantum dot geometries of series A1. Results for wurtzite lattice structure, with internal potentials included in the single-particle calculations, are shown in the left column, while in the middle column results for wurtzite lattice structure, where internal potentials were omitted are shown. Results for zincblende are given in the right column. The top row depicts the electronic transition where the configuration before the transition consists of the single-particle hole groundstate and the first excited single-particle electron state. The results in the bottom row are obtained with an initial configuration of the electron single-particle ground state and the first excited single-particle hole state. The final electronic configuration is an empty quantum dot for both transitions.
Each set of results contains three plots, showing the peak center frequency, the sum of the peaks Huang-Rhys factors, and the peak width, for all four analyzed peak regions.

7.3 Hartree-Fock exciton transitions

So far, we have modeled the coupling dynamics of the localised phonons only to changes in electronic configurations made up of single-particle wavefunctions.
In the next step, we will analyze the interactions with the vibrational eigenmodes of the excitonic transitions using the wavefunctions obtained from the Hartree-Fock calculations from chapter 6. Figure 7.4 shows the results for four such transitions, the recombination of the excitonic states $X_1 \uparrow\Downarrow$, $X_1 \uparrow\Uparrow$ and $X_2 \uparrow\Downarrow$ with the final state in these cases being an empty quantum dot.
As a fourth case, the relaxation of the excitonic state $X_2 \uparrow\Downarrow$ into the excitonic state $X_1 \uparrow\Downarrow$, which has a lower energy. Note that in this last case, we violate the assumption of our exciton-phonon coupling model, namely that we only consider changes in electronic configurations that are induced by radiative recombination, because the electronic transition in this last case is more likely associated to other mechanisms associated with the relaxation of charge carriers to the energy minimum, such as Auger-recombination. Yet the evaluation of this particular change in electronic configuration may yield insight into the probability of the participation of localised phonons in these kinds of inter-excitonic relaxations.
Analysing the calculations, we first note that the results for the recombination of the $X_1 \uparrow\Downarrow$ and $X_1 \uparrow\Uparrow$ excitons are identical. This, of course originates from their associated wavefunctions' probability distributions being identical as well, as shown in figure 6.9.
Moreover, the results for the X_1 excitons are very similar to the ones obtained for the single-particle ground-state transition, which is due to the close resemblance of the wavefunctions of the corresponding excitons to the single-particle wavefunction.
The $X_2 \uparrow\Downarrow$ has a different hole wavefunction associated to it, leading to a change in the resulting Huang-Rhys factors. This is most strongly seen as a decrease in the peak sum of the CdSe peak for large core-sizes. Both the peak frequencies and the peak widths remain largely unchanged. The results closely resemble the ones found for the configuration involving the excited hole single-particle state including internal potentials depicted in figure 7.3. This is again due to the close resemblance of the hole wavefunction of the X_2 exciton to the excited hole wavefunction used before.
The results for the inter-exciton transition show a decrease of Huang-Rhys factors for the CdSe and CdS peaks by an order of magnitude. The acoustic and intermediate peak sums are lowered as well. The CdSe peak sum retains its trend of increasing for larger quantum dot core sizes, while the CdS peak sum is also similar to before.
The acoustic peak sum shows an inverted trend to the ones before, decreasing for larger cores.
Interestingly, the peak frequencies are unaffected by the shift to this inter-excitonic transition, and the peak widths also remain very similar.
It would also be of interest to examine the transitions between different X_1 excitons, yet this exceeds the capabilities of our model, because the probability density of their associated wavefunctions is identical, as they only differ in their associated spin projections. This leads to no change in charge-density induced by the change in electronic configuration, making all Huang-Rhys factors zero.

The same argument holds for all transitions between different X_2 excitons.

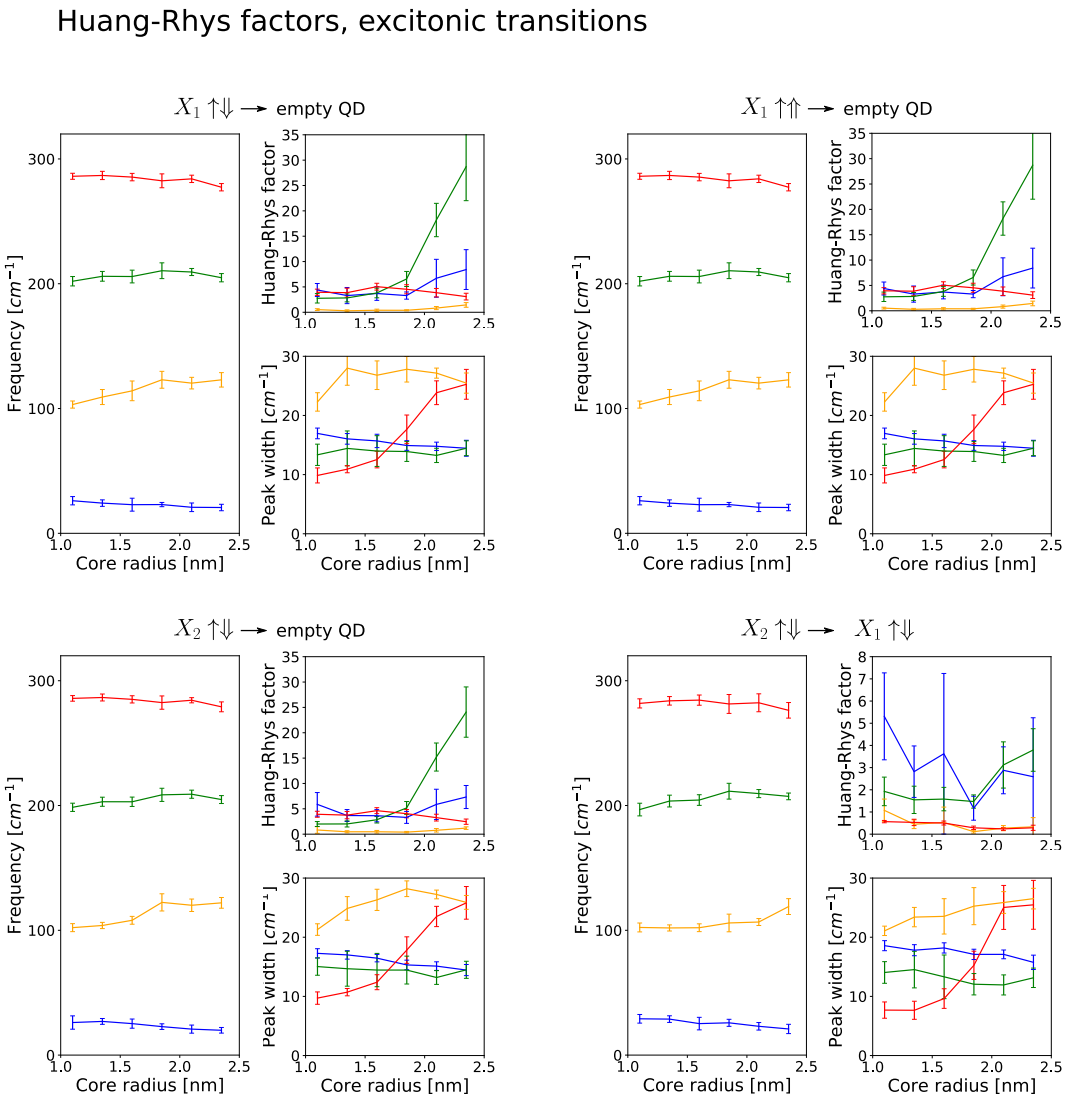

Figure 7.4: Analysis of the peaks observed in the Huang-Rhys spectra for optical transitions between Hartree-Fock exciton states. Results are for quantum dot geometries of series A1. Results for four separate electronic transitions are shown. Three transitions describe the radiative recombination of a Hartree-Fock exciton: $X_1 \uparrow\Downarrow$ on the top left, $X_1 \downarrow\Downarrow$ on the top right and $X_2 \uparrow\Downarrow$ on the bottom left. The fourth set of results is obtained for a transition from the $X_1 \uparrow\Downarrow$ to the $X_2 \uparrow\Downarrow$ exciton. Each set of results contains three plots, showing the peak center frequency, the sum of the peaks Huang-Rhys factors, and the peak width, for all four analyzed peak regions.

7.4 Summary

We successfully applied the model for Huang-Rhys factor determination introduced by Kelley [19] to core-shell quantum dots using wavefunctions both from single-particle $\mathbf{k}\cdot\mathbf{p}$ calculations and Multi-Particle Hartree-Fock calculations. The addition of the CdS-Shell leads to the appearance of an additional peak in the spectrum of Huang-Rhys factors in close vicinity to the CdS bulk LO-phonon frequency. We further observe peaks at low frequencies and in the vicinity of the bulk CdSe LO-phonon frequency, which were also discovered by Kelley. Additionally, we observe an additional, smaller peak arising between

100 and 130 wavenumbers, yet not for all examined quantum dots.
We have performed systematic studies of the peak sums, positions and widths for a variety of core-shell geometries for both lattice structures. This has led us to several key findings:

- The center frequencies of the peaks are mostly unaffected by the different electronic configurations examined. They are only dependent on the quantum dot geometry and the lattice structure. This leads us to the conclusion that only localised phonons in limited frequency areas show coupling to the electronic system, and the frequency shifts observed for different quantum dot geometries are largely due to changes in strain in the core and shell, induced by a different volume share of CdSe and CdS.

- The peak attributed to CdSe displays an increasing amplitude towards larger core sizes, while the peak attributed to CdS displays increased amplitude for smaller core sizes. This relates very closely to the change in volume share of the two materials. Therefore, we conclude that our attribution of these peaks to the two different materials is valid.

- The peak sums for all peaks strongly increase for wurtzite lattice structure as opposed to zincblende lattice structure. This effect can be mitigated by omitting the internal potentials in the wurtzite calculations, in which case the peak sums are similar to the zincblende case for larger core-sizes, yet remain large for small cores. We think that this is due to the wavefunction separation seen in the wurtzite calculations, which is mostly induced by the internal potentials. For zincblende, the electron- and hole-wavefunctions are both centered in the middle of the quantum dot, leading to the overall charge density of the resulting exciton to have much smaller amplitudes than the charge density of an exciton constructed from separated wurtzite wavefunctions.

  Since the method used for calculating Huang-Rhys factors scales with the overall charge-density of the electronic configuration, this leads to the strongly enhanced Huang-Rhys factors obtained in our calculations.

  Since the coupling found in experiment does not show such strong discrepancies between the two lattice structures, we come to the conclusion that the results we obtain for the wurtzite case are unphysical in their amplitude.

  One explanation for this can be found in a violation of one of the assumptions of the model we used. Namely, it was assumed that the vibrational eigenmodes are unaffected by the change in electronic configuration, even though the partial charges of the atoms are affected by the electronic configuration, and these partial charges are incorporated in the interatomic potentials. This is a reasonable assumption in the case of zincblende, where the induced changes in partial charge are small, yet might not be as valid in the case of separated wurtzite wavefunctions.

  Another possible explanation is that the extent of the wavefunction separation might be overestimated by our calculations.

  We believe that even though the peak sums calculated for wurtzite quantum dots are perhaps unreasonably high, the evaluation of their relative change for differ-

ent quantum dot geometries and the evolution of the center-frequencies are valid, nonetheless.

8 Properties of localised Phonons

We will now shift our attention towards the vibrational eigenmodes obtained from the atomistic calculations outlined in chapter 2.6. Because of the lack of translational symmetry in our quantum dots, these are not identical to the phonons found in bulk semiconductors, but can rather be compared to molecular vibrations, when imagining the colloidal quantum dot as a very large molecule. Our aim then, is to identify patterns in these vibrational motions, and find similarities and differences to the dynamics found in classical bulk phonons on an atomic scale. On this account, we have introduced in chapter 2.6.4 a set of measures to be determined for each eigenmode, for the simple reason that the number of eigenmodes is too large and their dynamics too complex to examine each one by hand.

8.1 Amplitude Distribution and Localisation

Figure 8.1 shows, for one exemplary quantum dot, the results of the phonon-analysis, as described in chapter 2.6.4. On the left side, the raw data is displayed. While one can clearly make out general trends, the graphs are quite noisy, complicating further analysis. For this reason, we applied a Savitzky-Golay filter [53] to the calculated data. The filtered data is plotted on the right side, and allows for a much easier analysis of the different graphs.
We will therefore use the filtered data to analyse the properties of the calculated vibrational eigenmodes, and compare the results for different quantum dot geometries as well as different lattice structures.
On this account, we have plotted the amplitude distribution and localisation results for both lattice structures for three different quantum dot geometries from series A1 in figure 8.2.
The first thing to note is that for each geometry, the results of both the amplitude distribution and the localisation analysis are very similar between the two lattice structures, in regard to the position as well as the amplitudes of the maxima and minima.
We identify five distinct frequency areas that show strongly different properties of the associated vibrational eigenmodes. In figure 8.3 there are three-dimensional plots of representational eigenmodes for each of these areas:

1. 0 - 140 cm^{-1}: Strongly delocalised, non-surface eigenmodes:

    - In this whole frequency range, the amplitude is decreased at the surface, yet otherwise relatively equally distributed through all other quantum dot regions. Only for the largest core size is the shell amplitude also decreased, which is due to the very thin shell largely coinciding with the surface area.
    - The localisation of all modes in this frequency range represents the minimum of localisation observed, except for a few outliers close to zero frequency.
    - There are some small maxima observed for the core amplitude distribution at 40 and 120 wavenumbers, yet those are small deviations compared to the other frequency regions.

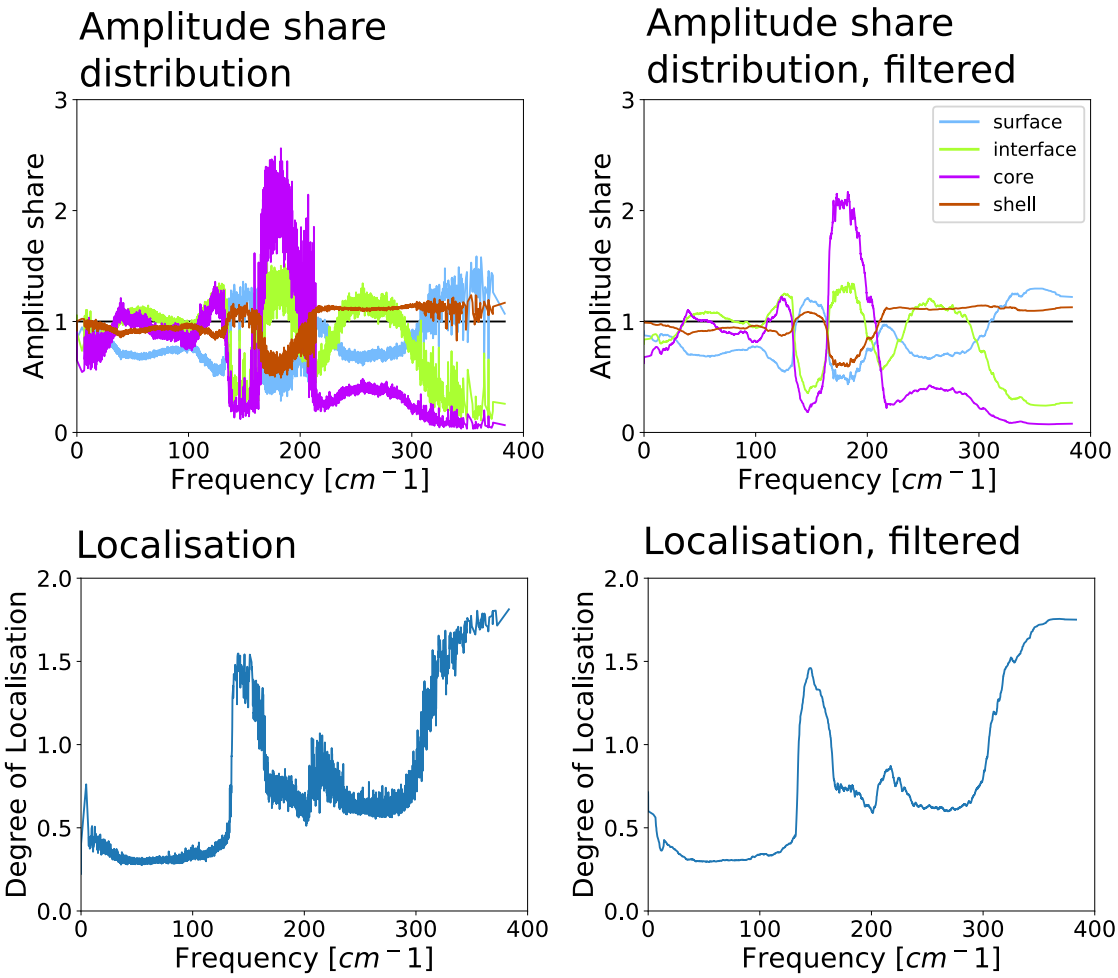

Figure 8.1: Unfiltered and filtered results of the amplitude distribution and localisation of the phonon modes for quantum dot geometry A1-7 with wurtzite lattice structure. Unfiltered results are shown on the left side, while on the right side, the same results are plotted after a Savitzky-Golay filter has been applied. On the top row, the results of the amplitude distribution analysis are given, while phonon localisation is shown on the bottom row.

- The visual representation of one eigenmode from this frequency range, found in figure 8.3 part (a), confirms these findings, as the amplitudes of the vibrational dynamics are spread through the entire quantum dot. Furthermore, we note that the amplitudes appear to be distributed evenly among atoms from both sublattices.
- Overall, vibrational eigenmodes in this frequency region are homogeneously distributed through the whole quantum dot, and therefore strongly resemble the behaviour of bulk phonons. The fact that both sublattices are subject to the motion, as opposed to only one sublattice moving relative to the other, is another similarity to the atomic motion associated to acoustic phonons in bulk structures, where neighbouring atoms move in-phase.

2. 140 - 170 cm^{-1}: Strongly localised surface modes:

   - The core amplitude share drops to almost zero for all but the largest core-size in this region, while the surface amplitude share shows a distinct maximum for the small and medium core sizes. For the large core-size, the maximum is observed in the interface amplitude share. This can be attributed to the fact that for large cores, the interface is rather close to the surface.
   - The localisation results for this frequency range display a very distinct maximum for all considered core sizes.
   - In figure 8.3 (b), these findings are confirmed, as the atomic motion is strongly confined to a small area at the quantum dot surface. Also notable is the fact that the dynamics are not confined to one sublattice, as the Cadmium atoms also display motion amplitudes, albeit to a smaller degree than the Sulfur atoms.
   - Thus the vibrational eigenmodes associated to frequencies in this range are strongly localised vibrations close to the quantum dot surface, strongly differing from the properties associated to bulk phonons.
   - Localised surface phonons in small spherical nanocrystals have also been calculated in the context of continuum dielectric theory [54, 55], and their impact on the electron-phonon coupling has been studied in [43].

3. 170 - 210 cm^{-1}: Core modes:

   - The amplitude share of the quantum dot core is strongly enhanced in this frequency area for all displayed geometries. For the small and medium core sizes, the interface amplitude share is enhanced as well, while it is close to unity for the largest core size. The amplitude shares of the shell and surface are simultaneously decreased for all geometries.
   - The localisation results for this frequency range show the following trend: for the smallest core, they are uniformly high, though smaller than for the surface modes dicussed above. For increasing core sizes, they decrease, until they are almost as low as the values for the delocalised region below 140 wavenumbers.

- The 3D-visualisation of a representational eigenmode from this frequency range found in figure 8.3 (c) confirms the confinement to the core as well as the homogenous distribution inside the core. It is notable, that the confinement is not complete, as some areas in the quantum dot shell also display atomic motion.
- From these findings, we can deduce that the eigenmodes associated to this frequency range are mostly confined to the quantum dot core, and are homogeneously distributed inside the core.

4. 210 - 320 cm^{-1}: Shell modes:

   - The core amplitude share drops sharply in this frequency area. In the case of small and medium core sizes, there is still a noticeable contribution of the core for frequencies between 230 and 300 wavenumbers, the core contribution is uniformly low for the large core
   - For the small and medium core quantum dots, the surface contribution is diminished as well, while the contribution of the interface is close to unity. This changes for the large core, where both the surface and interface more than proportionally contribute to the atomic motion.
   - The values for the localisation show an inverted trend when compared to the core modes above: They are small for small cores, and then increase for larger cores.
   - The visual representation of an eigenmode from this frequency area, depicted in figure 8.3 (d), shows that the dynamics are strongly confined to the Sulfur atoms, and therefore to the quantum dot shell. This is similar to the dynamics of bulk optical phonons, where neighbouring atoms move with inverse phase.
   - We conclude from these findings, that the vibrational eigenmodes in this frequency range are confined to the shell of the quantum dots, and the atomic motion is distributed homogeneously inside the shell volume. This leads to increased values of localisation if the overall shell volume is reduced.

5. $>$ 320 cm^{-1}: Strongly localised surface modes

   - The area of the largest frequencies observed in the atomic motion calculation shows almost no contribution from the quantum dot core, and only for the largest core can we observe a contribution from the core-shell interface. The contribution of the surface, however, is increased for all considered geometries.
   - The localisation values calculated for the phonons show a strong increase with frequency, and display the largest values calculated for all eigenmodes.
   - Similar to the eigenmodes in the frequency range between 140 and 170 wavenumbers, the visualisation of one mode from this frequency range, depicted in figure 8.3 (e), shows a strong confinement to a small area on the quantum dot surface. Differing from the surface mode at lower frequencies, however, the motion of the Cadmium sublattice is notably decreased.

- Thus, the vibrational eigenmodes making up this frequency section are strongly localised surface modes.

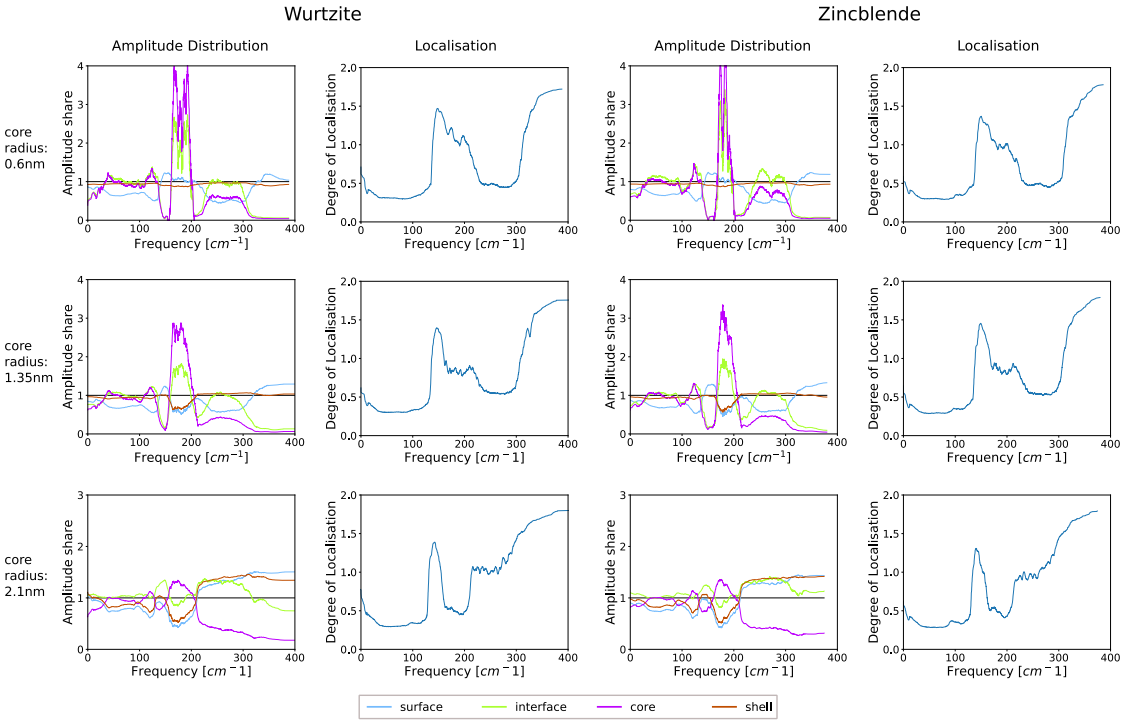

Figure 8.2: Filtered amplitude distribution and localisation results for quantum dots from series A1. Results for wurtzite are depicted in the first two columns, while results for zincblende are shown in the last two columns. The three rows of plots show results for quantum dots with core radii of 0.6 nm, 1.35 nm and 2.1 nm, respectively.

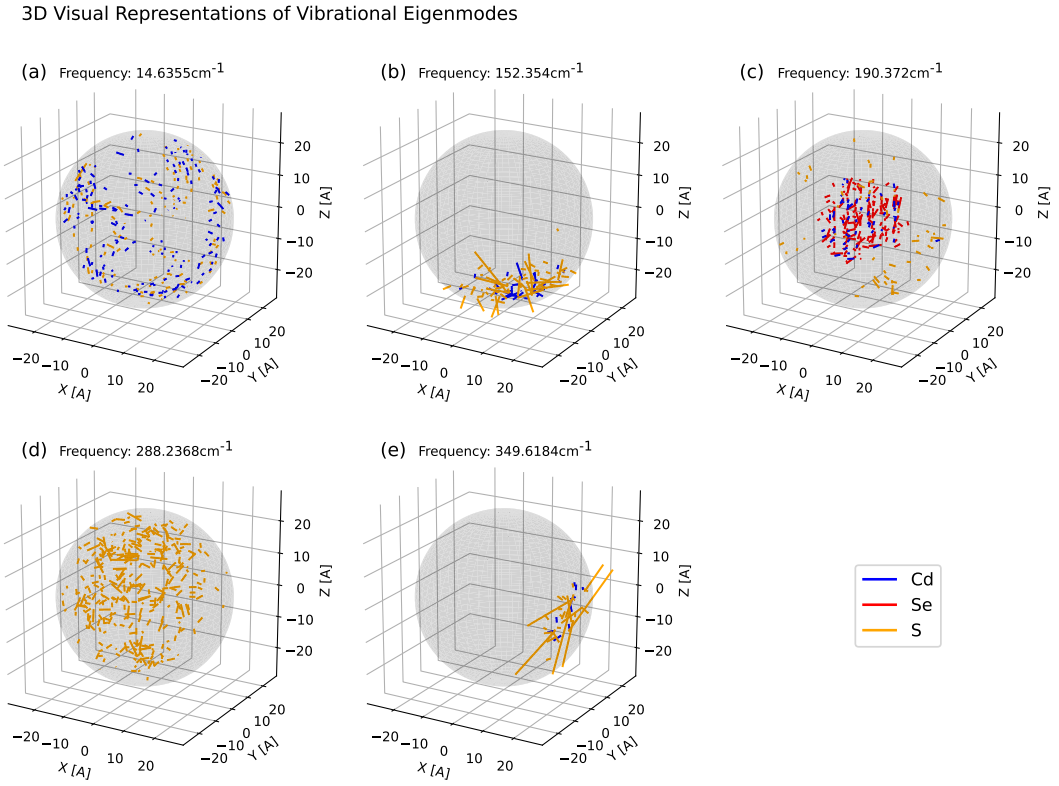

Figure 8.3: 3D plots of vibrational eigenmodes are displayed. Motion amplitudes and directions of single atoms are indicated by lines, with the line-length proportional to the motion amplitude. Lines are colour-coded by atom-type. Only atoms with significant motion amplitudes are depicted, to increase readability. Representational vibrational eigenmodes for each frequency region identified in chapter 8.1 are shown: (a) Strongly delocalised, non-surface eigenmodes (b) Strongly localised surface modes (c) Core modes (d) Shell modes (e) Strongly localised surface modes

8.2 Properties of phonons with significant Huang-Rhys factors

We will now examine the properties of the vibrational eigenmodes which contribute to the Huang-Rhys factors examined in chapter 7. In figures 8.4, 8.5 and 8.6, the amplitude distribution results for core, shell, interface and surface, as well as the localisation results are plotted for every eigenmode for quantum dot geometries from series A1 with a core radius of 0.6 nm, 1.35 nm and 2.1 nm, respectively, for both lattice structures. Phonons, which have an associated Huang-Rhys factor larger than 0.01 for the excitonic ground state transition, as depicted in figure 7.1, are highlighted by colour.
This allows us to make the following observations:

- All vibrational eigenmodes that display contributions to the acoustic peak in the Huang-Rhys spectrum are part of the strongly delocalised, non surface regime described above. This lends further credibility to our naming convention, as the eigenmodes in this frequency range very much act like bulk acoustic phonons.

- Phonons contributing to the intermediate peak are only found for the core radii 0.6 nm and 2.1 nm and only for wurtzite quantum dots. In the case of the small core radius, they are more than proportionally located at the core-shell interface, and have a very low amplitude at the surface. Their localisation is uniformly low.

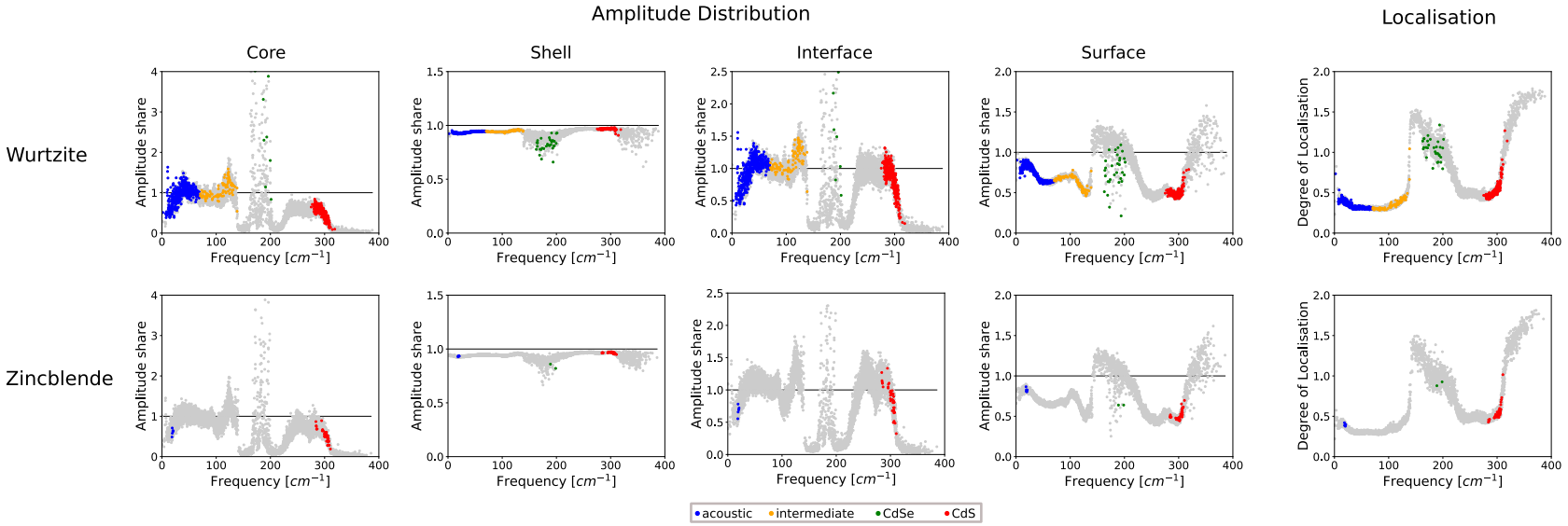

Figure 8.4: Unfiltered results for the different amplitude distribution and the localisation calculations for quantum dot geometry A1-3 with a core radius of 0.6 nm. Phonons which exhibit significant Huang-Rhys factors for the single-particle ground state recombination are colour coded.

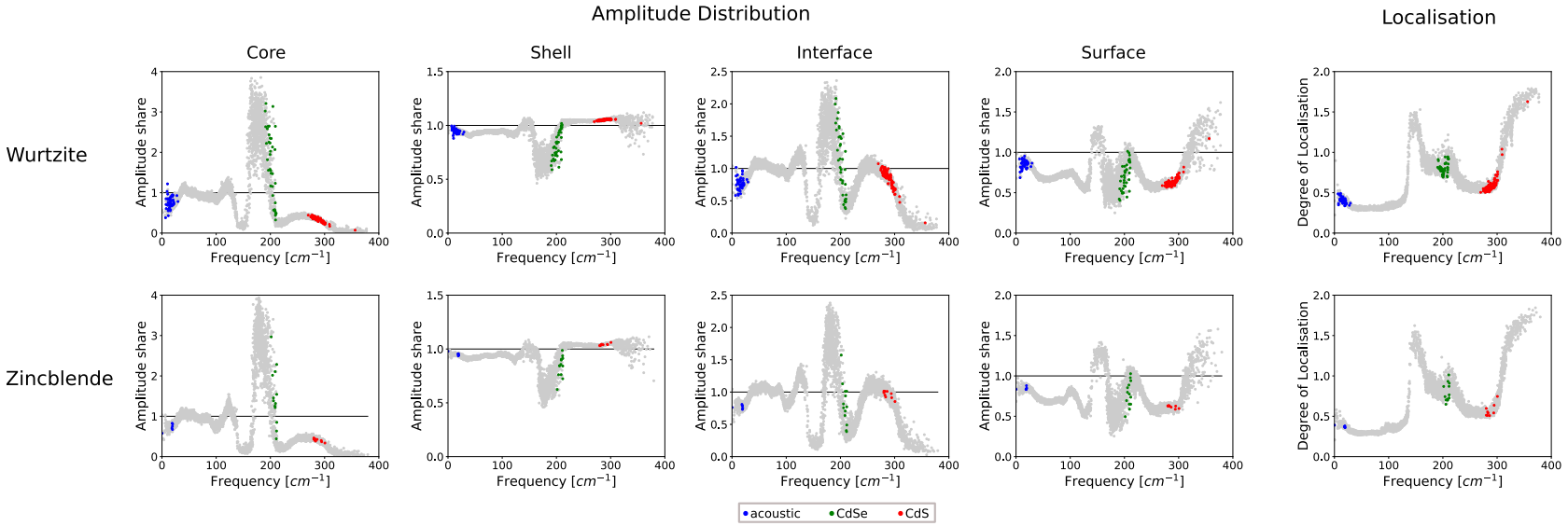

Figure 8.5: Unfiltered results for the different amplitude distribution and the localisation calculations for quantum dot geometry A1-6 with a core radius of 1.35 nm. Phonons which exhibit significant Huang-Rhys factors for the single-particle ground state recombination are colour coded.

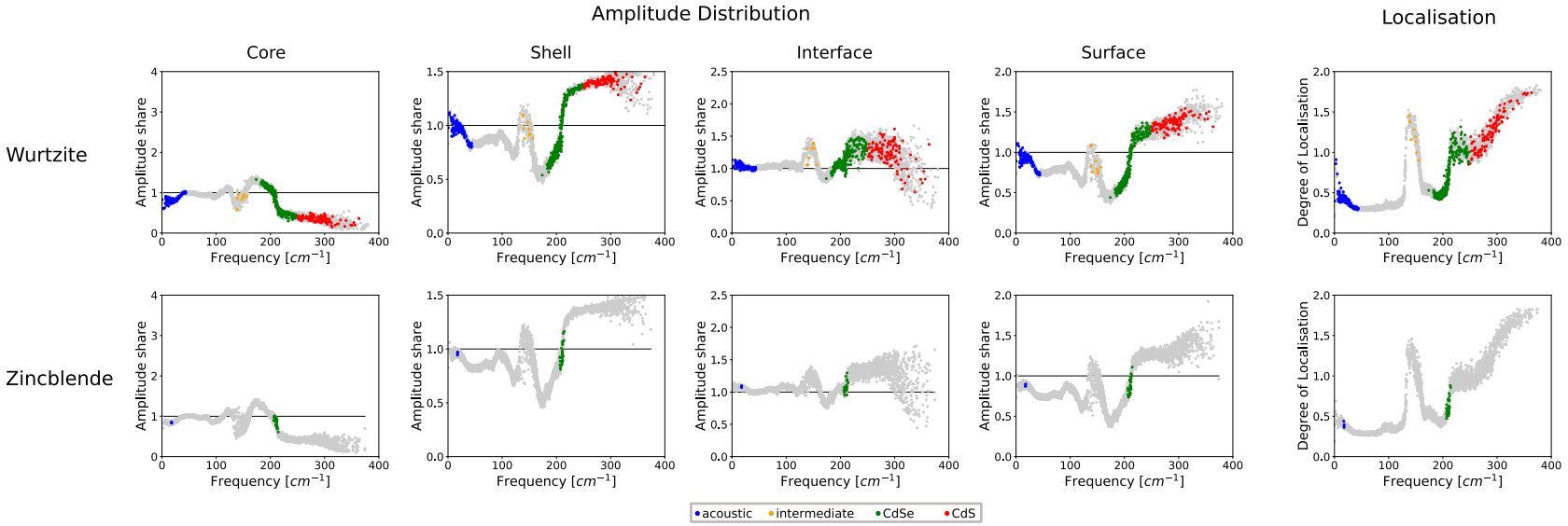

Figure 8.6: Unfiltered results for the different amplitude distribution and the localisation calculations for quantum dot geometry A1-9 with a core radius of 2.1 nm. Phonons which exhibit significant Huang-Rhys factors for the single-particle ground state recombination are colour coded.

In the case of the large core size, the modes are also located superproportionally at the quantum dot interface, yet are also present at the quantum dots surface, which is attributable to the thin quantum dot shell. In contrast to the case for small core size, all contributing modes are located inside the peak of the localisation parameter.

- The phonons contributing to the CdSe Huang-Rhys peak are all located on the border between the core-modes and the shell modes. They exhibit a wide variety of amplitude distributions in the core and shell regions as well as the interface region. Yet they all are contributing less than proportionally to the surface region. We conclude that the CdSe peak in the calculated Huang-Rhys spectra is not entirely comprised of phonons belonging to the core-modes, but also shows contributions from the atomic motions in the quantum dot shell.

- The phonons comprising the CdS peak in the Huang-Rhys spectra, however, are all found to be part of the shell-modes. They are suppressed both inside the quantum dot core and its surface, and are homogeneously distributed inside the quantum dot shell.

- The surface modes observed both between 140 and 170 wavenumbers and above 320 wavenumbers do not show strong coupling to the electronic transitions, aside from a few outliers at high frequency, particularly for the largest core size.

8.3 Summary

We have introduced a method to study the properties of the large number of vibrational eigenmodes of the examined quantum dots heuristically, by calculating the amplitude distribution among the core and shell, as well as the interface and surface regions, and introducing a measure for the localisation of the eigenmodes.
Using these heuristics, we are able to identify five distinct frequency regions, where the associated eigenmodes display unique properties. In three of these frequency regions, the vibrations display properties similar to those found for bulk phonons, while in the other two, we find strongly localised surface vibrations. These heuristic findings are confirmed by three dimensional visualisations of representational eigenmodes from each of the distinct frequency ranges.
We conclude by analysing the properties of the phonons with notable contributions to the Huang-Rhys coupling factors calculated in chapter 7, finding that almost all of them are resembling bulk phonons.

9 Summary

We have calculated the strain distributions and internal potentials for core-shell quantum dots of various geometries for both zincblende and wurtzite crystal structure. While the strain distributions are quite similar for the two lattice structures, the internal potentials are drastically different; for wurtzite, they lead to a polarisation along the [0001]-axis, while for zincblende, they are much smaller in amplitude and display no polarisation.
Influences of the dielectric environment of the quantum dot, while very significant for the potentials outside the quantum dot and in the quantum dot shell, are shown to be negligible inside the quantum dot core, where the electronic wavefunctions mostly reside. Furthermore, it was shown, that adding additional shells to the quantum dot geometry could lead to the screening of the polarisation potentials inside the quantum dot core for wurtzite quantum dots.
Subsequently, the effects of the internal potentials on the electronic structure are studied using $\mathbf{k}\cdot\mathbf{p}$-theory. We find that, for zincblende, the influence of the potentials on the single-particle energies and wavefunctions is negligible, while for wurtzite, the polarisation of the potentials leads to a separation of wavefunctions and a decrease in effective bandgap, as well as an exponential increase in radiative lifetimes, summarised as the quantum confined Stark effect (QCSE).
We also find that for non-spherical quantum dots, modeled as ellipsoids with varying aspect ratios, degeneracies in the single-particle energy structure are lifted, and that deviations from sphericity, even when the total quantum dot volume is retained, can induce strong shifts in effective bandgap.
We expand our analysis of the electronic structure by calculating excitonic states via an iterative Hartree-Fock algorithm. These excitons replicate the results from the single-particle picture, showing a strong quantum confined Stark effect induced by internal potentials, but also add additional insight into the radiative properties and energy structure of the excitons. We find that the lowest energy excitons, with parallel electron and hole spins, are not classical dark-states that show no radiative recombination, but exhibit finite lifetimes, that are a factor of 4 to 5 times higher than those found for the excitons with antiparallel spin, the classical bright states. This is due to the B and C valence band contributions to these excitons, which contain components of opposite spin. This result yields an alternative explanation of luminescence from the assumed dark states, which is reported in literature [15], and explained with the interaction of the dark-states with magnetic fields or phonons.
We then provide results for the exciton-phonon coupling in colloidal core-shell quantum dots, analysing Huang-Rhys factors for a series of quantum dot geometries for both crystal structures. We find, that the vast majority of the vibrational eigenmodes display no coupling to the exciton dynamics, and that those that do show coupling, are relegated to several small regions in frequency. This leads to three distinct peaks in the spectra of Huang-Rhys factors, attributed to low energy vibrational eigenmodes, akin to acoustic phonons in bulk, and eigenmodes with energies comparable to the bulk LO phonons of CdSe and CdS, respectively.
We find that the coupling is an order of magnitude stronger for wurtzite quantum dots

compared to zincblende. We attribute this to the wavefunction separation, as the results are much closer when internal potentials are omitted in the wurtzite calculations. Overall it was found that the center frequencies of the Huang-Rhys peaks are not strongly different for different electronic transitions, but the total Huang-Rhys factor of the peaks was affected.
Changes in peak frequency observed for variations in quantum dot geometry can be attributed to a changed strain distribution inside the quantum dot. The standard deviation of the peak frequencies, or width of the peaks, is also found to be larger for wurtzite structure compared to zincblende.
In the final part, we perform an analysis of the vibrational eigenmodes themselves, employing self-designed measures for the distribution of vibrational amplitudes inside the different regions of the quantum dot (core, shell, interface, surface) as well as for the spacial localisation of the atomic motion. We find that the vibrational eigenmodes can be split into five distinct groups, designated by specific frequency regions, of which three, modes located in the whole quantum dot excepting the surface, modes located inside the core and modes located inside the shell display similar dynamics on the atomic scale as would be expected of classical bulk phonons, while the other two, strongly localised surface modes observed in two distinct frequency regions, are more comparable to strongly localised molecular vibrations.
We further find, that those vibrational eigenmodes, which exhibit notable Huang-Rhys factors, all belong to the three groups of modes that are comparable to bulk phonons.
When assessing the validity of our results, we come to the following conclusions:

- The magnitude of the internal potentials might be overestimated. This is due to two different reasons: first, we decided to use the vacuum-value of $\varepsilon_r = 1$ for the environment dielectric constant, which could underestimate the amount of screening the potentials might undergo in realistic conditions. And second, we artificially removed all surface charges arising from the calculation of the pyroelectricity, because the model we use is only valid for interfaces between semiconductors, and colloidal quantum dots are not embedded in a semiconductor matrix, by definition. This choice might underestimate the amount of surface charge building up, which would decrease the potential amplitude inside the quantum dot. The qualitative results of the potential calculation, however, we believe to be correct, including all their consequences, such as the quantum confined Stark effect.

- The single-particle results of the $\mathbf{k}\cdot\mathbf{p}$-model lead to several interesting insights, as discussed above, but can't be relied on for realistic values for the transition energies, as particle interactions are not considered in this simplistic approach.

- Yet even for the more sophisticated Hartree-Fock excitons, the transition energies might not show a realistic picture, as there are multiple influences not covered by our model. The first is the fact that the exciton binding energies are affected by changes of the dielectric constant of the quantum dot environment, the same limiting factor seen for the potential calculations. The second one is that due to the possible high contrast in dielectric constants between the quantum dot shell and the environment,

mirror-charge effects could arise and would have to be included in the Hartree-Fock calculations.

- The Huang-Rhys factors are overestimating realistic values for coupling strength seen for these quantum structures. This is particularly evident in the case of Wurtzite crystal structure. The wurtzite case is shown to be caused by the wavefunction separation, which in turn leads to the violation of one of the assumptions of the employed calculation model, namely that the total net charge of the excitons be small compared to the partial charges of the atoms in the lattice. We nevertheless believe that the relative comparisons of coupling strengths, as well as the coupling frequencies and peak widths are viable results.

- The analysis of the atomic motions found in the vibrational eigenmodes of the quantum dots led to the insight that the modes coupling to the exciton dynamics bear strong similarities to classical bulk phonon dynamics on the atomic scale and that those phonons, that are highly localised do not show this kind of coupling. We believe this to be viable results, even though they are obtained using a very simple atomic interaction model.

In light of the results of this work, we would propose the following further work, to expand the results and mitigate some of the shortcomings:

- To expand the analysis of the vibrational eigenmodes, the results in this work should be compared to vibrational eigenmodes obtained using a more sophisticated interatomic potential, such as, for example, a Tersoff-potential. This might also lead to the overestimation in the Huang-Rhys factor calculations to be mitigated, since these calculations also depend on the vibrational dynamics.

- In this same line of thinking, it would be very worthwhile to investigate the atomic motions and exciton-phonon coupling of larger systems than the ones we are limited to in this work. This would require either a faster computer, or some optimisations in the calculation software.

- It would be interesting to know if the Huang-Rhys factors also show a strong dependency on non-sphericity as the one observed in the electronic structure calculations.

- Another way of extending the scope of the exciton-phonon analysis would be to project bulk phonons to an atomistic representation of, for example, an epitaxial Stranski-Krastanov quantum dot, and perform the same kind of Huang-Rhys factor calculation.

- It was shown that multishell quantum dots show an interesting screening effect of the potential inside the quantum dot core. It could be worthwhile to perform a study of the changes in electronic structure this screened potential would induce. It might be possible to design polarisation screened colloidal quantum dots, with the same benefits seen for the IFGARD structures [50].

A Implementation details

A.1 Electronic calculations

Calculations of the strain, the electric potentials, as well as the single-particle calculations are performed on a regularly spaced three-dimensional voxel grid. For this purpose, every voxel is first assigned a material composition, via a numerical value. The employed CdSe-CdS material system can be tuned in steps of one percent.
The orientation of the crystal axes relative to the three-dimensional grid is as follows:

- For zincblende crystal structure, the x-axis coincides with the [100]-direction, the y-axis coincides with the [010]-direction and the z-axis is aligned with the [001]-direction.
- For wurtzite crystal structure, the z-axis coincides with the [0001]-direction, while the x-axis is aligned with the [10-10]-direction and the y-axis is not directly aligned with a principal crystal axis, due to the symmetry of the wurtzite lattice.

For this reason, z-axis and [001]-direction (or [0001]-direction) may be used interchangeably in this work, as may the other directions/axes.

A.1.1 Quantum dot environment

The **k**·**p**-implementation used in this work was originally developed to be used for zero-dimensional quantum structures embedded in semiconductor matrix materials. For these cases, every voxel can be assigned a material composition, and for each voxel, there are well-defined parameters available, because the calculation area is made up completely by semiconductor materials.
The colloidal quantum dots explored in this work, however, are not enclosed in a matrix of other semiconductor materials. They can be surrounded, in contrast, by a variety of different materials, such as glass, water, a variety of polymer materials, or be in vacuum. Since all of these are not semiconductor materials, the **k**·**p**-method does not apply to them, and there are no material parameters available for the strain calculations as well.
Our workaround to this problem is the following:

- For the purpose of the strain-calculations the stiffness parameters of the surrounding material are set to very low values, yet not to zero, as that would lead to numerical issues with the relaxation algorithm. This yields a result analogous to a quantum dot in vacuum, that is not subject to external strains.
- The surrounding bandgap is considerably larger than the one found inside the quantum dot. We set the bandgap to a value of 14500 meV with the valence-band energy offset 2140 meV below the CdS valence band energy.
- The deformation potentials are set to zero, to not allow any influence of the strain calculation on the electronic calculation outside of the quantum dot.

Since the calculated electronic states are strongly confined inside the quantum dot, we assert that this approach to the problem leads to realistic calculation results for colloidal quantum dots, even though the employed calculation method was originally developed to only account for pure semiconductor systems. The only parameter that still strongly influences the results is the relative permittivity of the quantum dot environment. The influence of this parameter is explored in detail in section 4.3 for the electric potentials and section 5.1 for the single-particle results.

A.2 Phonon Calculations

This chapter will provide some additional details on the calculation process for the atomistic phonons, briefly outlined in chapter 2.6.
In a first step, we create a list of atomic positions that make up the quantum dot. This is done by using the bulk lattice constants of CdSe and, starting from the quantum dot center, constructing unit cells in either wurtzite or zincblende lattice structure, where we put Cd atoms at sites of one sublattice and Se atoms at the sites of the other sublattice. At sites that are farther away from the quantum dot center than the core radius, we instead place S atoms at the sites of the second sublattice. At last, all sites that are farther from the center than the total radius of the quantum dot, are deleted.
There are two further constraints on the possible atomistic representations of the quantum dot, namely:

- In order to calculate the coulombic part of the lattice energy, every atom is assigned a partial charge, as designated by the parameters in table C.3. Thus, we obtain the total charge of the quantum dot as the sum of all these partial charges. We are, however, limited to quantum dots that are charge neutral, as the geometry relaxation outlined in the next part is not well-suited to the forces arising in quantum dots with nonzero charge.

- The calculation of the vibrational eigenmodes necessitates a further constraint: In contrast to atoms not at the quantum dot surface, which always have four nearest neighbours, due to the tetragonal symmetry of both zincblende and wurtzite, atoms located at the quantum dot surface necessarily have a lower number of nearest neighbours. Atoms with only two or one nearest neighbours, however, lead to unphysical results in the vibrational calculation, as they then show a turning motion around an axis formed by their neighbours. Therefore, we need to eliminate all surface atoms with less than three nearest neighbours.

In order to obtain atomistic quantum dot configurations that meet these two constraints, we randomly vary the quantum dot center relative to the atomic lattice by a random vector, leading to different atomic configurations after the cutoff of all atoms outside the quantum dot radius. After that, we remove all surface atoms with less than three nearest neighbours, and check the total charge. We repeat this process, until we obtain a charge neutral quantum dot configuration.
Our approach to atomistic quantum dot construction demonstrates that there are various possible atomic representations for any given quantum dot geometry. To account for

possible variations in the results arising from these different configurations, we construct 10 different atomistic representations for each quantum dot geometry, and use the average of the obtained results for our analysis.

The numerical calculations performed using the GULP program [17], especially the relaxation of the atomic positions, are computationnaly demanding, and scale superlinearly with the number of atoms in the quantum dot. For this reason, we are limited in our analysis to quantum dots with a total radius of 2.6nm, for which the computation time is still feasible.

The relaxation of the atomic positions in order to obtain the atomic equilibrium positions is done via an iterative process and therefore carries a numerical error. This can lead to some of the resulting frequencies to have an imaginary part, which is of course an unphysical result. GULP outputs these imaginary frequencies as negative frequencies. In our calculations, the number of negative frequencies is always below 0.5% of the total number of frequencies. We are therefore confident to have found a good approximation of the equilibrium positions and neglect the negative results for all further analysis.

B Quantum dot Series

This appendix section lists all quantum dot geometries used for this work.

B.1 Spherical quantum dots

We consider three different series of spherical quantum dots in this work. Schematical drawings of these are found in figure B.1. Calculations were performed for both zincblende and wurtzite lattice structures for all quantum dot geometries.
Series A1 consists of quantum dots of a fixed total radius of 2.6nm with varying core sizes. Details are found in table B.1. The value for the total radius was chosen because it represents the maximum size where atomistic phonon calculations were still feasible in terms of calculation time needed. This series, then, is where all the work on phonons and exciton phonon coupling is performed.
Series A2 is made up of quantum dots with a total radius of 5 nm and varying core sizes. Details are found in table B.2. These larger dots were examined to more precisely describe the effects of the electric potentials, which strongly correlate with the size of the quantum dots, particularly the core.
The quantum dots in series A3 vary in total size, but have a fixed ratio of core radius to total radius. They allow for the examination of the effects of varying the total system size, and connect the series A1 and A2.
The calculations for varying values of the environment permittivity were performed for quantum dot geometry A2-6 (which is identical to A3-6). This geometry was also used for all plots of the calculated potentials.

Description	r_{core} [nm]	r_{tot} [nm]
A1-1	0.1	2.6
A1-2	0.35	2.6
A1-3	0.6	2.6
A1-4	0.85	2.6
A1-5	1.1	2.6
A1-6	1.35	2.6
A1-7	1.6	2.6
A1-8	1.85	2.6
A1-9	2.1	2.6
A1-10	2.35	2.6

Table B.1: Series A1 quantum dots

Description	r_{core} [nm]	r_{tot} [nm]
A2-1	0.5	5
A2-2	1	5
A2-3	1.5	5
A2-4	2	5
A2-5	2.5	5
A2-6	3	5
A2-7	3.5	5
A2-8	4	5
A2-9	4.5	5

Table B.2: Series A2 quantum dots

Description	r_{core} [nm]	r_{tot} [nm]
A3-1	1.5	2.5
A3-2	1.8	3
A3-3	2.1	3.5
A3-4	2.4	4
A3-5	2.7	4.5
A3-6	3	5

Table B.3: Series A3 quantum dots

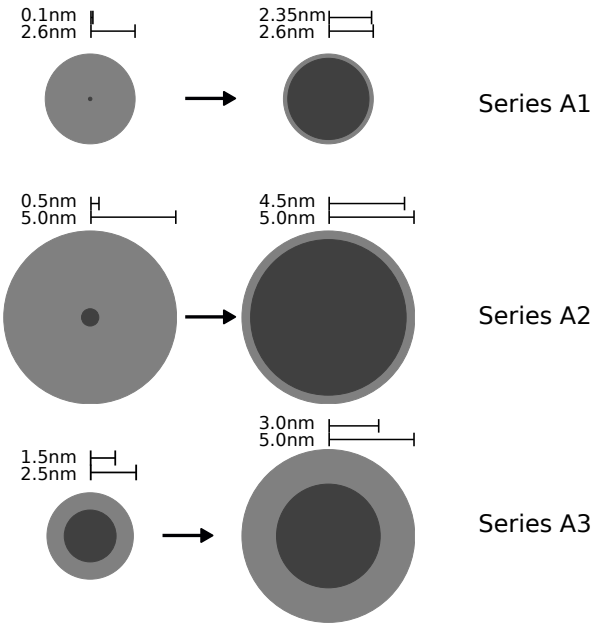

Figure B.1: Quantum dot series: Spherical quantum dot geometries. Schematic representation of the geometries of the spherical quantum dots used for calculations in this work.

B.2 Ellipsoidal quantum dots

While the geometry of spherical core shell quantum dots can be described by just the core radius and total radius, ellipsoidal quantum dots are subject to additional parameters. Generally, an ellipsoid is defined by different radii r_x, r_y and r_z, for each spacial direction. We construct these ellipsoidal quantum dots by defining an aspect ratio a, and then

calculating:

$$r_x = a \cdot r \quad ; \quad r_y = \frac{1}{\sqrt{a}} \cdot r \quad ; \quad r_z = \frac{1}{\sqrt{a}} \cdot r \tag{B.1}$$

which leads to an ellipsoidal quantum dot extended in x-direction, that retains the volume of the spherical quantum dot with radius r. The same procedure can be used to extend the ellipsoid in any other direction by switching the r_i.
Schematic representations of all ellipsoidal quantum dot geometries are given in figure B.2. Calculations for all geometries are performed for both zincblende and wurtzite lattice structures, except for series B2, which is only done for wurtzite.
Series B1 and B2 both have fixed values for the core radius and total radius, and are then modified by a range of different aspect ratios between 0.7 and 1.3. Details are found in tables B.4 and B.5. The extension is done in x-direction for series B1 and in z-direction for series B2.
Series B3 and B4 have fixed values of the aspect ratio of 0.8 and 1.2, respectively. The total radius is a constant 5nm and the core-radius is varied. Exact geometry information can be found in tables B.6 and B.7.

Description	r_{core} [nm]	r_{tot} [nm]	aspect ratio
B1-1	3	5	0.7
B1-2	3	5	0.75
B1-3	3	5	0.8
B1-4	3	5	0.85
B1-5	3	5	0.9
B1-6	3	5	0.95
B1-7	3	5	1.0
B1-8	3	5	1.05
B1-9	3	5	1.1
B1-10	3	5	1.15
B1-11	3	5	1.2
B1-12	3	5	1.25
B1-13	3	5	1.3

Table B.4: Series B1 quantum dots, the ellipsoids are extended along the x-direction

Description	r_{core} [nm]	r_{tot} [nm]	aspect ratio
B2-1	3	5	0.7
B2-2	3	5	0.75
B2-3	3	5	0.8
B2-4	3	5	0.85
B2-5	3	5	0.9
B2-6	3	5	0.95
B2-7	3	5	1.0
B2-8	3	5	1.05
B2-9	3	5	1.1
B2-10	3	5	1.15
B2-11	3	5	1.2
B2-12	3	5	1.25
B2-13	3	5	1.3

Table B.5: Series B1 quantum dots, the ellipsoids are extended along the z-direction. This series is wurtzite-only

Description	r_{core} [nm]	r_{tot} [nm]	aspect ratio
B3-1	0.5	5	0.8
B3-2	1.0	5	0.8
B3-3	1.5	5	0.8
B3-4	2.0	5	0.8
B3-5	2.5	5	0.8
B3-6	3.0	5	0.8
B3-7	3.5	5	0.8
B3-8	4.0	5	0.8
B3-9	4.5	5	0.8

Table B.6: Series B3 quantum dots, the values for the core radius are the same used for series A2.

Description	r_{core} [nm]	r_{tot} [nm]	aspect ratio
B3-1	0.5	5	1.2
B3-2	1.0	5	1.2
B3-3	1.5	5	1.2
B3-4	2.0	5	1.2
B3-5	2.5	5	1.2
B3-6	3.0	5	1.2
B3-7	3.5	5	1.2
B3-8	4.0	5	1.2
B3-9	4.5	5	1.2

Table B.7: Series B4 quantum dots, the values for the core radius are the same used for series A2.

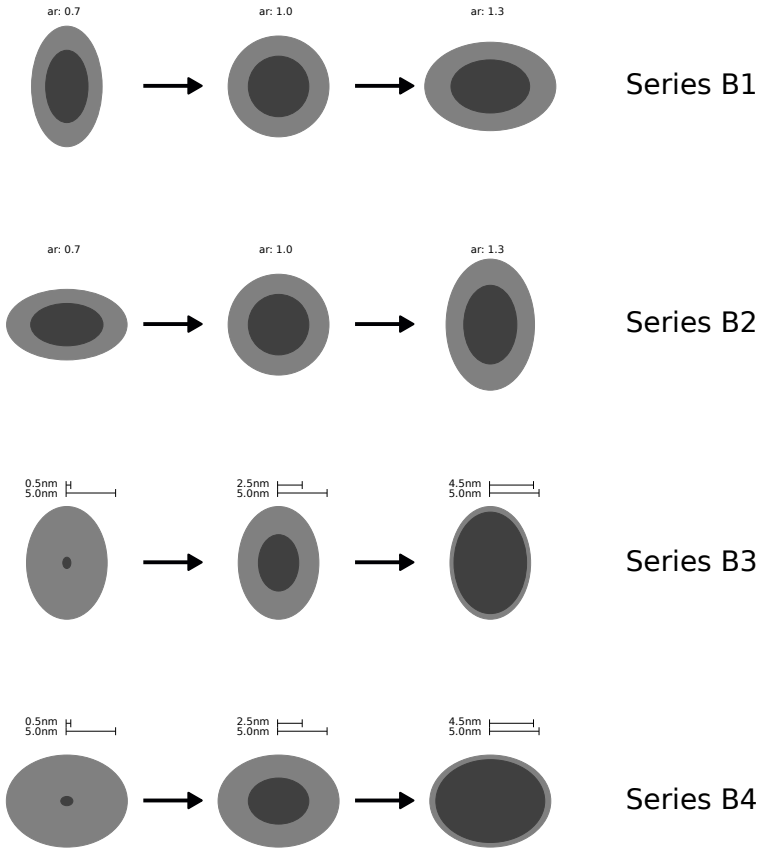

Figure B.2: Quantum dot series: Ellipsoidal quantum dot geometries. Schematic representation of the geometries of the ellipsoidal quantum dots used for calculations in this work.

B.3 Multishell quantum dots

Electric potentials are also calculated for a series of quantum dots with multiple shells. These are created by alternately adding shells of CdSe and CdS on a spherical CdSe/CdS core shell quantum dot. A schematic drawing of these multishell dots is given in figure B.3.

The radius of the core, as well as the thickness of all present shells is always 1.5 nm and the number of shells is varied between two and five. These calculations are only performed for wurtzite crystal structure, as we are interested in the behaviour of the pyroelectric potential.

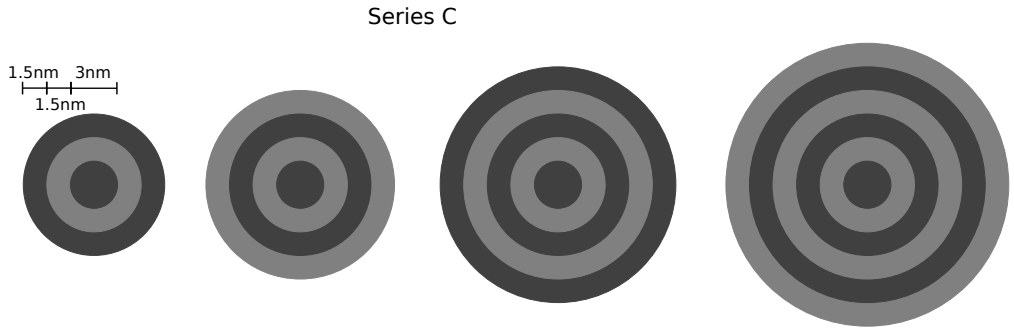

Figure B.3: Quantum dot series: Multishell quantum dot geometries. Schematic representation of the geometries of the multishell quantum dots used for calculations in this work.

C Parameter tables

Hexagonal phase

	Quantity	Unit	CdS	CdSe	Interpolation	Reference
Lattice constant	a	$\AA$	4.1348	4.2905	Linear	[56]
Lattice constant	c	$\AA$	6.749	7.015	Linear	[56]
Fundamental gap (1.8 K)	E_g	meV	2582	1841	Linear	[57]
VB edge	E_{V}	meV	180	600	Linear	[58]
Crystal-field splitting	$\triangle_{\mathrm{CR}}$	meV	27	39		[59]
Spin-orbit coupling energy	$\triangle_{\mathrm{SO}}$	meV	65	416		[59]
Optical matrix parameter	$E_p^{\parallel}$	meV	13000	13000	Linear	est. from fit procedure
Optical matrix parameter	$E_p^{\perp}$	meV	13000	13000		est. from fit procedure
CB effective mass	$m_e^{\parallel}$	m_0	0.205	0.13	Linear	[60, 61]
CB effective mass	$m_e^{\perp}$	m_0	0.205	0.13		[60, 61]
Luttinger-like parameter						
	A_1		-5.92	-10.2	Linear	[62]
	A_2		-0.7	-0.76	Linear	[62]
	A_3		5.37	9.35	Linear	[62]
	A_4		-1.82	-3.2		[62]
	A_5		-1.82	-3.2		[62]
	A_6		-1.36	-2.31		[62]
Deformation potentials						
	a_1	eV	-4.71	-14.6		cubic approx.
	a_2	eV	0.78	-10.1		cubic approx.
	D_1	eV	-3.35	-13.86	Linear	[63]
	D_2	eV	3.06	-6.42	Linear	[63]
	D_3	eV	1.3	4.0	Linear	[63]
	D_4	eV	-2.9	-2.2	Linear	[63]
	D_5	eV	1.5	-1.2		[63]
	D_6	eV	-2.4	-3.0		[63]
Elastic compliance	C_{11}	GPa	85.81	74.6	Linear	[64]
Elastic compliance	C_{12}	GPa	52.12	46.1	Linear	[64]
Elastic compliance	C_{13}	GPa	46.15	39.3		[64]
Elastic compliance	C_{33}	GPa	93.7	81.7		[64]
Elastic compliance	C_{44}	GPa	14.87	13.0	Linear	[64]
Static dielectric constant	ϵ_s		9.38	(9.15+9.29)/2	Linear	[65, 66]
Piezoelectric constants						
Linear	e_{15}	$\mathrm{C/m^2}$	-0.183	-0.138	Linear	[67]
Linear	e_{31}	$\mathrm{C/m^2}$	-0.262	-0.160	Linear	[67]
	e_{33}	$\mathrm{C/m^2}$	0.385	0.347	Linear	[67]
Spontaneous Polarization	P_{SP}	$\mathrm{C/m^2}$	-0.028	-0.006		[68, 69]

Table C.1: Material parameters for 6.5 K used in this work.

Zincblende Phase

	Quantity	Unit	CdS	CdSe	Interpolation	Reference
Lattice constant	a	A	5.832	6.057	Linear	[70]
Fundamental gap	E_g	meV	2583.0	1766.0	Linear	[71]
Averaged VB edge[72]	$E_v^{'}$	meV	396.7	60.0	Linear	
Spin-orbit coupling energy	$\triangle_0$	meV	70	420	Linear	[71]
Optical matrix parameter	E_p	meV	14214	25000	Linear	
CB effective mass	m_e	m_0	0.21	0.12	Linear	
Luttinger parameter	γ_1		2.721	4.4	Linear	[73, 74]
Luttinger parameter	γ_2		0.841	1.6	Linear	[73, 74]
Luttinger parameter	γ_3		1.152	2.68	Linear	[73, 74]
Kane parameter	B	meV nm^2	0	0	Linear	
CB-VB coupling by strain	b'	meV	0	0	Linear	
CB hydrostatic def. pot.	a_c	meV	-4450	-3770	Linear	[75, 73]
Gap hydrostatic def. pot.	a_g	meV	-5960	-5580	Linear	[75, 73]
VB shear def. pot. [100]	b_v	meV	-1180	-1200	Linear	[75, 73]
VB shear def. pot. [111]	d_v	meV	-3700	-4300	Linear	[75, 73]
Elastic compliance	C_{11}	GPa	90.7	74.9	Linear	[75, 73]
Elastic compliance	C_{12}	GPa	58.1	46.09	Linear	[75, 73]
Elastic compliance	C_{44}	GPa	51.0	39.26	Linear	[75, 73]
Static dielectric constant	ϵ_s		9.7	9.4	Linear	[75, 73]
Piezoelectric constants						
Linear	e_{14}	C/m^2	-0.05	-0.2	Linear	[75, 73]

Table C.2: Material parameters for 6.5 K used in this work. Owing to the lack of reliable bowing parameters, linear interpolation is employed for alloys.

GULP parameters

	q	ε	σ
Cd	0.966786	0.044173	1.501329
Se	-0.966786	0.035752	3.900962
S	-0.966786	0.034259	4.066081

Table C.3: Parameters used for all GULP calculations in this work

D References

[1] A. J. Shields, "Semiconductor quantum light sources," in *Nanoscience And Technology: A Collection of Reviews from Nature Journals*, pp. 221–229, World Scientific, 2010.

[2] P. Michler, A. Imamoğlu, M. Mason, P. Carson, G. Strouse, and S. Buratto, "Quantum correlation among photons from a single quantum dot at room temperature," *Nature*, vol. 406, no. 6799, p. 968, 2000.

[3] O. Benson, C. Santori, M. Pelton, and Y. Yamamoto, "Regulated and entangled photons from a single quantum dot," *Physical review letters*, vol. 84, no. 11, p. 2513, 2000.

[4] D. Bimberg, M. Grundmann, and N. N. Ledentsov, *Quantum dot heterostructures*. John Wiley & Sons, 1999.

[5] J. J. Li, Y. A. Wang, W. Guo, J. C. Keay, T. D. Mishima, M. B. Johnson, and X. Peng, "Large-scale synthesis of nearly monodisperse cdse/cds core/shell nanocrystals using air-stable reagents via successive ion layer adsorption and reaction," *Journal of the American Chemical Society*, vol. 125, no. 41, pp. 12567–12575, 2003.

[6] H. Chen, J. He, and S.-T. Wu, "Recent advances on quantum-dot-enhanced liquid-crystal displays," *IEEE Journal of Selected Topics in Quantum Electronics*, vol. 23, no. 5, pp. 1–11, 2017.

[7] M. Bruchez, M. Moronne, P. Gin, S. Weiss, and A. P. Alivisatos, "Semiconductor nanocrystals as fluorescent biological labels," *science*, vol. 281, no. 5385, pp. 2013–2016, 1998.

[8] Y. He, H.-T. Lu, L.-M. Sai, Y.-Y. Su, M. Hu, C.-H. Fan, W. Huang, and L.-H. Wang, "Microwave synthesis of water-dispersed cdte/cds/zns core-shell-shell quantum dots with excellent photostability and biocompatibility," *Advanced Materials*, vol. 20, no. 18, pp. 3416–3421, 2008.

[9] R. Xie, K. Chen, X. Chen, and X. Peng, "Inas/inp/znse core/shell/shell quantum dots as near-infrared emitters: bright, narrow-band, non-cadmium containing, and biocompatible," *Nano research*, vol. 1, no. 6, pp. 457–464, 2008.

[10] V. Sheka and D. Sheka, "Local States in a Semiconductor with a Narrow Forbidden Band," *Soviet Physics JETP*, 1966.

[11] B. Gel'Mont and M. D'yakonov, "Acceptor Levels in Diamond-Type Semiconductors," *Soviet Physics Semiconductors*, 1971.

[12] A. L. Efros and A. L. Efros, "Interband absorption of Light in a Semiconductor Sphere," *Fiz Tekh Poluprovodn*, 1982.

[13] A. Efros, M. Rosen, M. Kuno, M. Nirmal, D. Norris, and M. Bawendi, "Band-edge exciton in quantum dots of semiconductors with a degenerate valence band: Dark and bright exciton states.," *Physical review. B, Condensed matter*, vol. 54, pp. 4843–4856, aug 1996.

[14] A. V. Rodina and A. L. Efros, "Band-edge biexciton in nanocrystals of semiconductors with a degenerate valence band," *Physical Review B*, vol. 82, p. 125324, sep 2010.

[15] A. V. Rodina and A. L. Efros, "Radiative recombination from dark excitons in nanocrystals: Activation mechanisms and polarization properties," *Physical Review B - Condensed Matter*, vol. 93, no. 15, pp. 1–15, 2016.

[16] E. Rabani, "An interatomic pair potential for cadmium selenide," *The Journal of Chemical Physics*, vol. 116, no. 1, p. 258, 2002.

[17] J. D. Gale, "General Utility Lattice Program,"

[18] A. M. Kelley, "Electron-Phonon Coupling in CdSe Nanocrystals," *The Journal of Physical Chemistry Letters*, vol. 1, pp. 1296–1300, may 2010.

[19] A. M. Kelley, "Electron-phonon coupling in CdSe nanocrystals from an atomistic phonon model.," *ACS nano*, vol. 5, no. 6, pp. 5254–5262, 2011.

[20] O. Stier, M. Grundmann, and D. Bimberg, "Electronic and optical properties of strained quantum dots modeled by 8-band kp theory," *Physical Review B*, vol. 59, no. 8, pp. 5688–5701, 1999.

[21] P. Y. Yu and M. Cardona, *Fundamentals of semiconductors: physics and materials properties*. Springer, 2010.

[22] M. Suzuki and T. Uenoyama, *Group-III-Nitride Semiconductor Compounds*. Clarendon, Oxford, 1998.

[23] S. F. Borg, *Matrix-tensor Methods in Continuum Mechanics.(Based on a Preprint Edition, an Introduction to Matrix-tensor Methods in Theoretical and Applied Mechanics.)*. 1963.

[24] G. Bastard, "Wave mechanics applied to semiconductor heterostructures (les editions de physique, les ulis, france, 1988)," *Google Scholar*.

[25] P.-O. Löwdin, "Studies in perturbation theory," *Journal of Molecular Spectroscopy*, vol. 10, no. 1-6, pp. 12–33, 1963.

[26] E. O. Kane, "Band Theory and Transport Properties,"

[27] D. Gershoni, C. Henry, and G. Baraff, "Calculating the Optical Properties of Multidimensional Heterostructures: Application to the Modeling of Quaternary Quantum Well Lasers," *IEEE Journal of Quantum Electronics*, vol. 29, no. 9, 1993.

[28] T. B. Bahder, "Eight-band kp model of strained zinc-blende crystals," *Physical Review B*, vol. 41, no. 17, pp. 11992–12001, 1990.

[29] P. Enders, A. Bärwolff, M. Woerner, and D. Suisky, "kp theory of energy bands, wave functions, and optical selection rules in strained tetrahedral semiconductors," *Physical Review B*, vol. 51, no. 23, p. 16695, 1995.

[30] B. Levikovich and P. Ezekielevich, *Symmetry and strain-induced effects in semiconductors*, vol. 624. Wiley New York, 1974.

[31] S. L. Chuang and C. S. Chang, "A band-structure model of strained quantum-well wurtzite semiconductors," *Semiconductor Science and Technology*, vol. 12, pp. 252–263, 1997.

[32] D. Dugdale, S. Brand, and R. Abram, "Direct calculation of kp parameters for wurtzite AlN, GaN, and InN," *Physical Review B*, vol. 61, no. 19, pp. 12933–12938, 2000.

[33] O. Stier, "Electronic and Optical Properties of Quantum Dots and Wires," p. 203, 2000.

[34] M. Winkelnkemper, *Electronic Structure of Nitride-based Quantum Dots, TU Berlin.* PhD thesis, 2008.

[35] A. V. Rodina, M. Dietrich, A. Göldner, L. Eckey, A. Hoffmann, A. L. Efros, M. Rosen, and B. K. Meyer, "Free excitons in wurtzite GaN," *Physical Review B*, vol. 64, no. 11, p. 115204, 2001.

[36] A. Haug, *Theoretische Festkoerperphysik, vol. 1.* Franz Deuticke, Vienna, 1964.

[37] G. Hönig, "Mehrteilchenzustände in Halbleiter-Quantenpunkten, TU Berlin," 2015.

[38] Czycholl, *Theoretische Festkörperphysik.* Springer, 2008.

[39] M. Grünwald, A. Zayak, J. B. Neaton, P. L. Geissler, and E. Rabani, "Transferable pair potentials for cds and zns crystals," *The Journal of chemical physics*, vol. 136, no. 23, p. 234111, 2012.

[40] D. V. Melnikov and W. B. Fowler, "Electron-phonon interaction in a spherical quantum dot with finite potential barriers: The fröhlich hamiltonian," *Physical Review B*, vol. 64, no. 24, p. 245320, 2001.

[41] K. Huang and a. Rhys, "Theory of Light Absorption and Non-Radiative Transitions in F-Centres," *Proceedings of the Royal Society A: Mathematical, Physical and Engineering Sciences*, vol. 204, no. 1078, pp. 406–423, 1950.

[42] L. Biadala, E. V. Shornikova, A. V. Rodina, D. R. Yakovlev, B. Siebers, T. Aubert, M. Nasilowski, Z. Hens, B. Dubertret, A. L. Efros, *et al.*, "Magnetic polaron on dangling-bond spins in cdse colloidal nanocrystals," *Nature Nanotechnology*, 2017.

[43] C. Lin, D. F. Kelley, M. Rico, and A. M. Kelley, "The "surface optical" phonon in cdse nanocrystals," *ACS nano*, vol. 8, no. 4, pp. 3928–3938, 2014.

[44] C. Segarra, J. I. Climente, A. Polovitsyn, F. Rajadell, I. Moreels, and J. Planelles, "Piezoelectric Control of the Exciton Wave Function in Colloidal CdSe/CdS Nanocrystals," *Journal of Physical Chemistry Letters*, vol. 7, no. 12, pp. 2182–2188, 2016.

[45] C. Malmberg and A. Maryott, "Dielectric constant of water from 0° to 100° c," *Journal of research of the National Bureau of Standards*, vol. 56, no. 1, pp. 1–8, 1956.

[46] A. Issac, C. von Borczyskowski, and F. Cichos, "Correlation between photoluminescence intermittency of cdse quantum dots and self-trapped states in dielectric media," *Physical Review B*, vol. 71, no. 16, p. 161302, 2005.

[47] D. Schooss, A. Mews, A. Eychmüller, and H. Weller, "Quantum-dot quantum well cds/hgs/cds: Theory and experiment," *Physical Review B*, vol. 49, no. 24, p. 17072, 1994.

[48] D. Battaglia, J. J. Li, Y. Wang, and X. Peng, "Colloidal two-dimensional systems: Cdse quantum shells and wells," *Angewandte Chemie International Edition*, vol. 42, no. 41, pp. 5035–5039, 2003.

[49] M. Abe and S. Takeshi, "Magneto-optical enhancement by surface plasmon resonance in magnetic "nano-onions" with multicore-shell structures," *Journal of applied physics*, vol. 97, no. 10, p. 10M514, 2005.

[50] G. Hönig, S. Westerkamp, A. Hoffmann, and G. Callsen, "Shielding electrostatic fields in polar semiconductor nanostructures," *Physical Review Applied*, vol. 7, no. 2, p. 024004, 2017.

[51] G. Hönig, G. Callsen, and A. Hoffmann, "German patent no. 102015217330.5," 2015.

[52] G. Hönig, S. Westerkamp, and G. Callsen, "European patent no. 17160160.2 - 1551 (pending)," 2017.

[53] A. Savitzky and M. J. E. Golay, "Smoothing and differentiation of data by simplified least squares procedures.," *Analytical Chemistry*, vol. 36, no. 8, pp. 1627–1639, 1964.

[54] R. Ruppin and R. Englman, "Optical phonons of small crystals," *Reports on Progress in Physics*, vol. 33, no. 1, p. 149, 1970.

[55] V. A. Fonoberov and A. A. Balandin, "Interface and confined optical phonons in wurtzite nanocrystals," *Physical Review B*, vol. 70, no. 23, p. 233205, 2004.

[56] R. Wyckoff, *Crystal Structures*, vol. I. New York: Interscience Publishers, Inc., 1960.

[57] D. T. F. Marple and B. Segall, "Physics and Chemistry of II-VI Compounds," p. 317, Amsterdam: North Holland Pub. Co., 1967.

[58] S.-H. Wei and A. Zunger, "Calculated natural band offsets of all II-VI and III-V semiconductors: Chemical trends and the role of cation d orbitals," *Applied Physics Letters*, vol. 72, pp. 2011–2013, apr 1998.

[59] J.-B. Jeon, Y. M. Sirenko, K. Kim, M. Littlejohn, and M. Stroscio, "Valence band parameters of wurtzite materials," *Solid state communications*, vol. 99, no. 6, pp. 423–426, 1996.

[60] J. J. Hopfield and D. G. Thomas, "Fine Structure and Magneto-Optic Effects in the Exciton Spectrum of Cadmium Sulfide," *Physical Review*, vol. 122, pp. 35–52, apr 1961.

[61] S. M. Sze, *Physics of Semiconductor Devices*. 1981.

[62] T. Dietl, H. Ohno, and F. Matsukura, "Hole-mediated ferromagnetism in tetrahedrally coordinated semiconductors," *Physical Review B*, vol. 63, no. 19, p. 195205, 2001.

[63] D. W. Langer, R. N. Euwema, K. Era, and T. Koda, "Spin exchange in excitons, the quasicubic model and deformation potentials in II-VI compounds," *Physical Review B*, vol. 2, no. 10, pp. 4005–4022, 1970.

[64] O. Madelung, U. Rössler, and M. Schulz, eds., *II-VI and I-VII Compounds; Semimagnetic Compounds*, vol. 41B of *Landolt-Börnstein - Group III Condensed Matter*. Berlin/Heidelberg: Springer-Verlag, 1999.

[65] J. Wicksted, M. Matsushita, H. Z. Cummins, T. Shigenari, and X. Z. Lu, "Resonant Brillouin scattering in CdS. I. Experiment," *Physical Review B*, vol. 29, pp. 3350–3361, mar 1984.

[66] R. Geick, C. H. Perry, and S. S. Mitra, "Lattice vibrational properties of hexagonal CdSe," *Journal of Applied Physics*, vol. 37, no. 5, pp. 1994–1997, 1966.

[67] S. Adachi, *Properties of Group-IV, III-V and II-VI Semiconductors*. Chichester, UK: John Wiley & Sons, Ltd, 2005.

[68] T. Ogawa, "Estimation of the Spontaneous Polarization of Hexagonal ZnS, CdS and ZnO Crystals," *Journal of the Physical Society of Japan*, vol. 25, no. 4, pp. 1126–1128, 1968.

[69] M. E. Schmidt, S. a. Blanton, M. a. Hines, and P. Guyot-Sionnest, "Polar CdSe nanocrystals: Implications for electronic structure," *The Journal of Chemical Physics*, vol. 106, no. 12, p. 5254, 1997.

[70] S.-H. Wei and A. Zunger, "Predicted band-gap pressure coefficients of all diamond and zinc-blende semiconductors: Chemical trends," *Physical Review B*, vol. 60, no. 8, pp. 5404–5411, 1999.

[71] W. Shan, J. Song, H. Luo, and J. Furdyna, "Determination of the fundamental and split-off band gaps in zinc-blende CdSe by photomodulation spectroscopy," *Physical Review B*, vol. 50, no. 11, p. 8012, 1994.

[72] C. G. de Walle, "Band Lineups and Deformation Potentials in the Model-Solid Theory," *Phys. Rev. B*, vol. 39, no. 3, p. 1871, 1989.

[73] J. Gutowski, K. Sebald, and T. Voss, "CdS, zincblende configuration: Luttinger parameters," in *New Data and Updates for II-VI Compounds*, pp. 37–37, Berlin, Heidelberg: Springer Berlin Heidelberg.

[74] M. Willatzen, M. Cardona, and N. E. Christensen, "Spin-orbit coupling parameters and electron g factor of II-VI zinc-blende materials," *Physical Review B*, vol. 51, pp. 17992–17994, jun 1995.

[75] J. Gutowski, K. Sebald, and T. Voss, "CdSe, zincblende configuration: band structure, energies at symmetry points, gap energies," in *New Data and Updates for II-VI Compounds*, pp. 75–76, Berlin, Heidelberg: Springer Berlin Heidelberg.

Acknowledgements

I would like to take this opportunity to thank everybody that helped and supported me during the work on this PhD thesis.
First of all, I would like to thank Professor Axel Hoffmann, for giving me the opportunity to prepare my PhD thesis as a member of his group. He was always supportive when I needed advice, yet gave all of his PhD students a great deal of freedom in their respective work.
I would also like to thank Gerald Hönig, for his insights and explanations of **k**·**p**-theory in wurtzite structures and Gordon Callsen, for his explanations of everything nitride. I would also like to thank both of them for the very fruitful collaboration on the IFGARD-project.
Fortunately, I was not the only PhD-student working on the theoretical side of the group: I would like to thank Stefan Jagsch, Ludwig Hilse and Alexander Mittelstädt for the collaboration and discussions on software, hardware, simulations and all the other things that constantly break.
For the longest part of my employment in the AG Hoffmann I was part of the NEWLED-project. For their excellent teamwork in regards to this project, I would like to thank Felix Nippert and Sarah Schlichting.
During my time as a PhD-student, I supervised both the Bachelor-thesis of Marlon Placke, and the Master-thesis of Nicole Srocka. I would like to thank them both for our work together, some of which has been depicted in this PhD-thesis.
For the whole of my time in the AG Hoffmann, I had the best office neighbours one could wish for: for scientific and political discussions, general sillyness and beers I would like to thank Christoph Tyborski, Stefan Kalinowski, Felix Kampmann and Narine Ghazarian.
Most of all, I would like to thank Andrei Schliwa, who, since my Master-thesis has supervised my work, and without whom I would not have been able to finish this thesis.
I would also like to thank the rest of the Hoffmann and Maultzsch groups, it has been a great time.
Apart from my scientific environment, I would like to thank my parents, Dietrich and Karin Westerkamp, who have always supported me in everything I have undertaken.
And most of all, thank you to my girlfriend, Stefanie Marquardt, for all the support and encouragement, and for tolerating me during the phases of frustration, which are seemingly inevitable as a PhD-student.

List of Figures

List of Tables